x

Elastic and viscoelastic properties of the solid earth using normal mode based and numerical methods in 1D and in 3D

by

Akiko To

B.S. (Kyushu University) 1998
M.S. (Tokyo University) 2000

A dissertation submitted in partial satisfaction of the
requirements for the degree of
Doctor of Philosophy

in

Geophysics

in the

GRADUATE DIVISION
of the
UNIVERSITY of CALIFORNIA at BERKELEY

Committee in charge:

Professor Barbara Romanowicz, Chair
Professor Douglas Dreger
Professor David Brillinger

Fall 2006

The dissertation of Akiko To is approved:

Chair Date

Date

Date

University of California at Berkeley

Fall 2006

Abstract

Elastic and viscoelastic properties of the solid earth using normal mode based and numerical methods in 1D and in 3D

by

Akiko To

Doctor of Philosophy in Geophysics

University of California at Berkeley

Professor Barbara Romanowicz, Chair

We developed a waveform modeling tool which is suitable to apply to relatively high frequency S diffracted waveforms which propagate through strongly heterogeneous D" regions. The accuracy of the method is checked against normal mode summation in simple models and shows a satisfactory precision.

The method is applied to observed Sdiff waveforms to constrain the structure in the D" layer beneath the Indian Ocean. The SHdiff waveforms, which graze the southeastern edge of the African superplume, have previously been reported to show a rapid arrival time shift and a broadening of the waveforms with respect to the azimuth. In addition the waveforms show a secondary pulse that follows the direct Sdiff phase. The comparison of waveform data with CSEM synthetics indicates that the postcursors can be explained by

simple 3D structure effect in the D” region with a sharp, quasi-vertical boundary aligned almost parallel to the ray path.When including 3D effects in the modeling, we find that the velocity contrast across the sharp boundary is of the order of 4-5%, averaged over the last 300 km of the mantle, which is smaller than has been proposed in some studies, but larger than in existing tomographic models, implying that the “superplume” features at the base of the mantle cannot be purely thermal.

We show that a set of SHdiff waveforms, which grazed the southern border of the Pacific superplume, have similar features to waveforms which grazed the southeastern edge of the African superplume. The similarity of the two observed SHdiff waveform sets at relatively high frequencies indicates that the low velocity regions in the lower mantle under the Pacific Ocean and Africa, corresponding to the strong degree-2 pattern in shear velocity tomographic models, have a similar nature also at finer scales.

We examine how well the anomalies are resolved in the tomographic model in other regions of the D” layer. The comparison of synthetic travel time anomalies between CSEM and NACT shows limitations in the ability of NACT to handle the effects of large amplitude Vs anomalies. The comparisons of travel time anomalies predicted by 1D ray theory, CSEM and NACT shows the importance of including finite frequency effects in the modeling. The comparison of observed travel time anomalies with CSEM synthetics show that despite the limitations in the NACT method, the model (SAW24B16) gives a good prediction of travel time anomaly amplitudes particularly in the regions where the dataset for the model have a good sampling coverage.

We performed simulations of coseismic and postseismic deformation due to the Mw=7.7 1819 Allah Bund earthquake, using a previously obtained source rupture model. Our results show that Coulomb failure stress on the rupture plane of the M=7.6 2001 Bhuj event had increased by more than 0.1 bar due to the 1819 event. This is a small, but possibly significant, amount. Other historic earthquakes in the Rann of Kachchh region that occurred since 1819 also predominantly occurred in regions of enhanced ΔCFS from the 1819 earthquake. This implies that coseismic and postseismic stress changes due to the 2001 Bhuj earthquake will lead to comparable regional stress perturbations in the Rann of Kachchh region and might thus result in continued enhanced earthquake activity in an extended earthquake sequence in an otherwise low-strain rate, intra-plate setting.

Professor Barbara Romanowicz
Dissertation Committee Chair

Contents

List of Figures

List of Tables

Chapter 1

Introduction

The D” region, which encompasses the last 300km or so of the deep mantle, is thought to be a thermal and chemical boundary layer, and the site of vigorous dynamic processes. Its structure is believed to hold the keys to answering some of the crucial questions concerning the evolution of the earth, such as the ultimate fate of subducting slabs,the origin of hot spots, the amount of bottom heating driving mantle circulation, electro-magnetic coupling between the core and the mantle, and the differentiation of material that produces the chemical heterogeneity in the deep mantle.

The D” region was named by Bullen (1963) who estimated the density profile of the earth’s interior by using a seismic velocity profile and a few simple assumptions. He concluded that the lower mantle, between the depths of 1000km and 2898km, consists of two different

layers. Then he concluded that the lower layer with the depth range between 2700km and CMB, D" layer, has a density gradient that is 3 times larger than predicted assuming a constant composition for the lower mantle. This indicated the presence of heavy substances or minerals in the D" layer which are different from the rest of the lower mantle.

In the last 20 years, many seismological observations have accumulated that clearly set this region of the mantle apart. Some prominent features are the existence of ultra low velocity zones[*Garnero et al.*, 1995], anisotropy[*Vinnik et al*, 1995], small scale heterogeneity and discontinuities [*Hutko et al* , 2006; *Thomas et al*, 2006]. Many of these observations, which highlight unique characteristics or amplitudes of anomalies in the D'' layer, are made for relatively localized regions. This is because heterogeneous distribution of stations and earthquakes limits the sampling of the D" region and because only some of the seismic phases such as ScS, SKS, PKKP and SPdKS that sample a small portion of D" are used.

Recently, a phase transition, which is likely to occur at the depths of the D" layer, was discovered by high pressure experiments and ab initio calculations [*Murakami et al*, 2004; *Oganov and Ono*]. $(Mg,Fe)SiO_3$ perovskite undergoes a phase transition to a post perovskite at high pressure. Some of the properties, associated with existence of post-perovskite phase are consistent with previous findings based on seismology, such as anisotropies and discontinuities at the base of the mantle. Many questions, regarding to the nature of the D", have remain unanswered and some more questions have emerged by the discovery of the phase transition. Some of the key questions are the role of the D" layer in mantle dy-

namics, the cause of the strong heterogeneities in the D” whether they are purely due to the phase transition or some chemical heterogeneities also exist. Resolving details of the seismic structure and obtaining the accurate distribution of heterogeneities in the D” layer using seismic waves would help to answer these questions. For example, a simulation of mantle convection , which takes the phase transition into account, indicates that the scale of heterogeneity becomes smaller in the case when the phase transition is the only cause of the heterogeneities [*Nakagawa and Tackley*,2004].

Global tomographic models give an integrated view of the anomaly distribution in the D” layer. Global shear velocity tomographic models show two large-scale low velocity structures in the lower mantle one under southern Africa, and the other under the mid-Pacific, which are referred to as “superplumes”. Although tomographic models reveal the distribution of heterogeneity in the earth’s interior, because of the necessary damping and smoothing that are introduced in the inversion processes, they do not accurately recover the amplitude and gradient of the anomalies. For example, by forward modeling, strong lateral variation of heterogeneities are found in the D” region at the borders of the superplumes. Studies of travel time anomalies of D” region sensitive phases show peak to peak lateral variations of up to 10% in S velocity occurring over several hundred km, which are clearly underestimated in the tomographic models, whose maximum amplitudes are around 4% or so.

One of the problems in some studies of D” layer structure is that they rely on a weak

anomaly approximation. The approximation, also know as Born approximation, does not allow to predict the accurate amplitude of strong heterogeneity. The ray theory approximation is also used in studies of D" structure. It is a high frequency approximation which ignores the finite frequency effect of wave propagation, and therefore it is not appropriate for studying low frequency waves or diffracted waves. On the other hand, the D" layer is most widely and globally sampled by diffracted waves. Diffracted waves, so called Sdiff or Pdiff (Fig. 1.1), diffract over more than 30 degrees of epicentral distance along the core-mantle boundary. Using these phases is essential for mapping the 3D structure of D" layer especially in the southern hemisphere where there are not many stations and therefore inadequate sampling by other phases.

In chapter 2, we develop a tool that handles the waveform modeling of (1) propagation of seismic waves in 3D models with strong heterogeneity and in spherical geometry (2) diffracted waves along the core-mantle boundary, with a reasonable amount of computer resources. The Spectral Element Method, which was introduced in geophysics about 10 years ago, is a numerical method based on the weak formulation of the wave equation and it allows to take into account models with strong heterogeneity. The method is extended to spherical geometry by meshing of the sphere into hexahedra [*Chaljub* ,2000]. However, the drawback of this method is a numerical cost. In order to overcome this problem, Capdeville[*Capdeville et al.*, 2002] has developed a hybrid method that couples spectral element computations with a normal mode solution. The spectral elements are used only in the target strongly heterogeneous regions. We present the coupled method for the case

with a thin spherical shell of spectral elements, which corresponds to the heterogeneous D" layer, "sandwiched" between two modal solutions. With this method, we can compute synthetic waveforms with periods of 12 seconds in a reasonable amount of time (for Sdiff, 25 hours of computation time with 16 nodes of 4GB of memory per node). The period corresponds to a wavelength, of about 100km at the CMB. A first simulation in a 3D D" layer model based on the tomographic model SAW24B16 [*Mégnin and Romanowicz*, 2000] is presented and compared with observed data. This work has been published in *Geophysical Journal International* under [*Capdeville, To and Romanowicz, 2003*].

In chapter 3, this method is applied to observed waveforms which are significantly affected by strong heterogeneity in the D" region. First we present interesting waveforms, which sample the southern border of the Pacific superplume. Then we show similarities between these waveforms and previously observed waveforms that sample the southern border of the African superplume. Finally, we apply the coupled mode and spectral element approach to the data and estimate the velocity contrast between the outside and inside of the superplume. The results show the importance of using an appropriate tool which takes in account the strong 3D heterogeneity, especially the effect due to structures outside of the great circle path. This work has been published in *Earth and Planetary Science Letters* under [*To, Capdeville, Takeuchi and Romanowicz, 2005*].

In chapter 4, we examine how well the anomalies are resolved in other regions of the D" layer. We put special focus on the anomaly distributions in the Pacific region, where the

locations and details of sharp anomaly gradient structures around the Pacific superplume are less well understood than in the African superplume.

In Chapter 5, we focus on a postseismic displacement which lasts for more than a hundred years. The 2001 Mw 7.7 Bhuj earthquake occurred in an intraplate region showing little evidence of active tectonism, but with rather unusual active seismicity, including an earlier major earthquake, the 1819 Allah Bund earthquake (M7.7). We found that static coseismic and transient postseismic deformation following the 1819 Great Rann of Kachchh earthquake (M7.7) has increased the likelihood of failure (ΔCFS) in the region and the occurrence of the 2001 Bhuj earthquake.

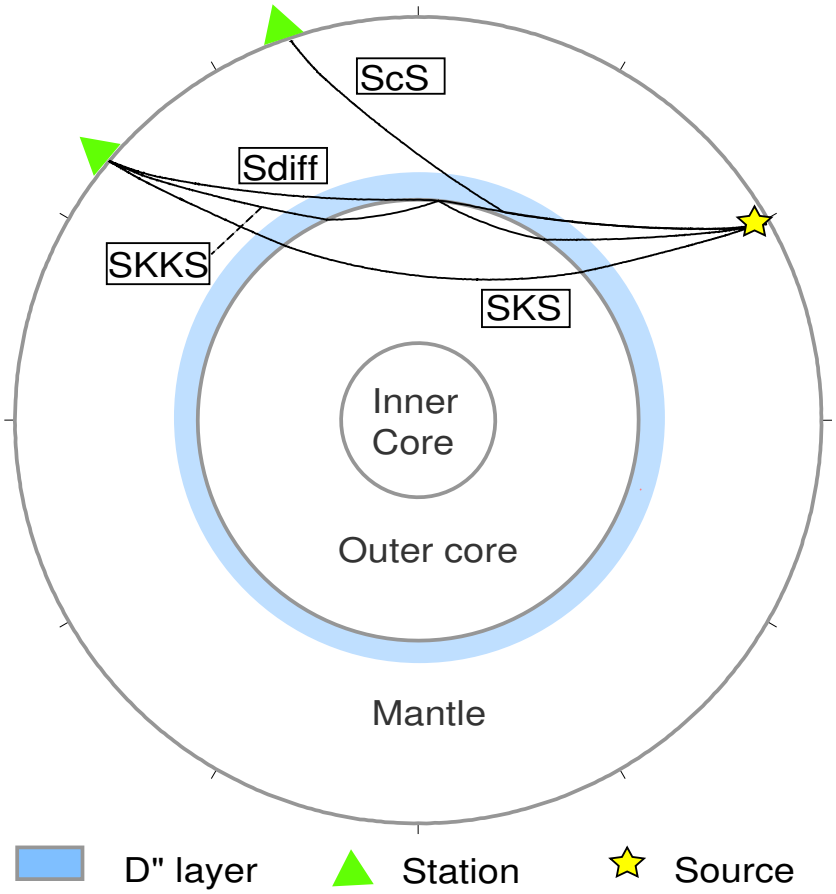

Figure 1.1: Schematic description of wave paths of SKS,SKKS and Sdiff.

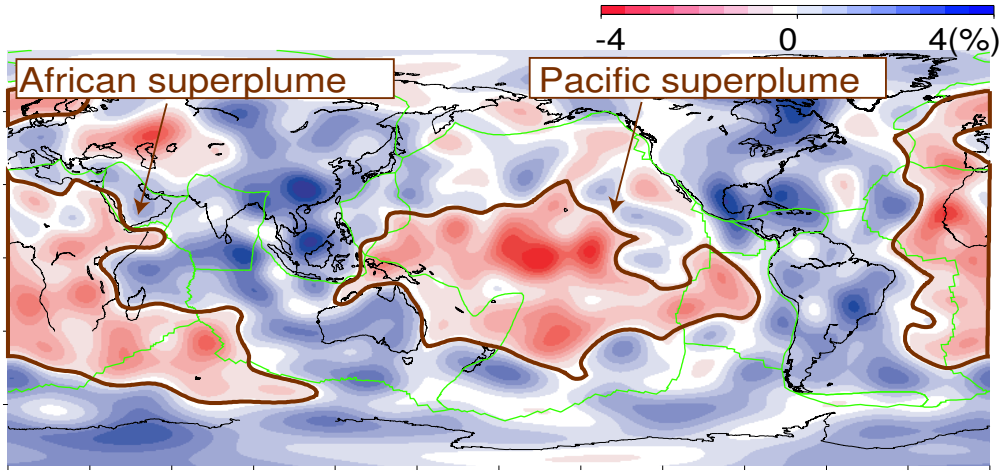

Figure 1.2: S wave velocity tomographic model (SAW24B16) at the depth of 2850km. Brown lines are contour lines of 0 % anomaly which encircle the slow anomaly regions called superplumes.

Chapter 2

Coupling Spectral Elements and Modes in a spherical earth: an extension to the "sandwich" case

This chapter has been published in *Geophysical Journal International* [*Capdeville,To and Romanowicz,2003*] with the title 'Coupling Spectral Element and Modes in a spherical earth: an extension to the sandwiched" case'

Summary

We present an extension to the coupling scheme of the Spectral Element Method (SEM) with a normal mode solution in spherical geometry. This extension allows us to consider a thin spherical shell of spectral elements between two modal solutions above and below. The SEM is based on a high order variational formulation in space and a second-order explicit scheme in time. It combines the geometrical flexibility of the classical finite element method with the exponential convergence rate associated with spectral techniques. In the inner sphere and outer shell, the solution is sought in terms of a modal solution in the frequency domain after expansion on the spherical harmonics basis. The SEM has been shown to obtain an excellent accuracy in solving the wave equation in complex media but is still numerically expensive for the whole Earth for high frequency simulations. On the other hand, modal solutions are well known and numerically cheap in spherically symmetric models. By combining these two methods we take advantage of both, allowing high frequency simulations in global Earth models with 3D structure in a limited depth range. Within the spectral element method, the coupling is introduced via a dynamic interface operator, a Dirichlet-to-Neumann (*DtN*) operator which can be explicitly constructed in the frequency and generalized spherical harmonics domain using modal solutions in the inner sphere and outer shell. The presence of the source and receivers in the top modal solution shell requires some special treatment. The accuracy of the method is checked against the mode summation method in simple spherically symmetric models and shows

very good agreement for all type of waves, including diffracted waves traveling on the coupling boundary. A first simulation in a 3D D” layer model based on the tomographic model SAW24B16 is presented up to a corner frequency of 1/12 s. The comparison with data shows surprisingly good results for the 3D model even when the observed waveform amplitudes differ significantly from the ones predicted in the spherically symmetric reference model (PREM).

2.1 Introduction

While it has long been known that the top layers of the earth’s interior, the crust and the uppermost mantle, are strongly heterogeneous, with lateral variations of structure commonly exceeding 10%, it has only recently been recognized that such strong variations may also be present at the bottom of the mantle, in the D" region. The latter, which encompasses the last 300 km or so of the mantle [*Bullen*, 1963], is thought to be both a thermal and a chemical boundary layer, and the site of vigorous dynamic processes (e.g. [*Loper and Lay*, 1995; *Lay et al.*, 1998]). Recent global tomographic models of S velocity clearly show the distinctive character of lateral variations of structure at the top and at the base of the mantle (e.g. [*Su et al.*, 1994; *Masters*, 1996; *Li and Romanowicz*, 1996; *Grand et al.*, 1997; *Liu and Dziewonski*, 1998; *Ritsema et al.* 1999; *Mégnin and Romanowicz*, 2000]). The rms velocity profile peaks in the top 200 km and then again consistently shows a marked

increase in the deepest 500-800 km of the mantle. The spectrum of lateral heterogeneity changes from being "white" in the bulk of the lower mantle, to being dominated by long wavelengths in the upper mantle as well as in the last 500 km above the CMB, as reflected in more organized spatial patterns. These patterns have been confirmed in studies focussed on the global 2D analysis of CMB diffracted waves (e.g. review [*Garnero*, 2000]).

On the other hand, the most recent seismological evidence points to the existence of strong lateral variations in D" associated with the borders of the two largest "plumes" (i.e. low velocity regions) at the base of the mantle, resolved in all tomographic models. Peak to peak lateral variations of up to 10% in S velocity occurring over several hundred km have been found, both on the border of the African Plume (e.g. [*Ritsema et al.*, 1998; *Wen and Helmberger*, 1998b; *Ni and Helmberger*, 2001]) and of the Pacific Plume [*Bréger and Romanowicz* , 1998; *Bréger et al.*, 1998]. Such strong variations cannot be interpreted in terms of thermal variations alone. Strong localized variations in P velocity have also been inferred from the study of precursors to PKP [*Vidale and Hedlin*, 1998; *Wen and Helmberger*, 1998b] and in S velocity anisotropy from the study of SVdiff [*Vinnik*,1998].

Yet, present global waveform modelling approaches rely heavily on assumptions of weak heterogeneity. While the forward modelling of travel times of body wave phases sensitive to the base of the mantle, using standard ray methods, provides helpful insights regarding the character of lateral heterogeneity, much information is yet to be gained from the analysis of waveforms. For this purpose, adequate modelling tools need to be applied.

Given the strong heterogeneity found in the two boundary layers of the mantle, appropriate tools are needed that will handle waveform modelling of the 1) propagation of seismic body and surface waves in 3D models with strong lateral variations and in spherical geometry, and 2) diffracted waves along the core-mantle boundary. Diffracted waves cannot be handled by ray-based methods. On the other hand, perturbation methods based on a normal mode formalism are well adapted to the spherical geometry, can handle diffracted waves and allow the computation of Fréchet kernels for inversion (e.g. [*Li and Romanowicz,* 1995; *Li and Romanowicz*, 1996; *Lognonne and Romanowicz*, 1990; *Clevede and Logonnne*, 1996; *Dahlen et al.*,2000]). However, the strength of the target lateral heterogeneity, which would require pushing the perturbation development to rather large orders beyond the Born approximation, and the relatively short period of the waves considered (30 sec or less), makes this approach as yet rather unpractical for waveform modelling, especially in the P-SV case (many modes to couple). Another approach that has been proposed for whole earth heterogeneous models is based on the DSM (Direct Solution Method, [*Geller and Ohminato*, 1994; *Geller and Takeuchi*, 1995]). This method, based on the weak form of the equations of motions, allows one to compute partial derivatives of seismograms, and is therefore well adapted for inversion. Unfortunately, this method is currently only available for axisymmetric models (e.g. [*Cummins et al.*,1997]) and uses the Born approximation for models without symmetry [*Takeuchi and Geller*,2000].

There have been some successes in modeling D" sensitive phases using hybrid codes, in which the computation in D" is done by a Cartesian finite difference (FD) scheme, while

outside of the deep mantle, standard 1D ray methods such as WKBJ [*Chapman*,1978], Kirchoff [*Stead and Helmberger*, 1988] or generalized rays [*Helmberger*, 1983], are applied to perform the ray tracing. The FD part is computationally heavy and the hybrid approach reduces the computation time outside of the target heterogeneous region. Wen and Helmberger [*Wen and Helmberger*, 1998a; *Wen and Helmberger*, 1998b] successfully implemented such a dual scheme, and in particular modelled the effect of the ULVZ on the PKP and SKS+SPdKS waveforms. Because the disturbance due to the ULVZ is limited to a small region of D", this type of approach is, from a computational perspective, particularly efficient. It is unfortunately not appropriate for modelling Sdiff waves. First, Sdiff can diffract over more than 20^o epicentral distance, and it is not possible to adequately simulate diffraction over a curved CMB in the cartesian FD box.

Over the last few years, much progress has been made in the development of numerical methods adapted to spherical geometry and able to compute waves emanating from a realistic seismic source, reaching, within reasonable computational time, periods of interest for teleseismic studies, making no assumptions on the strength of velocity contrasts, and able to handle interface waves and interface topography.

Among the possible numerical methods able to solve the wave equation in general Earth models, the Spectral Element Method (SEM) has been shown to be particulary efficient and accurate. The SEM has been introduced in computational fluid dynamics [*Patera*, 1984; *Maday and Patera*, 1989] and applied more recently to the 3D elastic equation [*Faccioli et*

al.,1997; *Komatitsch and Vilotte*, 1998]. This method combines the geometrical flexibility of conventional finite element methods with the exponential convergence rate associated with spectral techniques, and suffers from minimal numerical dispersion and diffusion. The extension to spherical geometry has been introduced by [*Chaljub* ,2000; *Chaljub et al.*, 2003] developing a mesh of the sphere with deformed cubes named the "Cubic Sphere" starting from the work of [*Sadourny*, 1972] and [*Ronchi*, 1996], and allowing nonconforming interfaces using the mortar method [*Bernardi et al.* , 1994]. The effects of anisotropy, attenuation [*Komatitsch and Tromp*, 1999], rotation and gravity [*Komatitsch and Tromp*, 2002] have also been introduced. In spite of all the qualities of the method, the main drawback is still the numerical cost. The method can address corner frequencies between 1/20 Hz and 1/15 Hz but only with huge amount of memory (100 Gbyte is an order of magnitude) and with a large CPU time, making it still impractical to test numerous models, as one would want to do in a forward modelling approach, or compute the wavefield for hundreds of sources in an iterative global inversion scheme.

A solution to that problem, allowing higher frequency simulations using smaller machines (smaller memory and less CPU time), has been introduced with the coupling of the SEM with the modal solution [*Capdeville* ,2000; *Capdeville et al.*, 2002; *Capdeville et al.*, 2002]. The idea of this method is to limit the use of the expensive SEM in regions of the Earth that, depending on the problem studied, include 3D heterogeneity, and to use the cheaper modal solution in regions that can be assumed spherically symmetric. The coupling between the SEM , expressed in space and time domain, and the modal solution, expressed in fre-

quency and wave-number domain, is not trivial and requires some original solutions that are explained in detail in [*Capdeville et al.*, 2002] (hereafter referred to as “paper 1”). In the spectral element method, the coupling is introduced via a dynamic coupling operator, a Dirichlet-to-Neumann (DtN) boundary operator. The operator can be explicitely constructed in the frequency domain and in the generalized spherical harmonics basis, using classical modal solution techniques.

In paper 1, only one coupling interface was allowed with an external shell of spectral elements over an inner sphere in which the modal solution is found. The typical application of such a partitioning is for a heterogeneous crust over a spherically symmetric mantle and core. We present here an extension of the coupled method to the case of a thin spherical shell of spectral elements “sandwiched” between two modal solutions. A target application of this new development is the study of the D” layer, which is strongly heterogeneous, as discussed above. In that case, a layer with 3D structure at the bottom of the mantle can be used between two spherically symmetric models. This paricular coupling type is not trivial, due to the fact that the source and the receivers are in the modal solution domain, as we will show here. We finally present and discuss an example of simulations, with a 3D model in the D” layer obtained using the S tomographic model SAW24B16 [*Mégnin and Romanowicz*, 2000] and PREM [*Dziewonski and Anderson*, 1981] and some comparisons with data.

2.2 Problem statement and method principle

We consider a non rotating Earth Ω of radius r_Ω. The equation of motion to be solved in Ω is:

$$\rho(\mathbf{r})\ddot{\mathbf{u}}(\mathbf{r},t) - \mathscr{H}\mathbf{u}(\mathbf{r},t) = \mathbf{f}(\mathbf{r},t)\,, \tag{2.1}$$

where ρ is the density, $\mathbf{u}$ is the displacement field, $\ddot{\mathbf{u}}$ its second partial derivative with respect to time t, $\mathscr{H}$ is the elasto-gravity operator for a non rotating spherical Earth (e.g. [*Valette,* 1986; *Woodhouse and Dahlen*, 1978]) and $\mathbf{f}$ the generalized body force due to the earthquake. We assume a free surface boundary condition $\partial\Omega$, and an initial state of the form $\mathbf{u}(\mathbf{r},0) = \dot{\mathbf{u}}(\mathbf{r},0) = 0$. We divide the earth in three parts, an external shell Ω_{M2}, an internal sphere Ω_{M1}, and an internal shell Ω_S sandwiched between them. We name Γ_1 the spherical boundary between the domains Ω_{M1} and Ω_S, and Γ_2 the spherical boundary between the domains Ω_S and Ω_{M2} (see Fig. 2.1). Note that if Ω_{M2} is reduced to 0, we are in the same situation as presented in paper 1, that is, one external shell over an inner sphere. We assume that all lateral heterogeneities of the Earth model are localized in the inner shell Ω_S, and that the Earth model within Ω_{M1} and Ω_{M2}, as well as on Γ_1 and Γ_2, is spherically symmetric. Depending on the Earth model considered, the radius r_{Γ_i} of interface Γ_i can be set anywhere between the core–mantle boundary radius and r_Ω. The basic idea of the method is to use the spectral element method (SEM) in the heterogeneous part, that is Ω_S, and a modal solution in Ω_{M1} and Ω_{M2}. The latter is well known when the model properties are only varying radially. The point is that, on the one hand, the spectral element method

is very well adapted to a general 3D medium but is time and memory consuming from a numerical point of view. On the other hand, the modal solution has a very low numerical cost in spherically symmetric media. Combining these two methods, we expect to optimize the numerical cost of wave propagation in Earth models where, for example, we wish to focus the investigation on lateral heterogeneities in a given depth range of the mantle, such as D" and its vicinity.

2.2.1 Variational formulation

We first solve the wave equation using the SEM in Ω_S. The coupling with the modal solution in Ω_{M1} and Ω_{M2} will then come naturally. The SEM is a finite element method which solves the equation of motion in its variational form that is the integral form of (2.1). In this problem formulation, we seek a solution in $\mathscr{V}$, the set of square-integrable functions with square-integrable generalized first derivatives over Ω_S. The problem to be solved is : find $\mathbf{u}(\cdot,t) \in \mathscr{V}$, such that $\forall t \in \mathbf{I} = [0,T]$, the time duration of the simulation, and $\forall \mathbf{w} \in \mathscr{V}$

$$(\rho\ddot{\mathbf{u}},\mathbf{w}) + a(\mathbf{u},\mathbf{w}) - \sum_{i=1,2} langle\mathbf{T}_{\Gamma_i},\mathbf{w}\rangle_{\Gamma_i} = (\mathbf{f},\mathbf{w}) \tag{2.2}$$

with $(\mathbf{w}, \rho\mathbf{u})\,|_{t=0} = 0$ and $(\mathbf{w}, \rho\dot{\mathbf{u}})\,|_{t=0} = 0$, where $(\cdot,\cdot)$ is the classical L^2 inner product, the symmetric elasto–gravity bilinear form $a(\cdot,\cdot)$ expression can be found in paper 1 and

$$\langle \mathbf{T}_{\Gamma_i}, \mathbf{w} \rangle_{\Gamma_i} = \int_{\Gamma_i} (\mathbf{T}_{\Gamma_i} cdot \mathbf{w})\, \mathrm{d}\mathbf{x}, \tag{2.3}$$

where $\mathbf{T}_{\Gamma_i}$ is the traction on the spherical interface Γ_i. To solve (2.2), we need to know $\mathbf{T}_{\Gamma_i}$. As will be shown in section 2.2.3, $\mathbf{T}_{\Gamma_i}$ can be computed as a function of the incident displacement $\mathbf{u}_{\Gamma_i}$ on each coupling interface and this is where the coupling is performed.

2.2.2 The Spectral Element Approximation

The basic principle of the SEM, which is very close to the classical finite element method, is to solve (2.2) using a high degree polynomial approximation by elements of functions in $\mathscr{V}$ space. In this method, elements have to be deformed cubes, so a cubic meshing of the spherical shell has to be found. The "cubic sphere" proposed by [*Sadourny*, 1972] and further extended by [*Ronchi*, 1996] allows such a meshing of a spherical surface by decomposing it into six regions of identical shape which can be mapped onto a cube face. To obtain the meshing of a spherical shell, spherical surfaces are connected radially (see figure 2.2), where non conforming interfaces are allowed [*Chaljub et al.*, 2003]. Each numerical integration of (2.2) is performed using the Gauss-Lobatto-Legendre (GLL) quadrature in each cartesian direction. The polynomial basis is built using the Lagrange polynomial

associated with GLL points. A detailed description of the spectral element method applied to the wave equation can be found in [*Komatitsch and Vilotte*, 1998] and [*Chaljub et al.*, 2003].

In this paper, the anelasticity of the medium is taken into account in the SEM following the scheme presented in [*Komatitsch and Tromp*, 1999].

2.2.3 The *Dirichlet to Neumann* operator

In this part, we recall results obtained in Paper 1 ignoring for the moment that the source and the receivers will be in the upper modal solution domain, Ω_{M2}. This aspect will be examined in the next section. The continuity of traction and the continuity of displacement, or the normal displacement (depending on whether Γ is a solid–solid or a solid–fluid interface), through each interface $\Gamma_i, i = 1,2$, have to be assured. Assuming that the solution to the wave equation (2.1), without the right-hand-side (rhs) $\mathbf{f}$, is known in Ω_{Mi}, if a boundary condition in displacement is imposed on the interface Γ_i, the stress field can be computed everywhere in Ω_{Mi} and in particular the traction on Γ_i is known. Using the continuity relations of displacement and traction through Γ_i, we are then able to construct an operator $\mathscr{A}_i$ that, for a given displacement $\mathbf{u}_{\Gamma_i}$ on Γ_i, returns the corresponding traction that Ω_{Mi} applies on Ω_S :

$$\mathscr{A}_i \quad : \quad \mathbf{T}_{\Gamma_i}(\mathbf{r},t) = \mathscr{A}_i\left(\mathbf{u}_{\Gamma_i}(\mathbf{r},t)\right), \tag{2.4}$$

for a solid–solid interface and

$$\mathscr{A}_i \quad : \quad \mathbf{T}_{\Gamma_i}(\mathbf{r},t) = \mathscr{A}_i\left(\mathbf{u}_{\Gamma_i}(\mathbf{r},t)\cdot\mathbf{n}(\mathbf{r})\right), \tag{2.5}$$

for a solid–fluid interface, where $\mathbf{n}$ is the normal outward unit vector to the surface Γ_i. Form the point of view of Ω_S, the boundary condition on Γ_i is a Neumann condition (condition in traction) that depends on a Dirichlet condition (condition in displacement), therefore the operator $\mathscr{A}_i$ is named a *Dirichlet to Neuman* (*DtN*) operator. This operator allows us to compute (2.3) knowing $\mathbf{u}_{\Gamma_i}$, as for a classical absorbing boundary problem (e.g. [*Givoli and Keller*, 1990; *Grote and Keller*, 1995; *Sanchez-Sesma and Vai*, 1998]).

As shown in paper 1, the *DtN* operator is built in the frequency – generalized spherical harmonic domain [*Phinney and Burridge*,1973], in which the solutions of (2.1) without the right hand side term are well known in spherically symmetric models. For each angular order ℓ, an operator in frequency $\mathscr{A}_\ell(\omega)$ is found which, due to the spherical symmetry of the problem, does not depend on the azimutal order (m). This operator is not defined for a discrete set of frequencies Π_d^ℓ, that correspond to the eigenfrequencies of Ω_{Mi} for the homogeneous Dirichlet problem (no displacement at the boundary Γ_i). Note that if one needs to include attenuation in the spherically symmetric part of the model, anelasticity is simply approximated by introducing a complex part in each eigenfrequency of Π_d^ℓ, as it is classically done in normal mode problems (e.g. [*Takeuchi and Saito*, 1972]).

Because the SEM is a time–space method, the *DtN* operator has to be computed in this domain. The first and most difficult step is to compute $\mathscr{A}_\ell$ in the time domain for each ℓ. First, because of its singularities at each frequency of Π_d, this operation cannot be performed by a traditional fast Fourier transform (FFT). To circumscribe this problem, the continuous spectrum, on which a classical FFT can be performed, is separated form the discrete spectrum. The Fourier transform of the discrete part of the operator can be obtained using the Cauchy theorem, which finally allows us to obtain the *DtN* operator in the time domain. The *DtN* operator is naturally causal, but in order to be compatible with the SEM time evolution scheme, it has to be numerically causal. By numerically causal we mean that the *DtN* operator in time that is obtained from the *DtN* operator in frequency, using the numerical process previously described, must be equal to zero before $t = 0$. If it were not the case, $\mathbf{u}_{\Gamma_i}(t)$ would be required at time steps future to the current time step, in order to compute $\mathbf{T}_{\Gamma_i}(t)$ correctly at the current time step, which is obviously not possible. Unfortunately, the frequency window used for the Fourier transform is not infinite (the maximum frequency possible is the Nyquist frequency), and such a filtering is not causal. In order to circumscribe this second problem, a regularized *DtN* operator, $\mathscr{A}^r_\ell$, is used, where $\mathscr{A}^r_\ell(\omega)$ is close to zero for the high frequencies. On such a regularized *DtN* operator, the frequency window filtering has no effect and the causality is numerically preserved. $\mathscr{A}^r_\ell$ is obtained by subtracting from $\mathscr{A}_\ell$ an asymptotic operator $\mathscr{C}_\ell$ valid for the high frequency of the *DtN* operator, which can be obtained analytically (see Paper 1). With such a regularization, the expression of the traction in the generalized spherical harmonic

domain is,

$$\mathbf{T}_{\Gamma_i,\ell,m} = \mathscr{A}^r_\ell * \mathbf{u}_{\Gamma_i,\ell,m} + \mathscr{C}_\ell * \mathbf{u}_{\Gamma_i,\ell,m} \tag{2.6}$$

where $*$ is the time convolution. As $\mathscr{A}^r_\ell$ is causal, $\mathscr{A}^r_\ell * \mathbf{u}_{\Gamma_i\ell,m}$ can be computed numerically without any problem and it can be shown that $\mathscr{C}_\ell * \mathbf{u}_{\Gamma_i,\ell,m}$ can be computed analytically. Mathematically speaking, $\mathscr{A}_\ell$ is not a bounded operator and therefore, the numerical Fourier transform cannot be performed on it properly. The regularized operator $\mathscr{A}^r_\ell$ is bounded (it goes down to zero for high frequency), and therefore the numerical Fourier transform can be performed on it properly, which solves the problem.

After having obtained $\mathbf{T}_{\Gamma_i,\ell,m}$ in time, the second step is to obtain it in space. To do so, a backward Legendre transform, that is the summation over ℓ and m of coefficients $\mathbf{T}_{\Gamma_i,\ell,m}$ on the generalized spherical harmonic basis, has to be performed. The summation over ℓ has to be numerically truncated after an ℓ_{max} that does not affect the coupling process (the summation over m is naturally truncated as, for a given ℓ, m must lie between $-\ell$ and ℓ). To evaluate this corner angular order ℓ_{max}, the dispersion curve of the surface waves of the inner sphere for the homogeneous Dirichlet boundary condition problem can be used. As a matter of fact, with such a curve, for a given maximum frequency of the source, a maximum angular order can be found. This maximum angular order corresponds to the maximum angular order that a wave would have in the inner sphere in the far field of the source. Multiplying this angular order with a "safety" coefficient (Γ_i can be in the near field of the source and the medium close to the interface in Ω_S can be strongly heterogeneous),

let's say 2, a very good coupling is obtained. Finally, the traction expression which is to be used to evaluate (2.3) is

$$\mathbf{T}_{\Gamma_i} = \sum_{\ell=0}^{\ell=\ell_{max}} \sum_{m=-\ell}^{m=+\ell} \left(\mathscr{A}^r_\ell * \mathbf{u}_{\Gamma_i,\ell,m} + \mathscr{C}_\ell * \mathbf{u}_{\Gamma_i,\ell,m} \right) \cdot \mathscr{Y}_{\ell,m} \tag{2.7}$$

where $\mathscr{Y}_{\ell,m}$ is the generalized spherical harmonic basis.

2.2.4 Particularity of the coupling due to the "sandwich"

The introduction of the "sandwich" geometry has two practical consequences that have to be treated: the source and the receivers are in the upper modal solution domain.

The resolution and the construction of the *DtN* operator remains unchanged in the inner sphere Ω_{M1}, but in the outer shell Ω_{M2}, we must take into account the right hand side **f** in the resolution of (2.1). This is performed by adding a particular solution of (2.1) to the general one which gives the following *DtN* relation,

$$\mathscr{A}_i \quad : \quad \mathbf{T}_{\Gamma_2}(\mathbf{r},t) = \mathscr{A}_2\left(\mathbf{u}_{\Gamma_i}(\mathbf{r},t)\right) + \mathscr{B}(\mathbf{r},t)\,, \tag{2.8}$$

in the solid–solid case (the solid–liquid case is similar) where $\mathscr{B}$ is the particulr solution term due to the presence of the source in Ω_{M2}. $\mathscr{B}$ is computed using the modal solution of Ω_{M2} where the boundary condition on Γ_2 is chosen as an homogeneous Dirichlet condition

(no displacement) for practical reasons (see appendix .1 for details).

As receivers are on the free surface of the Earth, they are located in the modal solution domain Ω_{M2}. We must therefore use the modal solution to obtain the displacement at the surface. This is performed using an operator $\mathscr{P}$ similar to the *DtN* operator that continues the SEM domain solution on the coupling interface Γ_2 up to the free surface in the modal solution domain:

$$\mathscr{P} \quad : \quad \mathbf{u}^{M2}(\mathbf{r},t) = \mathscr{P}\left(\mathbf{u}_{\Gamma_i}(\mathbf{r},t)\right) + \mathscr{B}^d(\mathbf{r},t)\,, \tag{2.9}$$

where $\mathbf{u}^{M2}$ is the displacement in Ω_{M2}, $\mathscr{B}^d$ is a term similar to $\mathscr{B}$ but in displacement and at the free surface.

All operators $\mathscr{A}_2$, $\mathscr{B}$, $\mathscr{B}^d$ and $\mathscr{P}$ have a discrete spectrum that is a subset of the spectrum of the spherical shell Ω_{M2} with free surface condition at the surface and homogeneous Dirichlet condition on Γ_2 but they are not all exactly the same. Indeed, some eigenfrequencies corresponding to surface waves do not contribute to the *DtN* after a certain frequency depending on the depth of Γ_2, and are therefore not present in the spectrum of $\mathscr{A}_2$, $\mathscr{B}$ and $\mathscr{P}$. However, they are present in the spectrum of $\mathscr{B}^d$.

2.3 Validation tests

Before presenting a test of the “sandwich” coupling, we first present a validation test fo a diffracted wave on the coupling interface. A diffracted wave exactly on the coupling interface is a very difficult case for this method because such a wave stays on the *DtN* boundary for a long time and is therefore very sensitive to any error that occurs during the coupling process (an even worse case, i.e. Stoneley waves on the coupling boundary, is discussed in [*Capdeville* ,2000]). Furthermore, this kind of wave (Sdiff and Pdiff) is widely used to study the D” layer, and because we do not consider any heterogeneity in the outer core, the coupling interface Γ_2 will be set at the CMB and therefore diffracted waves will propagate on the *DtN* boundary. It is therefore crucial to test the accuracy of simulations in this particular case.

To do so, we use a simple model that is a homogeneous spherical shell (external radius: 6371 km) over a liquid inner sphere (radius 2871 km). The external shell S wave velocity (β) is 6 kms^{-1}, the P wave velocity (α) is 8 kms^{-1}, the inner sphere P wave is set to 4 kms^{-1} to create a shadow area for P waves so that Pdiff and PKP waves do not mix (figure 2.3). The density is everywhere 3000 kgm^{-3}. The source, located at a depth of 1048 km, is an explosion (this implies that no SHdiff waves will be generated, but SHdiff is not a difficult case because for this wave, the boundary is only a free surface), and the corner frequency is 1/125 Hz. Figure 2.4 shows the spectral element mesh used for that test. We compare synthetics obtained with the coupled method with normal mode synthetics at 4

different epicentral distances on figure 2.5. The residuals, amplified 10 times, show a very good agreement which validates the coupling in that case and demonstrates that diffracted waves propagating along the coupling interface are computed with a satisfactory accuracy. More tests of the *DtN* but non specific to the sandwich coupling can be found in [*Capdeville* ,2000] or [*Capdeville et al.*, 2002].

To validate the sandwich coupling, we perform a test in a fully homogeneous sphere with a very deep source. The test is once again unrealistic geophysically speaking, but has every difficulty, and even more (the source is not usually so deep), of a realistic case for the coupling. Furthermore, the normal mode solution is, in that case, quasi-analytic and therefore suitable. The source is very deep in order to minimize surface waves that could hide problems at the coupling interface. The elastic properties of the sphere are the same as those of the external shell in the previous test. The different radii are $r_{\partial\Omega}$ =6371 km, r_{Γ_2} =3810.5 km and r_{Γ_1} =2560.5 km. The spectral element mesh is exactly the same as the one in figure 2.4, but, because of geometrical effects (radii are smaller), the maximum corner frequency can be higher (1/55 Hz). The source is a strike-slip earthquake at 1272 km depth. In figure 2.6, we present, on the top graph, the contribution of the two terms of equation (2.9) to the actual seismogram. The term $\mathscr{B}^d$ represents the source contribution in a spherical shell with a rigid boundary condition at the bottom. The reflection of the inner interface can be clearly seen, especially on the transverse component. The term $\mathscr{P} * \mathbf{u}_{\Gamma_2}^{M2}$ is the contribution of the *DtN* operator to the final seismogram. This contribution cancels all the reflections at the inner interface of the term $\mathscr{B}^d$,to finally obtain a very good match with

the normal mode summation reference solution. Once again the accuracy is satisfactory.

Finally, we show in figure 2.7 a comparison with normal mode solution in PREM. The configuration is similar to the one in the previous test, but the source is now 600 km deep and r_{Γ_1} has been set to 3480 km to match the core mantle boundary. Once again, residuals for both vertical and transverse components show a very good agreement.

2.4 An example of application: the D" layer

We perform a simulation of one deep event (621 km deep) of Magnitude 6.8 (September 4 97, Fiji) using PREM in the top shell, and the 3D degree 24 SH model SAW24B16 [*Mégnin and Romanowicz*, 2000], in the 370 km above the CMB. To obtain P wave velocity and density heterogeneities, we use simple linear relations, $\delta\rho = 0.4\delta\beta$ and $\delta\alpha = 0.25\delta\beta$. The source mechanism is obtained from the Harvard CMT catalog and we have chosen 10 stations form CNSN (code used on figures: CN), USAF/USGS (GT), GSN-IRIS/IDA (II), GSN-IRIS/USGS (IU), USNSN (US) and LODORE (XT) networks (figure 2.8). All epicentral distances lie between 95° and 127° and we look at ScS waves and S diffracted on the CMB. The spectral element mesh used has about 12000 elements and 4.10^6 integration points (see figure 2.9) which allows a minimum corner period of $12s$.

We first present synthetics in PREM and SAW24B16 at two stations (INK and LMN) in figure 2.10. The effect on P waves (vertical component) is weak at this frequency, but the effect

on Sdiff (transverse component) is noticeable, especially for the amplitude at LMN. This effect should be observable on the corresponding data.

Our next step is to compare data with synthetics produced in the 3D model and in PREM for reference. To do so, station response and crude ellipticity correction has been applied to synthetics. Figure 2.11 presents such a comparison for the 10 stations considered. These 10 stations have been chosen for their representativity when comparing data and synthetics. Two phases are shown, ScS or Sdiff and sScS or sSdiff (depending on the epicentral distance). The first observation is that, for most of the stations and to the first order, the 3D model does a better job than PREM , both on the time delay and on the amplitude. This is especially true for stations like LMN and BOSA at large epicentral distance, where the effect on the amplitude is the strongest. Note that slow regions are systematically associated with higher amplitude than PREM (.e.g. YKW3, LMN) and fast regions with smaller amplitude than PREM (BOSA). The fact that a tomographic model gives a good result on the amplitude was not obvious a priori and is a good surprise. But the 3D models explain only the first order features of the data, and not at all stations. The time shift due to the 3D model is sometime to strong (e.g. WMQ) and sometime both amplitude and phase are poorly explained (e.g. BW06 or TLY). It shows that interesting work still remains to better explain observed diffracted waveforms, even at the relatively long periods considered. The second phase, sSdiff, is poorly modeled. This can be explained by the fact that this wave spends significant time in the strongly heterogeneous upper mantle near the source, and this heterogeneity is not accounted for in the model. This shows one of the limitations of our

approach linked to the fact that we do not take into account heterogeneities anywhere else than in and above the D" layer. Nothing prevents us, however, from progressively incorporating heterogeneity at different levels in the mantle, and in particular, from considering, in the future, two or more shells of strong 3D structure, as needed.

Finally, in figure 2.12 are plotted time arrivals of ScS or Sdiff phases computed by linearized ray tracing and by the coupled method using waveform cross-correlation for a large number of stations. It shows that in most cases ray tracing and the coupled method have time residuals of the same sign, but with significant differences of absolute value. The general trend is that linearized ray theory overestimate time residual, which is coherent with the wavefront healing phenomenon [*Hung et al.*, 2001]. A more extensive discussion of the type of comparison will be given in a forthcoming paper.

This particular simulation was performed on 64 processors of the IBM machine of the NERSC, it required about 13Gbytes of memory and lasted approximatively 20 hours.

2.5 Discussion and conclusions

We have presented an extension to the coupled spectral elements/modes method, which allows us to consider a thin spherical shell of spectral elements "sandwiched" between two modal solutions. This extension provides a way to obtain relatively high frequency seismograms at reasonable computation cost to study 3D structure in specific shells of

the earth. The method accuracy is checked against normal mode summation in simple models and shows a satisfactory precision. An important application, as shown here, is the study of the D” layer and its vicinity, where we can reach corner frequencies under 10 s on moderately large parallel computers (typically 64 processors and under 20Gbytes of memory). Using this tool, we hope to provide strong constrains on the 3D heterogeneity in and above D”, in well sampled regions of geodynamical interest, such as in the region of the Pacific superplume.

The comparison of observed S diffracted seismograms for paths sampling D" across the Pacific ,with synthetics computed in an existing tomographic model in which heterogeneity has been restricted to the bottom 370km of the mantle shows surprisingly good agreement, not only in phase, but also in amplitude (in contrast to PREM synthetics), at least down to a 12 s corner frequency. This indicates that 3D effects not accounted for by the theoretical approximations used in the construction of model SAW24B16 are not systematically dominant. Notable differences remain, and will be investigated further. The main limitation of the approach presented in this paper is of course the fact that the model is not 3D everywhere, but this is the price to pay to be able to reach interesting frequencies and not be too restricted in the number of trial models to run.

Another interesting target of such a method is the inner core. In that case, the SEM would be used only in the inner core and the modal solution everywhere else. Corner frequencies of 5 s should be within range with the same type of machines.

Among the possible future developments, it is possible to introduce some 3D structure in the modal part, such as ellipticity, using modal perturbations. But it will not be possible to include general 3D models without falling again in the classical difficulties of normal mode perturbation techniques.

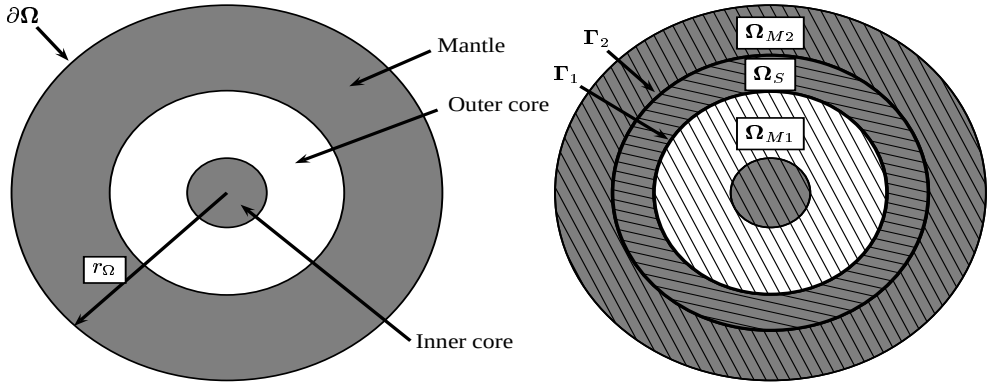

Figure 2.1: The Earth domain Ω (left) is divided in three parts (right), an external shell Ω_{M2}, an internal shell Ω_S and an internal sphere Ω_{M1} separated by two spherical boundaries Γ_2 and Γ_1. In this sketch, Γ_1 is located on the core mantle boundary and Γ_2 in the lower mantle. We assume that lateral heterogeneities of the Earth model are only present in Ω_S, so that the SEM needs only to be used in that domain and modal solutions in Ω_{M1} and Ω_{M2}.

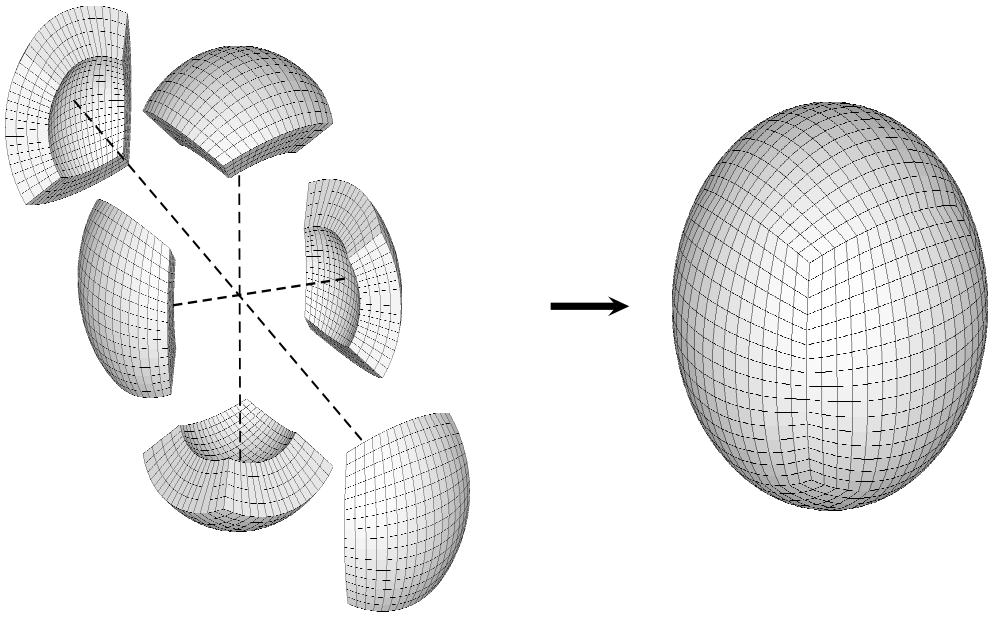

Figure 2.2: Left: Split view of the six regions. Right: assembled view of the six regions in a spherical shell.

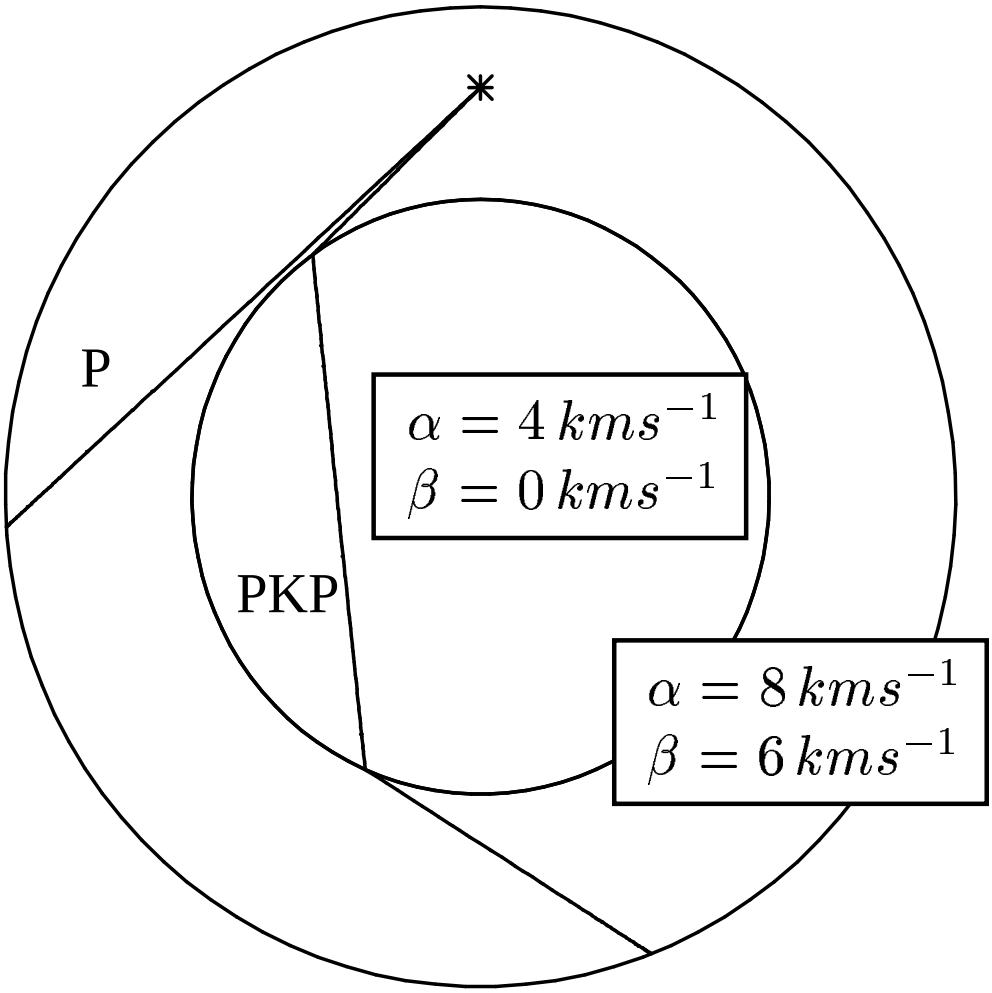

Figure 2.3: Two rays with very close ray parameters in the homogeneous sphere with a liquid inclusion showing the wide shadow area between the P and PKP waves.

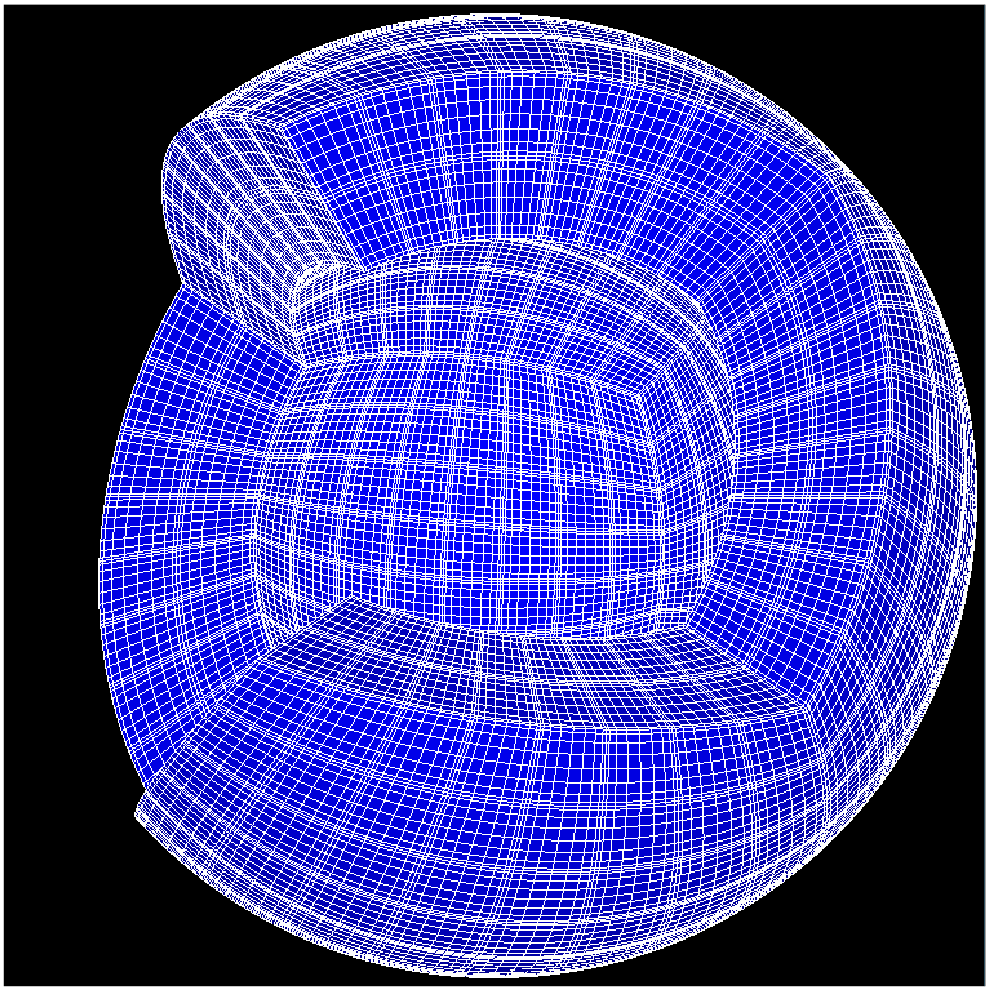

Figure 2.4: Spectral element mesh used in the homogeneous test. It has 8 elements in each horizontal direction in each region and 2 elements in the vertical one. The polynomial degree is 8 in each direction.

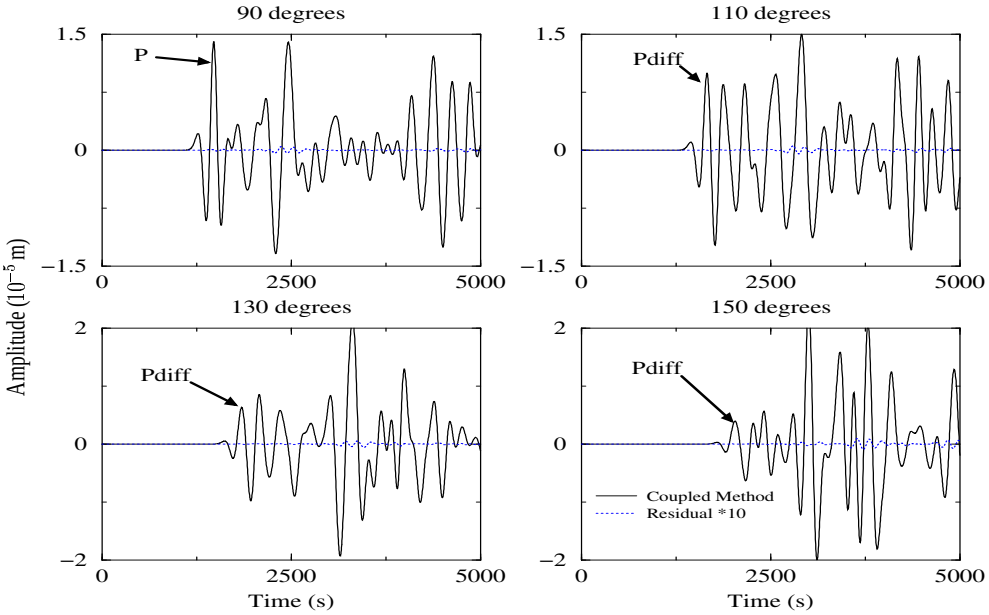

Figure 2.5: Vertical component seismograms recorded at 90°, 110°, 130° and 150° of epicentral distance in the homogeneous sphere with a liquid inclusion. The solid line is the coupled method solution and the dotted line represents the residualx10 when comparing with the normal mode summation solution (the normal mode summation solution is not represented because there is no visible difference with the coupled method solution).

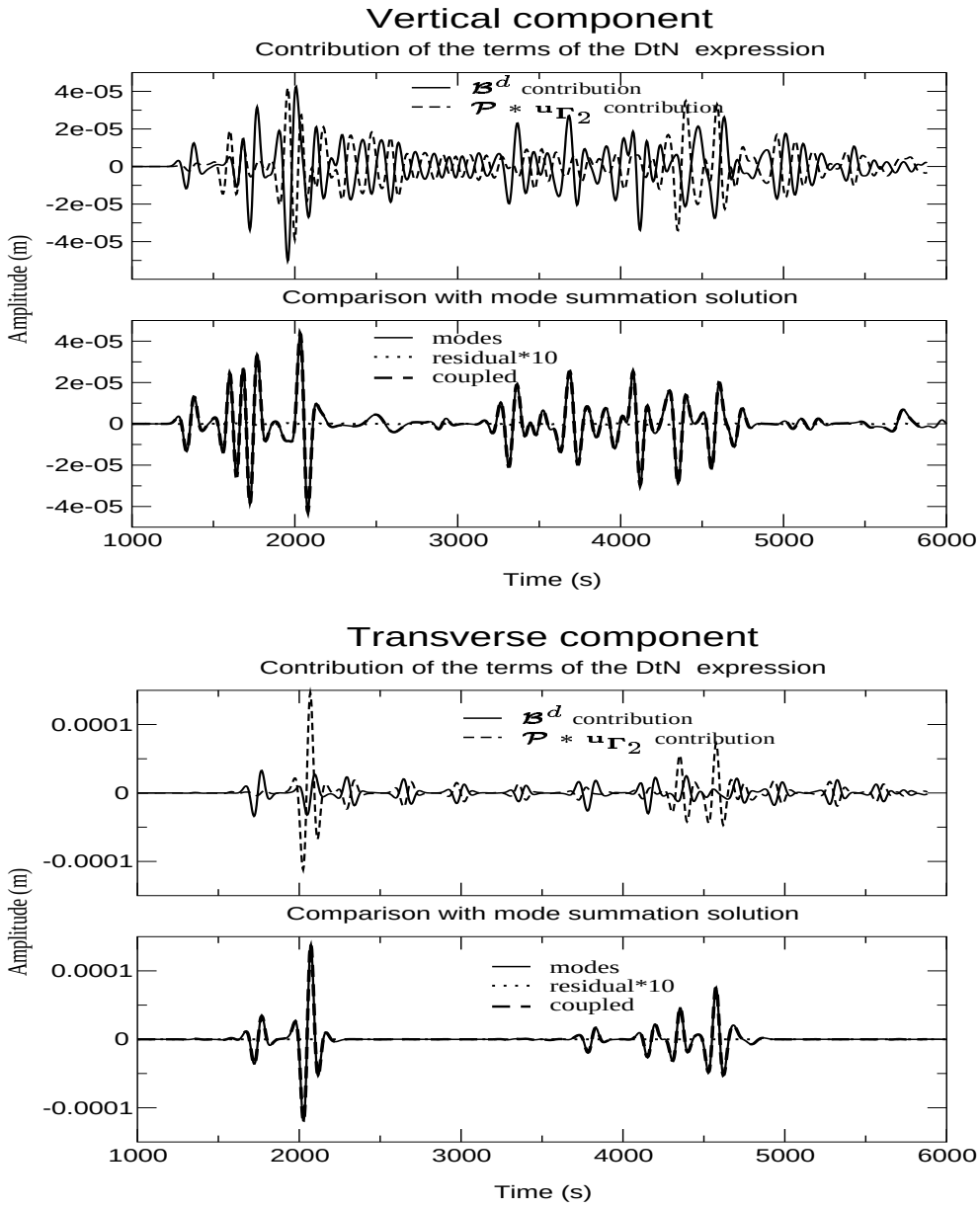

Figure 2.6: Vertical and transverse displacement records at an epicentral distance of 107° in a homogeneous sphere. The top plot for each component represents the contribution to displacement of the two terms of equation (2.9). The bottom plot presents comparisons with normal mode summation solutions.

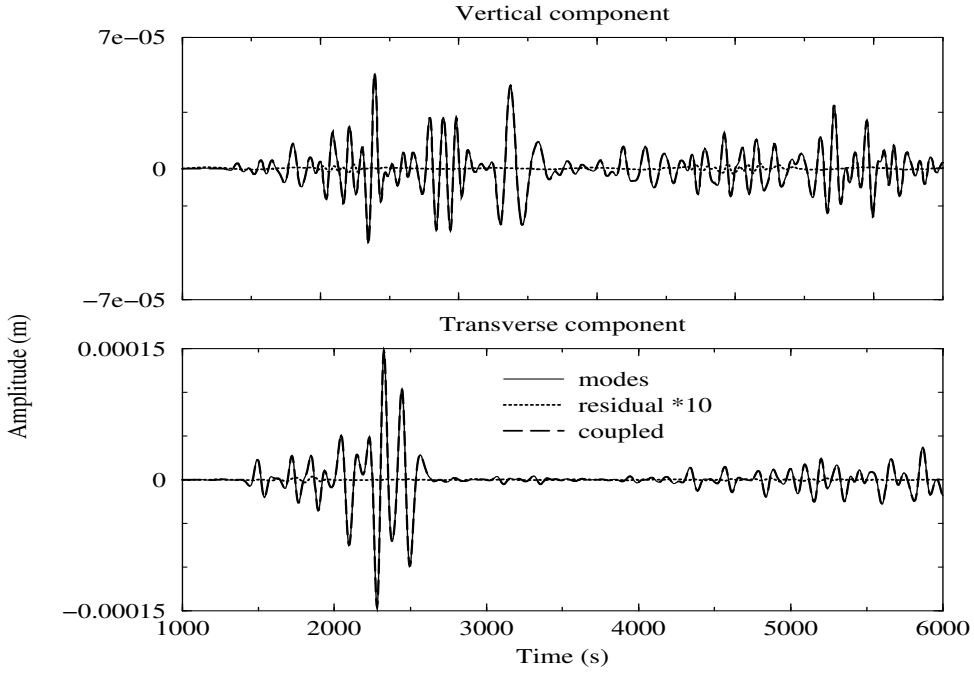

Figure 2.7: Vertical (top) and transverse (bottom) displacement records computed by modes summation (solid line) and by the coupled method (dashed line). The difference between the two solutions time 10 (dotted line) shows a very good agreement.

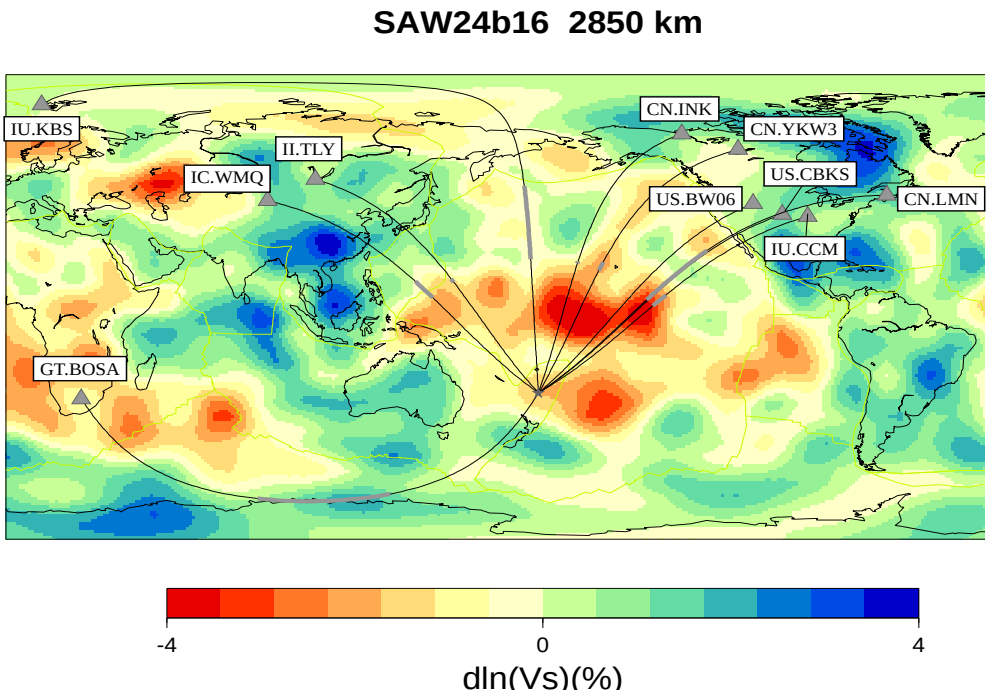

Figure 2.8: Configuration of source and stations used in this example. The background model is the tomographic model SAW24B16 above the CMB. Path between source and stations are plotted, and in bold is plotted the part of the path that would sample the D" layer in PREM.

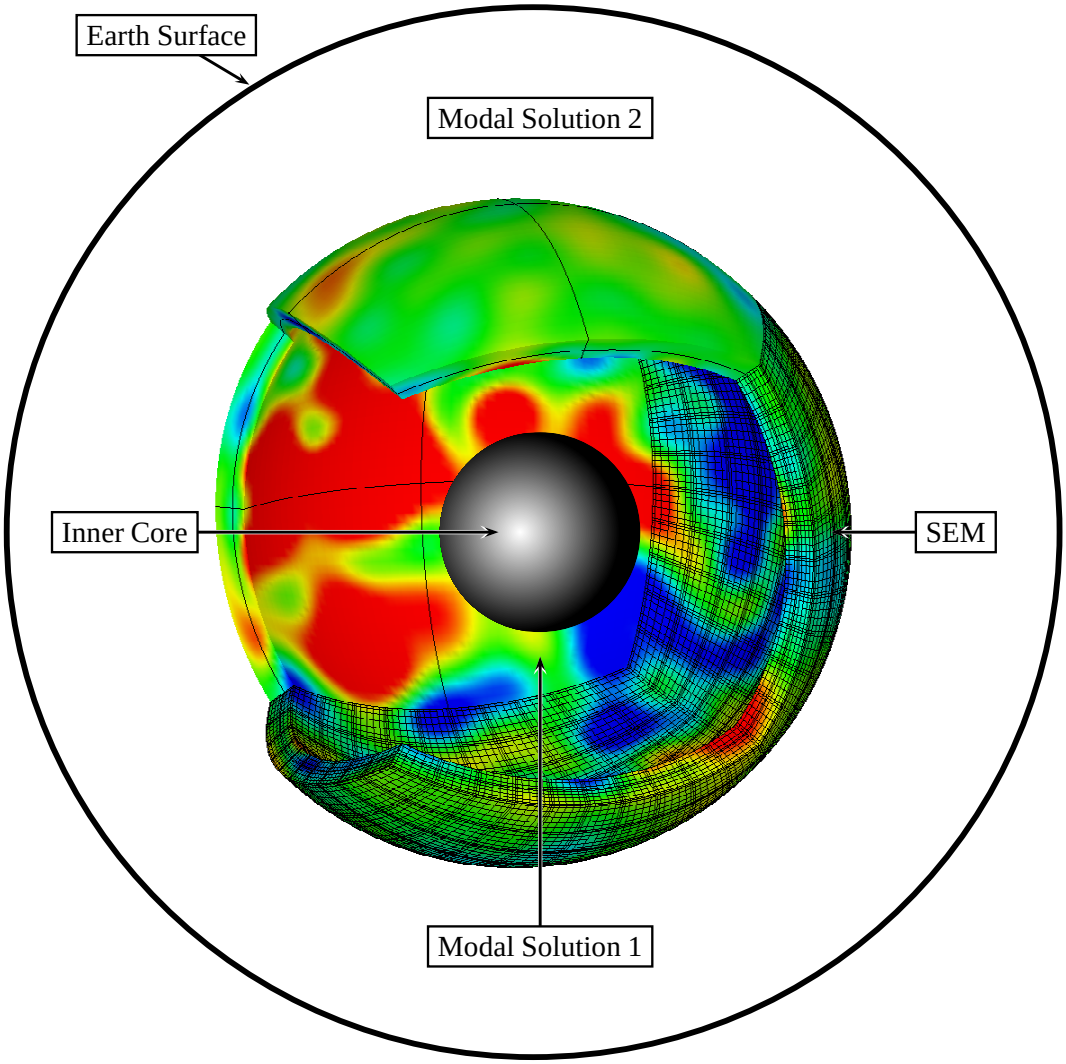

Figure 2.9: Sketch of the configuration used in this example. The spectral element mesh is represented with 4 times less elements in each horizontal direction that 4 times less GLL points in the vertical direction there are actually for visibility purpose. In color in represented the S wave velocity contrast compared to PREM from the tomographic model SAW12B16.

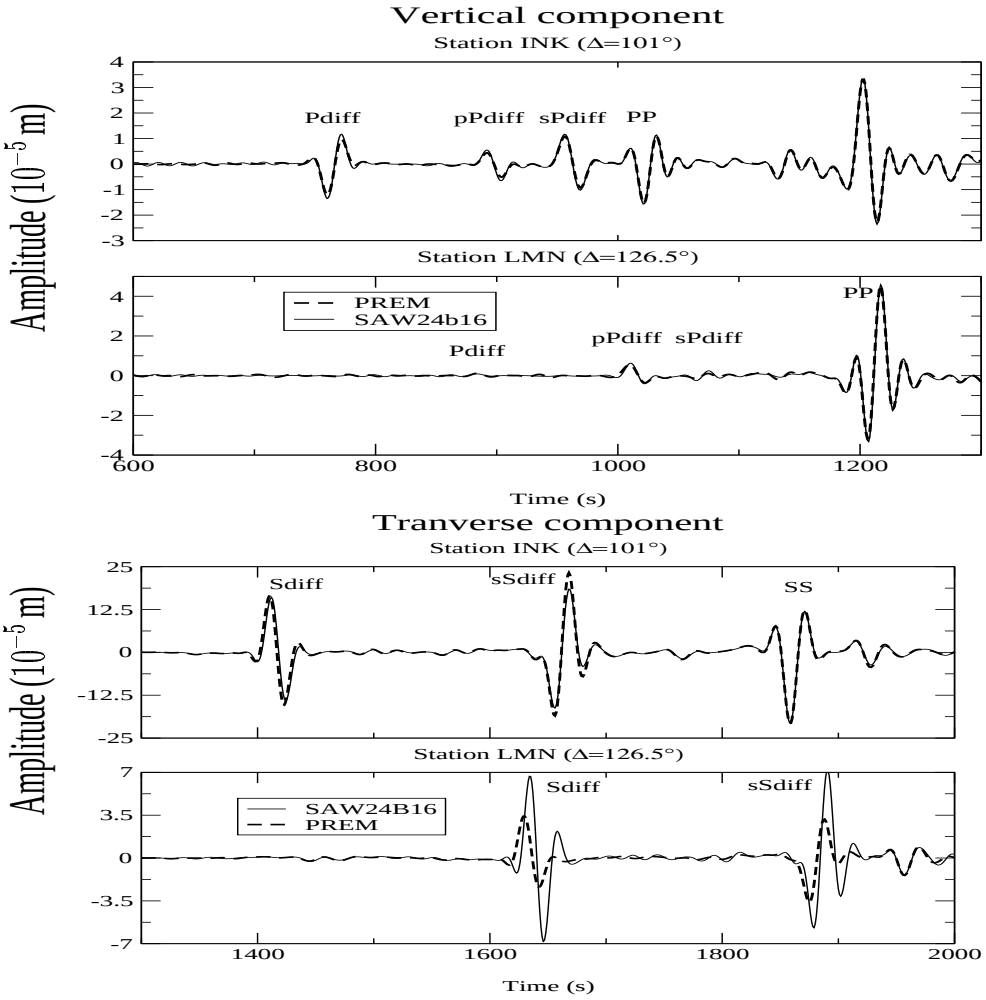

Figure 2.10: Vertical (top) and Transverse (bottom) synthetics computed in PREM and SAW24B16 for two stations. The effect on SHdiff is strong at large epicentral distance especially on the amplitude (a factor two).

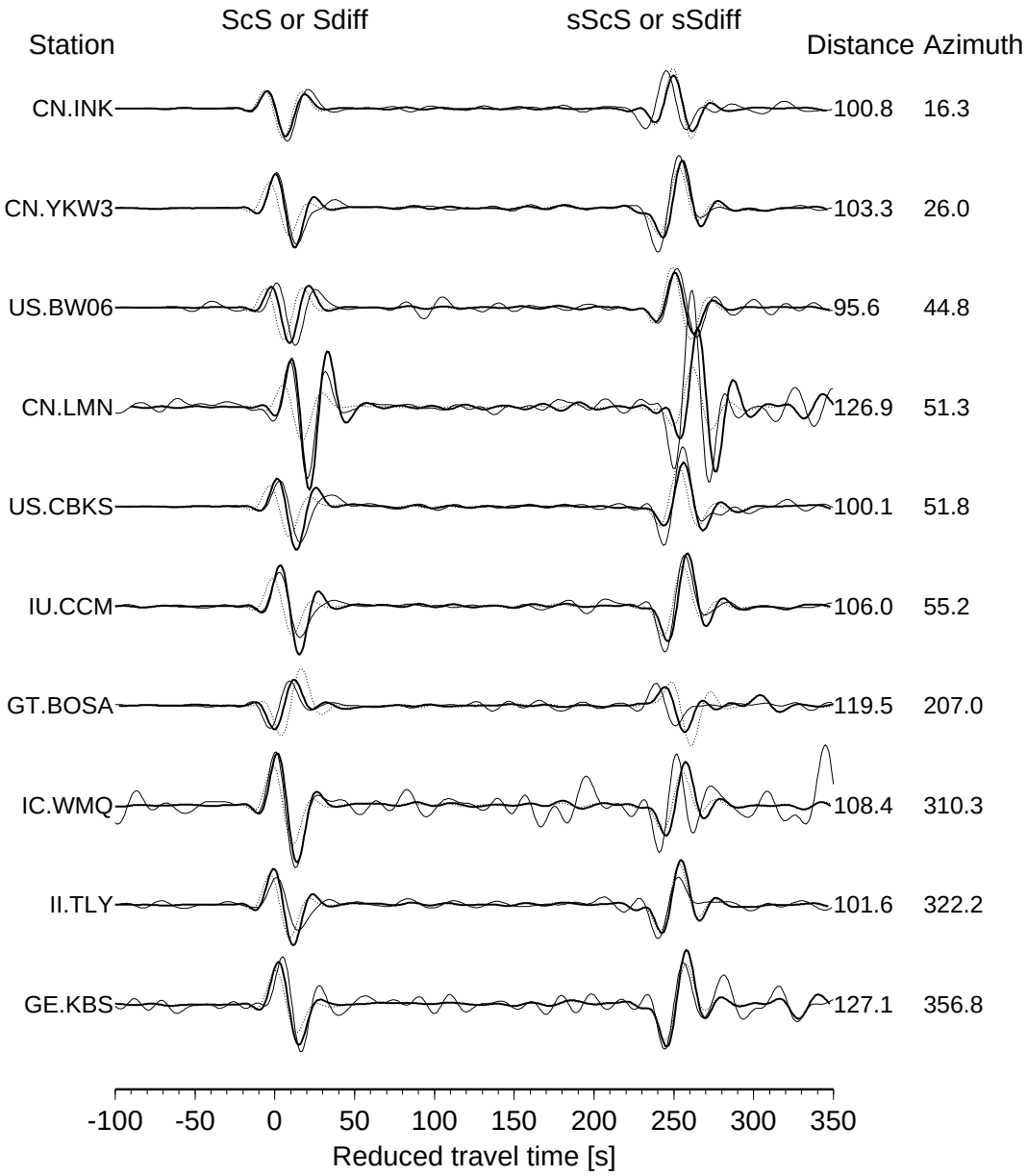

Figure 2.11: Comparison between data (thin line), synthetics in PREM (dotted line) and synthetics in SAW24B16 + PREM (bold line).

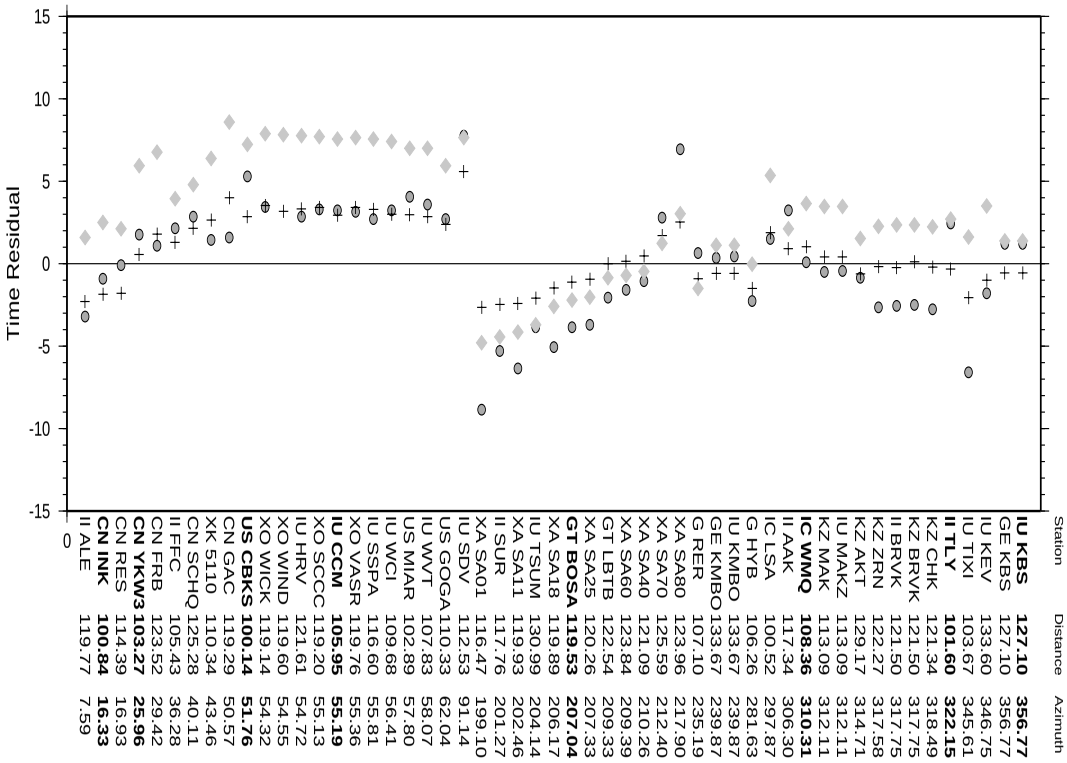

Figure 2.12: Time arrivals of ScS or Sdiff phase computed by linearized ray tracing (diamonds) and by the coupled method using waveform cross-correlation (crosses) for a large number of stations in SAW24B16 model in the D" region. The station name for which waveforms are plotted on figure 2.8 are printed in bold. The time arrivals of data are also plotted (circles).

Chapter 3

3D effects of sharp boundaries at the borders of the African and Pacific superplumes; observation and modeling

This chapter has been published in *Earth and Planetary Science Letters* [*To, Akiko; Romanowicz, B; Capdeville, Y; Takeuchi, N*] with the title ’3D effects of sharp boundaries at the borders of the African and Pacific superplumes; observation and modeling’

Summary

We report that a sharp lateral boundary exists at the southern edge of the Pacific superplume. The set of SHdiff waveforms, which graze the South Pacific, have similar features to those observed previously at the southeastern edge of the African superplume. Both waveform sets show a rapid shift of the arrival time and the broadening of the waveforms with respect to the azimuth as previously reported in the case of the African plume. We also document here that they both show a secondary pulse that follows the direct Sdiff phase. The coupled mode/spectral element method, which can handle strong lateral variations of shear velocity in D", is used to construct synthetic waveforms. The postcursors can be explained by simple effects of 3D structure in the D” region with a sharp quasi vertical boundary aligned almost parallel to the ray path. The existence of these pulses suggests that modeling of heterogeneity outside of the great circle path can help constrain the 3D structure at the base of the mantle. When including 3D effects in the modeling, we find that the velocity contrast across the sharp boundary is of the order of 4-5%, averaged over the last 300 km of the mantle, which is smaller than has been proposed in some studies, but larger than in existing tomographic models, implying that the “superplume” features at the base of the mantle cannot be purely thermal. The similarity of the two observed SHdiff waveform sets at relatively high frequencies indicates that the low velocity regions in the lower mantle under Pacific and Africa, corresponding to the strong degree-2 pattern in shear velocity tomographic models, have a similar nature also at finer scales.

3.1 Introduction

Global shear velocity tomographic models show two large-scale low velocity structures in the lower mantle, one under southern Africa and the other under the mid-Pacific ([*Grand* , 2002; *Gu et al.*, 2001; *Mégnin and Romanowicz*, 2000; *Masters et al.*, 2000,; *Ritsema et al.* 1999]). The long wavelength structures of the so-called superplumes are consistent between different models and they extend laterally for several thousand kilometers. However, disagreement remains in the finer scale structures, which are better resolved by forward modeling techniques. More detailed images of the strength and shape of the slow anomalies are often obtained by matching the travel time data and waveforms of various lower mantle sensitive phases such as ScS, S, SpdKS, SKKS, SKS and Sdiff [*Tanaka and Hamaguchi*, 1992; *Garnero and D Helmberger*, 1993; *Wysession et al.*, 1994; *Ritsema et al.*, 1998; *Wysession et al.*, 2001; *Bréger et al.*, 2001].

Recently, sharp lateral transitions in the velocity structure at the borders of the superplumes have been reported. Most of the findings are associated with the African superplume [*Wen*, 2001; *Ni et al.*, 2002]. Steep gradients of the shear wave velocity are observed on the east and west sides of this prominent low velocity feature, which extends 1500km above the CMB [*Ni et al.*, 2002]. Furthermore, on the southeastern edge of the African anomaly, sharp transitions are observed at the north and south sides of the kidney shaped slow anomaly (shown as a brown dashed line in Fig. 3.1) that lies on the CMB [*Wen*, 2001; *Ni et al.*, 2005].

There is also evidence of sharp velocity gradients around the Pacific superplume. A large 8% lateral shear velocity drop in D" has been observed in the northeastern Pacific with a localized region of fast anomaly adjacent to the edge of the superplume [*Bréger and Romanowicz* , 1998].

The two prominent low S velocity features in the Pacific and under Africa have been interpreted as large scale upwellings, with higher than average temperature, possibly representing the return flow from subduction [*Hager et al.*, 1985]. The low velocities are anticorrelated with bulk sound speed [*Robertson and Woodhouse*, 1996; *Su and Dziewonski* , 1997], and may be associated with higher than average density [*Ishii and Tromp*, 1999]. Their detailed features are not resolved yet, in particular whether the corresponding upwellings are broad or consist of a large number of narrow plumes [*Schubert et al.*, 2004]. The sharp velocity contrasts documented in some previous studies [*Ritsema et al.* 1999; *Wen*, 2001; *Ni et al.*, 2002; *Ni et al.*, 2005; *Bréger and Romanowicz* , 1998] also indicate that the nature of the superplumes cannot be purely thermal. Constraining the gradients across their boundaries and the detailed structure within them is therefore crucial to furthering our understanding of the dynamics of the mantle.

We focus on two points in this paper. First, we show that a sharp vertical boundary also exists at the southern edge of the Pacific superplume. The set of SHdiff waveforms, which sample D" in the South Pacific, have similar features to those observed at the southeastern edge of the African superplume [*Wen*, 2001; *Ni et al.*, 2005]. Second, we show that the

waveforms from Africa and the South Pacific exhibit not only rapid travel time shifts, but also multiple pulses, for paths sub-parallel to the sharp boundary, in its vicinity. We use the coupled mode/spectral element method (CSEM in what follows) [*Capdeville* ,2000; *Capdeville et al.*, 2002; *Capdeville et al.*, 2003] to construct synthetic waveforms in 3D models of D" and show that these first order features and their trends with azimuth can indeed be produced by 3D effects from a simple structure with a strong sharp quasi vertical boundary aligned almost parallel to the ray path.

3.2 Data

The locations of the events and stations used are displayed in Figure 3.1. We considered earthquakes with depths of 100 km to 680 km and $M_w \geq 6.1$. Broadband seismograms were collected from the IRIS/GSN and IRIS/PASSCAL networks. Figure 3.2 shows the observed Sdiff waveforms for an event in the Fiji-Tonga region (19970904) recorded at the stations of the Tanzanian array in Africa. The locations of raypaths are shown in Fig. 3.1. Waveforms are aligned with respect to the Sdiff arrival time predicted for PREM and shown in order of increasing azimuth. As the azimuth increases, the ray paths start to enter the slow anomaly that lies to the north (Fig. 3.1). The first two panels from the left show transverse and radial components respectively, to which a zero-phase butterworth filter has been applied, with corner frequencies of 0.01 and 0.2 Hz. A bandpass filter with slightly

different high corner frequencies is applied to the traces of the third and fourth panel, to match the filters used later in the synthetic computations. The high frequency corners are at 0.09 Hz and 0.078 Hz respectively.

Figure 3.3 shows the SHdiff records of Fiji and Tonga events recorded at station BDFB of the Global Telemetered Southern Hemisphere Network (GTSN), in Brazil. The source information for each event is given in Table 3.1. The SH radiation patterns for the Harvard CMT solution (http://www.seismology.harvard.edu/CMTsearch.html) are shown in Figure 3.4. The waveforms are corrected for source polarity according to the latter solution. The raypaths of these waveforms are shown in thick yellow lines in Figure 3.1: they sample the southern Pacific. The configuration of the events and stations is different from that of the African case (Fig. 3.2) in that we look at waveforms from many events recorded at a single station, whereas waveforms from one event, recorded at many stations, are aligned in the African case. This is because there is at present no dense array in South America that would sample this region. Consequently, the waveforms of (Fig. 3.3) are shown in order of back azimuth. The waveforms look alike, despite the fact that we are comparing waveforms from earthquakes with different sizes, depths and mechanisms, and with possible shifts due to errors in the event location and timing. A clear time delay of about 13 seconds of the top trace, which samples the north, compared to the bottom trace, which samples the south, is observed. The S phase waveforms recorded at the closer station RPN, at distances of 61 to 64 degrees (Fig. 3.1), show relatively simple pulses (Fig. 3.5) and do not show

either secondary pulses or the rapid time shift with respect to the back azimuth. Especially the waveforms from the event 20000614 show the distinct difference between a simple S phase and a complex SHdiff phase. These comparisons confirm that the travel time shift and the secondary pulses in the SHdiff phase reflect an anomalous structure and are not due to features in the source process. There is no systematic trend in the radiation pattern (Fig. 3.4) and the size and depth of the earthquakes (Table 3.1) with respect to the back azimuth, which also indicates that the features of Sdiff phase are not due to the source processes, or to structure in the vicinity of the source.

These SHdiff waveform sets, which sample the southeastern edge of the African slow anomaly (hereafter ASA) and the southern edge of the Pacific slow anomaly (hereafter PSA), are very similar in the following ways. First of all, the onset times of the first arrivals change very rapidly, or show a sudden jump with respect to the change of azimuth or back azimuth. The thick grey lines in Figure 3.2 and Figure 3.3 follow the trough of the first arrival. In the case of ASA, the first arrivals shift about 15 seconds within an 18 degrees change of azimuth. In the PSA case, the arrival time changes about 13 seconds within 18 degrees change in back azimuth. Second, the waveforms, which graze the transition from fast to slow, show an additional pulse indicated by solid dots and solid black lines in Figure 3.2 and Figure 3.3. In the ASA case, as raypaths start to sample the slow anomaly, this pulse comes closer to the first pulse, and it finally merges with the latter at an azimuth of 218 degrees. In other words, the solid black lines, which follow the second pulse, have the opposite slope from the grey lines that follow the first pulse (in the right 2 panels of

Figures 3.2 and 3.3). This later phase is the feature we model in the following section. Third, when we look at the higher frequency components of these waveforms, there are yet additional pulses that can be followed for a certain azimuth range. These pulses are shown by the open circle dots in the first panel of Figure 3.2 and 3.3.

In order to confirm that the travel time shift observed in PSA is due to heterogeneity at the base of the mantle, we measured the differential travel times of Sdiff-SKKS(Figure 3.6). We measured them for all the paths shown on the Pacific side in Figure 3.1. The differential travel times are less affected by the uncertainty in the source location and the origin time than for absolute Sdiff. In addition, because the raypaths of Sdiff and SKKS are close to each other in the upper mantle, they are more sensitive to heterogeneity at the base of the mantle. Both Sdiff and SKKS travel times are measured by taking cross correlations between observed waveforms and PREM synthetic waveforms constructed by normal mode summation down to 5 seconds.

A bandpass filter with corner frequencies of 0.01 and 0.058 Hz is applied to the Sdiff phase and a filter with corner frequencies of 0.01 and 0.2 Hz is applied to the SKKS phase to measure the travel times. Relatively low frequency components are used for the Sdiff measurement because the Sdiff waveforms look complex, with many high frequency pulses, as shown in the first and third panels of Figure 3.3. Taking the cross correlation is difficult in such cases and results in the reduction of the number of usable data. High frequency components are used for the SKKS measurements to avoid contamination by other phases

such as SKKKS, which arrives close to SKKS. When measured using different frequency ranges, including down to 0.2 Hz for Sdiff and 0.058 Hz for the SKS, the measured travel times shift globally by a few seconds. However the relative travel time differences between the stations, which are the focus here, change by less than 1.5 seconds.

The result of the travel time measurement is shown in Figure 3.6 with respect to the latitude of the point where Sdiff first reaches the CMB on the source side. An ellipticity correction [*Kennett, and Gudmundsson*, 1996] is applied to each datum. The residuals of Sdiff-SKKS for the station BDFB (gray diamonds in Figure 3.6) show a steep gradient of 10 seconds within a latitude change of 10 degrees. This indicates that the rapid shift of the arrival time shown in Figure 3.3 is neither due to the mislocation of events nor to upper mantle heterogeneity. This shows that the sharp lateral transition in shear velocity anomaly lies between the two regions where the SKKS raypaths enter and exit the outer core (shown by yellow diamonds in Fig. 3.1). The data points for stations other than BDFB also show that the Sdiff-SKKS residuals increase toward the north up through a latitude of around -20 degrees. The residuals decrease again north of latitude of -15 degrees, suggesting a rapid exit from the low velocity region, but this feature is not discussed further in this paper.

3.3 Modeling from simple structures

We used a coupled mode and spectral element approach (CSEM in what follows) [*Capdeville* ,2000; *Capdeville et al.*, 2002; *Capdeville et al.*, 2003] for the waveform modeling. The study of strong lateral variations in the D" region is best addressed by a forward waveform modeling approach that can handle 1) the propagation of seismic waves in 3D models with strong lateral variations and in spherical geometry and 2) diffracted waves along the core mantle boundary. The most promising method at the present time, the spectral element method (SEM), remains computationally heavy. To address the study of heterogeneity in particular regions, such as D", Capdeville ([*Capdeville* ,2000]) developed a hybrid method that couples spectral element computations with a normal mode solution, so that the spectral element method is used only in the target strongly heterogeneous regions. The modal solution provides a fast and precise solution in regions of the Earth where a model with spherical symmetry can be considered. This approach has been extended to the case of a heterogeneous shell "sandwiched" between two spherically symmetric shells [*Capdeville et al.*, 2003; *To et al.*, 2003]. In this study, SEM is used for the bottom 370km of the mantle.

In the first part, we show that synthetic waveforms constructed from simple models with vertical boundaries can explain the first order features of the observed waveforms. The models have the 1D structure of PREM down to a depth of 2591 km, and the 3D model below 2591km, down to the CMB. The 3D part of Model 1 is divided into 4 quadrants as shown in Figure 3.7a so that we can test different models with the same CSEM run. Each

quadrant in Model 1 has either -3% or +3% constant S velocity anomaly with respect to PREM. The portion of the Sdiff raypaths, which goes through the bottom 300km of the mantle, is shown in thick lines. The source mechanism is set to have its maximum SH radiation around the maximum gradient of lateral heterogeneity. The two boundaries on the right and top (i.e. pointing 0N and 90E) are sharp and the other two on the left and bottom (i.e. pointing 180S and 90W) are more gradual. The 6% velocity jump occurs within a distance of 3 degrees for the sharp boundary and within 10 degrees for the gradual boundary. The sharp boundaries are shifted 13 degrees from the great circle that goes through the source (shown by a dashed line). The gradual boundaries lie between 5 degrees and 15 degrees from the great circles. Model 2 (Fig. 3.7b) has an S velocity anomaly of -2% and +2% in the fast and slow region, respectively. The 4% shear velocity jump occurs within 7 degrees. The boundaries lie 13 degrees away from the great circles, which are parallel to the boundaries.

Figure 3.5 (a) to (d) show the synthetic waveforms for the stations which are located at the four velocity transition zones of Model 1. The synthetics are computed down to 12 seconds. Each trace is normalized by its maximum amplitude. Bars on the right side show the relative maximum amplitude. Long bars indicate that the traces have large maximum amplitudes. The four panels show different combinations according to whether the interface is sharp or gradual and whether the source is located on the slow or fast side of the interface. In all four cases, we observe multiple pulses for paths which interact with transitions in the velocity structure. The comparisons between (a) and (c), and between (b) and (d) show that a

sharper boundary produces a multiple pulse in a wider range of azimuths. When the source is located in the slow region (Fig. 3.5 (a) (c)), the secondary pulse, indicated by dashed lines, is observed at stations in the slow regions, such as stations 23-41 for (a), 203-221 for (c). By inspecting the corresponding particle motions, we infer that this corresponds to paths which are radiated toward the fast region from the slow region, turn within the velocity gradient and propagate toward the stations in the slow region. The estimated bent raypath is shown in Figure 3.7(a) for station 205 of Model1. The path is estimated by setting the lateral turning point of the ray in the middle of the diffracting potion on the CMB. When the path from the source enters D" in the fast region ((b), (d)), a secondary phase due to multipathing is observed, as indicated by the solid black lines in Figure 3.5 (b) and (d). It is observed at stations 81-105 for (b), 261-281 for (d). The first arrival at these stations is a wave which is refracted at the boundary from the fast to slow region. For example, the refracted raypath for station 89, estimated from the particle motion, is drawn in Fig 3.7. The secondary phase at these stations is a wave which propagates directly from the source without bending much, sampling the slow region in D". The move out of the phase indicated by the black line is observed at stations in the fast region or at the border, such as stations 101-105 and 277-281. We believe this is a diffracted wave originating from the scattering point where the boundary of the fast and slow region meets the 1D PREM at 300km above the CMB, and is therefore an unrealistic feature of the model. Figure 3.5 (e) and (f) show the result for Model 2, which has a smaller shear velocity transition (from -2% to 2%). The source is located on the slower side in (e) and the faster side in (f). Explanation

of the phases shown by solid black and dashed lines are the same as above.

Among the six panels in Figure 3.5, the waveforms of panel (f) show features which resemble the observations most. The velocity contrast at the boundary is 4% and the source is located on the fast side of the boundary. A more direct comparison between the synthetic and observed waveforms is shown in Figure 3.9 . Although there are some differences, they all have the common feature of one trough followed by two peaks. The waveforms are compared with different time scales and frequency ranges, to show the qualitative similarity between them. The time scale of the synthetics is stretched compared to that of the observed waveforms. This is because of the frequency limitation of the present SEM calculations, which is dictated by the computer power available to us. Although synthetics were calculated down to 8 seconds in the next section, it is limited down to 12 seconds here due to the heavy computations. In the comparison shown in Figure 3.9, we have chosen a station, which clearly shows two separate pulses in the synthetics. As the second pulse moves closer to the first one (229-231 of Model 2), these pulses blend into a single broadened pulse because frequency resolution is not good enough. Calculations of the CSEM synthetics to higher frequencies would allow a better separation of these pulses for paths close to the vertical boundary, as seen in the observations. The waveforms from Model 2 look more similar to the data than Model 1, which provides constraints on the appropriate velocity contrast to match the observations. As shown later, the velocity contrast which explains the Sdiff travel time measurements in the case of ASA is about 4% and it is consistent with Model 2. The first arrival of Model 2 station 247 is a refracted wave from the

fast region to the slow region (similarly to station 89 in Model 1, Fig. 3.7a). In Model 1 however, the bending of the ray at the boundary is large and creates a large shadow zone of the first arrival, which does not seem to be present in the observations.

3.4 Modeling based on the tomographic model

In the second part of the modeling, we focus on the kidney shaped slow anomaly in Africa. As shown in the previous section, the cause of the multiple pulses depends on the geometry of the source and receiver, and the location of the boundary. Based on the SH tomographic model [*Mégnin and Romanowicz*, 2000], we constructed a model which generates the secondary phase (solid black lines of Fig. 3.2). The result gives insight of where and how the secondary arrivals are produced in the African data. Figure 3.10 presents equidistance projections of the kidney shaped anomaly. The source, in the Fiji-Tonga region, is plotted at the apex. The left panels show the original SAW24B16 model. The right panels show a modified model. The contour line of 0(%) anomaly of the original tomographic model is kept fixed. The velocity anomaly is saturated to -2.75(%) in the slow regions and 1.75 (%) in the fast region, between the CMB and 300 km above the CMB. These values are chosen to fit the travel time measurements of the Sdiff phase. The transition to the 1D model above 370 km from the CMB is here smooth, to avoid artificial effects in the vertical plane. Figure 3.11 shows the synthetic waveforms calculated down to 8 seconds. The calculation to high

frequencies is necessary because the secondary arrival cannot be distinguished for some paths when periods shorter than 12 seconds are not included, as shown in Figure 3.2. The synthetics from the original tomographic model (Fig. 3.11 left panel) do not generate the secondary arrival or the rapid shift of the first arrival. On the other hand, the synthetics from the modified model with the sharp boundaries (Fig. 3.11 right panel) capture the features of the observed waveforms. The move out of the secondary arrival, which actually appears in multiple branches, shows a slope which is consistent with observations, although it appears at a slightly different azimuth. Moreover, the jump of the first arrival occurs around the azimuth of 215 degrees which is also consistent with the observations. Figure 3.12(a) and (b) shows the synthetic and observed particle motions at the station corresponding to an azimuth of 210.26 degrees. The particle motion of Sdiff phase in 1D PREM model(shown by a grey line) shows almost purely tangential motion at the azimuth of maximum SH radiation. The synthetic particle motion indicates that the first pulse arrives from the southern side and the second pulse arrives from the northern side. Although the timing of the second arrival is not quite consistent, the observed particle motion also follows a similar trend. Both the first and second arrivals are estimated to be refracted waves and their paths are described schematically in Figure 3.10 by yellow and green lines, respectively. We should point out, however, that only several observations show similar particle motion as Figure 3.12(b), and many of the observed traces are complicated or do not show the clear change of the incoming wave direction(Fig. 3.12 (c)(d)). The modified model is consistent with the result from the previous section, where Figure 3.5(f) looked most similar to the data.

In both Figure 3.5(f) and Figure 3.11(b), the source is located on the faster side of the boundary, the velocity jump is 4% and 4.5% respectively, and the multiple pulses are observed at stations located on the slow side.

The particle motions depend also on radiation pattern and anisotropic structure. For example, particle motion plots show evidence for shear wave splitting (elliptical motion) for paths that stay entirely in the fast region (azimuths 199 to 204 degrees)(Fig. 3.11(c)), but remain linear once the paths start interacting with the vertical boundary and for the rest of the azimuth range considered here(Fig. 3.11(d)). This is consistent with the absence of prominent SV energy for azimuths larger than 204 (Fig. 3.2 second panel) and indicates that neither radial anisotropy, as found in many regions in D" [*Panning and Romanowicz*, 2004], nor azimuthal anisotropy can explain the secondary pulses described in this study. We defer a detailed analysis of the full suite of observed particle motions to a future study.

3.5 Discussion and Conclusions

The result from simple models (Fig. 3.7 and Fig. 3.5) shows that when the wavepath in the D" is quasi-parallel to a sharp vertical boundary, the Sdiff waveforms are accompanied by secondary phases. The synthetic tests from the models of Fig. 3.7 give only a qualitative constraint on the model, which is the existence of a sharp vertical boundary in the D” region. However, because SEM includes the 3D effects from strong heteroge-

neous structures, the order of magnitude of the effects on the waveforms is well captured by the simple model. When the boundary is sharper, the secondary phases are clearer and observed in wider ranges of azimuth. These phases can be used as additional constraints on the shape and sharpness of these boundaries. There are features in the synthetic waveforms of Figure 3.5, which are not seen in observed waveforms. They are indicated by grey dots, and are observed at those receivers, where the wave paths only sample the slow anomaly regions and do not interfere with the lateral heterogeneity. Therefore, we think the pulses are due to the vertical velocity change in the synthetic model, which is the sudden reduction of velocity at 300km above the CMB. Various vertical structures should be examined and adjusted more carefully in future studies.

The synthetics from the more realistic model of Figure 3.9 indicates that the postcursors of ASA data are refractions from different sides of the kidney shaped boundary. This suggests that the details of the shape and anomaly contrast at the boundary can be obtained by fitting the timing of the emergence of the postcursor. Although there are some differences, the timing of the first arrival and the slope of the secondary arrival are consistent between synthetics and observations. This indicates that the shape of the anomaly is well described in the existing tomographic model, in spite of the fact that only 2D kernels within the great circle were used to make the original model [*Mégnin and Romanowicz,* 2000]. The gradient of the anomaly is less well constrained, as previously discussed in the case of Africa by [*Ritsema et al.* 1999] and in the case of the Pacific by Bréger and Romanowicz [*Bréger and Romanowicz* , 1998]. Observation of refracted waves outside of the great

circle suggests the importance of including 3D effects for detailed modeling of the velocity anomalies at the base of the mantle. These effects should also be examined carefully when attenuation measurements are made in regions with sharp lateral heterogeneity, or more generally, when modeling amplitudes of low pass filtered records.

The observed waveforms of ASA (Fig. 3.2) are presented in other papers [*Wen*, 2001; *Ni et al.*, 2005]. Wen [*Wen*, 2001] proposed a model where the thickness and velocity of the low velocity region varies from a 12km thick layer with -12% velocity reduction on the south side, to a 180km thick layer with negative velocity gradient of -2% at the top and -9% at the CMB on the north side. The shape of the slow anomaly region in Wen's model is consistent with this study, however, his modeling requires a large velocity contrast. In his study, only 2D heterogeneity along the great circle was taken into account to construct the synthetic waveforms for the modeling. The postcursors were interpreted as reflections inside the low velocity layer on the CMB, in the vertical plane. In contrast, we interpret the secondary pulses as arising from interactions with the vertical boundary, in the horizontal plane. Since the D" region is characterized by strong heterogeneity having a broad spectrum of scale lengths, it is important to identify whether the secondary pulses are caused by vertical or lateral heterogeneity. Different interpretations result in quite different models [*Liu et al.*, 1998; *Cormier*, 1985; *Haddon and Buchbinder*, 1986]. Our result is consistent with [*Ni et al.*, 2005]. Here, we show that the observed multiple pulses can be produced from relatively simple structures. In addition to the pulses pointed out in [*Ni et al.*, 2005] (shown by grey lines in Fig. 3.2), we show that the observed Sdiff phase is followed by a postcursor (shown

by solid black lines in Figure 3.2, 3.3 and 3.5), which can be explained by a strong vertical boundary. The emergence of pulses due to heterogeneity outside of the great circle are more consistent with the data than effects from horizontal layering. Furthermore, by considering 3D effects, we find that a relatively small velocity contrast across the vertical boundary (but stronger on average over the last 300 km of the mantle than in current tomographic models) is sufficient (about 4%). [*Bréger and Romanowicz* , 1998] obtained a large 8% lateral shear velocity gradient across the northeastern boundary of the Pacific superplume, at the base of the mantle. Similar trends in differential travel time shifts as in Figure 3.6 were measured in that study. Because, in that study, the velocity structure was modified only locally near the CMB, rather than changing the gradient and saturating a large region with constant anomaly, the velocity change may be consistent with what is found here.

We have shown that sharp vertical boundaries exist not only at the border of the African plume but also under the south Pacific. The Sdiff waveforms, which graze these two regions, are similar in that 1) rapid shifts of the first arrival time with respect to azimuth are observed; 2) secondary phases, which accompany the Sdiff phase (shown by solid black lines in Figure 3.2 and 3.3) are observed; 3) smaller pulses are observed at higher frequencies, which can be followed in a certain azimuth range (shown by open circles in 3.2 and 3.3). This indicates that the low velocity regions in the lower mantle under Pacific and Africa, corresponding to the strong degree-2 pattern in shear velocity tomographic models, have a similar nature also at finer scales. The velocity contrast found here, averaging 4-4.5%, is smaller than suggested in some previous forward modeling studies, however, it

is still significantly larger than in any recent S velocity tomographic models, which clearly underpredict lateral variations in the last 300 km at the base of the mantle (e.g. [*Ritsema et al.* 1999; *Bréger et al.*, 1998]). Such a large average anomaly over this depth range cannot be due to thermal effects alone and implies that the superplumes carry a distinct compositional component. Unlike the African superplume where the shape and the location of much of the boundaries are revealed thanks to data from dense broadband arrays, large uncertainties remain on the shape of the Pacific superplume. In particular, the locations of northern and western boundaries of the Pacific superplume need to be further investigated, as well as finer scale structure within the superplumes.

Event date	Latitude	Longitude	Depth (km)	Distance (deg)	Back Azimuth (deg)	Mw	Half duration (sec)
1997 05 25	-32.02	-179.95	345.0	113.84	223.7	7.1	8.5
1997 03 21	-31.18	179.90	452.8	114.46	224.37	6.3	3.5
1997 05 03	-31.70	-179.06	119.3	113.5	224.5	6.9	7.0
1996 11 05	-30.95	-179.73	366.7	114.4	224.8	6.7	5.8
1998 07 09	-30.51	-178.71	154.5	114.0	225.7	6.9	6.8
2001 06 03	-29.37	-178.23	199.3	114.3	227.0	7.1	9.3
1994 02 11	-18.89	169.08	223.3	129.9	228.1	6.8	6.5
2000 06 14	-25.45	178.38	615.4	119.02	228.52	6.4	4.1
1994 10 27	-25.75	179.39	540.6	118.11	228.87	6.6	5.2
1998 04 14	-23.73	-179.81	509.6	118.69	231.21	6.1	2.7
2002 06 30	-22.13	179.43	631.6	120.18	232.25	6.4	4.0
1996 04 16	-23.98	-176.47	116.2	116.1	232.9	7.1	9.3
1998 05 16	-22.27	-179.35	608.8	119.17	232.85	6.8	6.5
2002 08 19	-21.74	-179.08	630.9	119.26	233.51	7.6	16.5
1995 01 17	-20.71	-179.13	649.4	119.86	234.47	6.3	3.0
1997 10 14	-21.94	-176.15	165.9	116.9	235.0	7.7	17.9
2002 01 02	-17.63	178.84	680.8	123.15	236.26	6.1	3.0
1998 03 29	-17.57	-178.85	553.7	121.31	237.70	7.1	9.3
2000 05 04	-17.72	-178.31	539.8	120.80	237.87	6.4	4.2
1994 03 09	-17.69	-178.11	567.8	120.65	238.01	7.6	16.0
2000 01 08	-16.84	-173.81	162.4	117.5	241.2	7.2	9.7

Table 3.1: List of events, used in this study and recorded at the station BDFB in Brazil, The waveforms for these events are shown in Fig.3. The origin times and locations are extracted from the Harvard CMT Catalog.

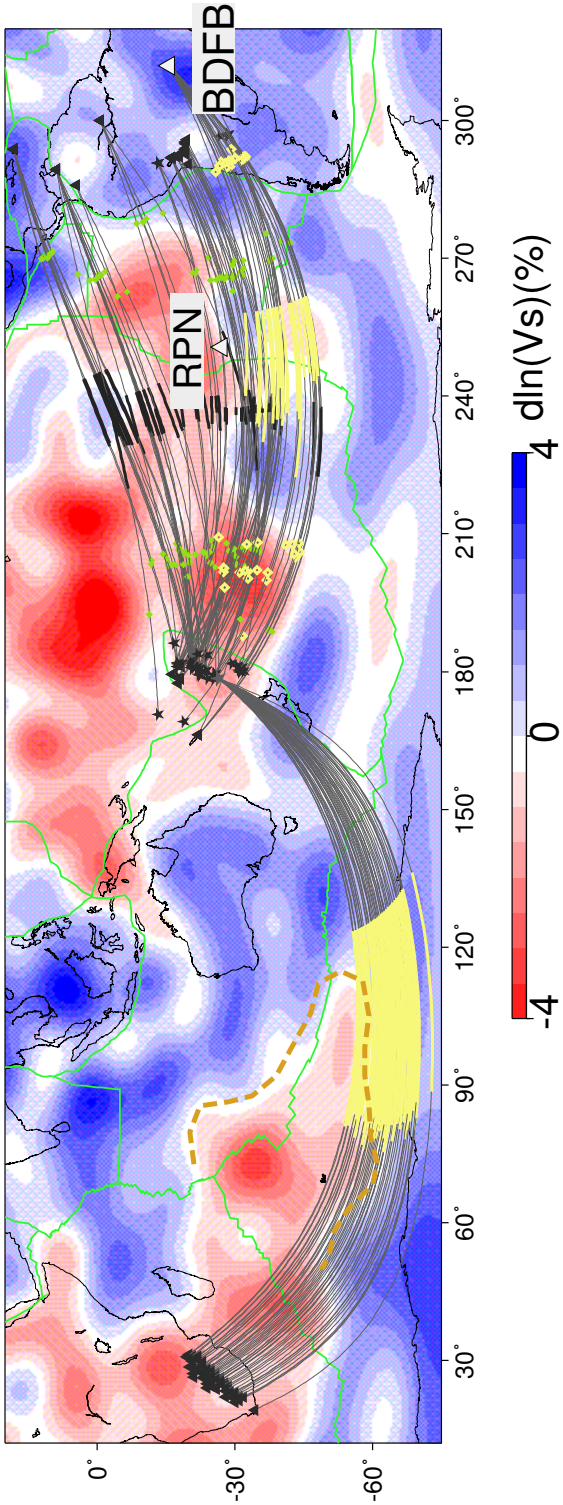

Figure 3.1: Earthquakes (stars), stations (triangles), and projections of the raypaths. Background model is the shear velocity model SAW24b16 [*Mégnin and Romanowicz*, 2000] at the depth of 2850km. The thick lines show the diffracting portion of the paths on the CMB. Thick yellow lines are the paths of the traces whose waveforms are shown in Figure 3.2 and 3.3. Diamonds show the points where SKKS enter and exit the outer core.

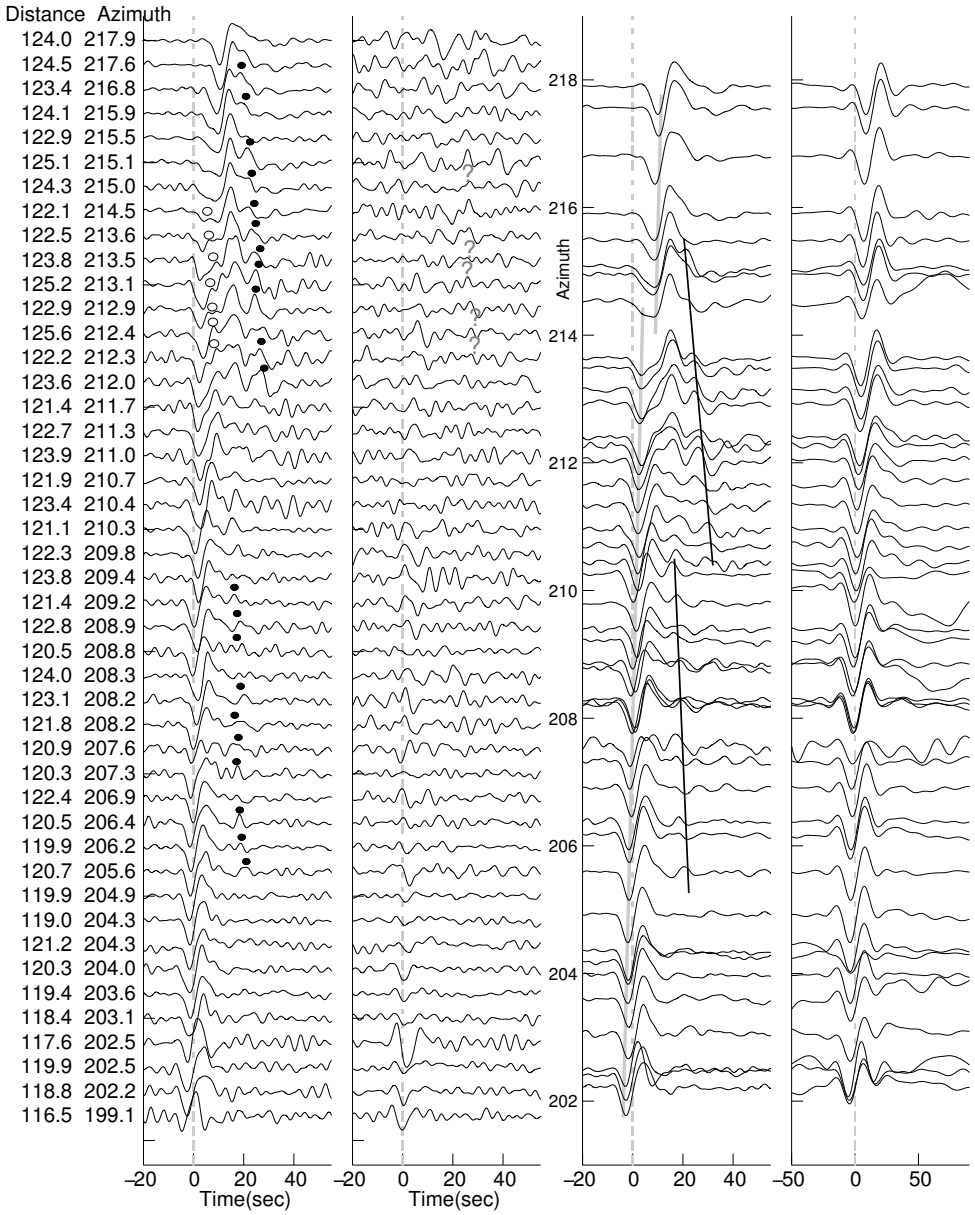

Figure 3.2: Observed velocity waveforms for event 19970904 in Fiji-Tonga (M_w6.8) recorded in South Africa.. Waveforms are filtered in three different ways. First panel from the left: Transverse component bandpass filtered with corner frequencies at 0.01 and 0.5 Hz. The distance and back azimuth of each station are indicated on the left. The broken line is the expected Sdiff arrival for the PREM model. Second panel: Radial component, filtered in the same way as the transverse component. Third panel: Bandpass filtered with corner frequencies at 0.01 and 0.125 Hz. Y-axis shows the back azimuth. Note the different vertical scale compared to the first two panels on the left. Right panel: filtered in the same way as synthetic waveforms in Figure 3.5, with a high end corner frequency at 0.078Hz. With this frequency limit, the multiple pulses are not well separated. Gray lines follow the trough of the first pulse. Black solid lines follow the secondary pulse, which is only observed in the vicinity of the structural boundary.

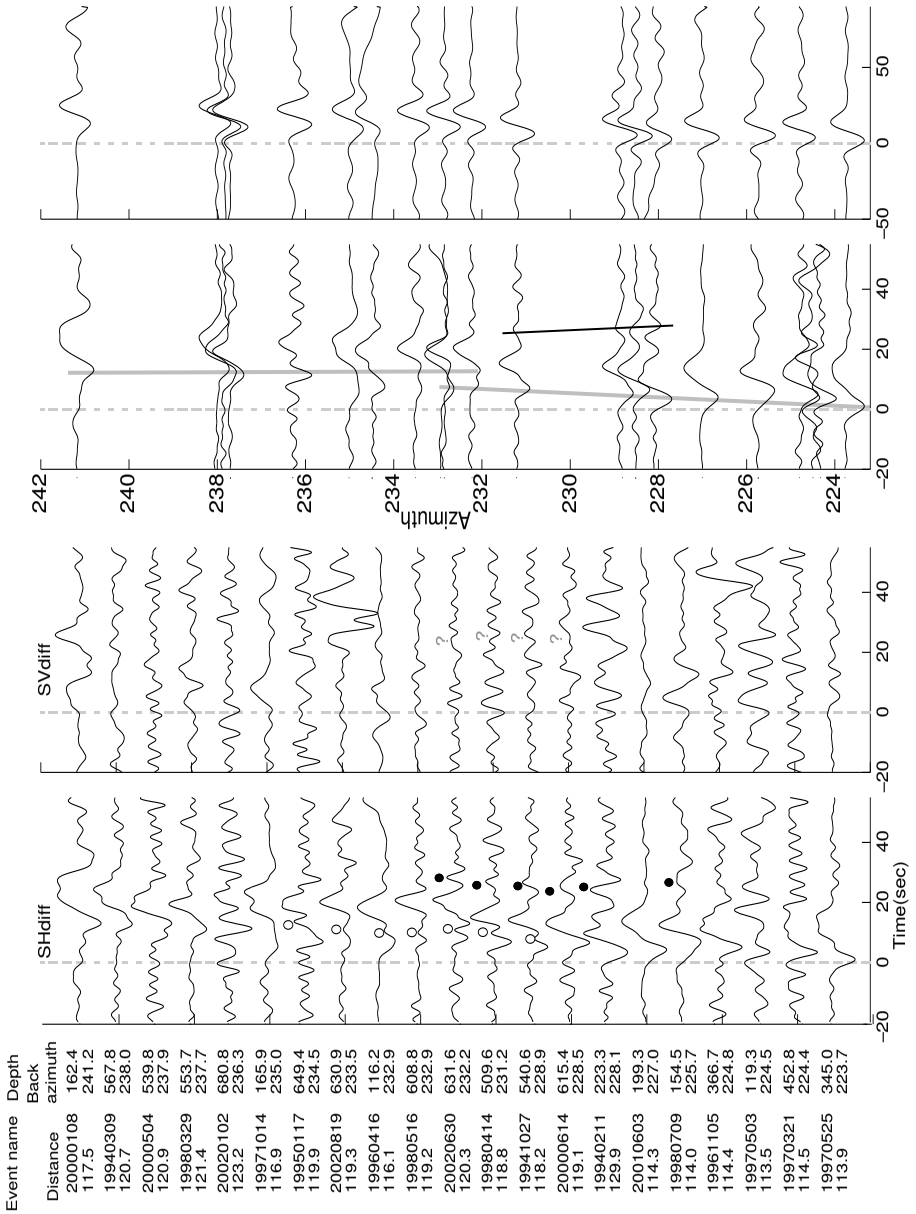

Figure 3.3: Same as Figure 3.2 for 21 events in Fiji-Tonga recorded at the station BDFB in Brazil, ordered as a function of back azimuth. Filtered in the same way as Figure 3.2. The large pulse in the radial component of event 20020819 is a contamination from an event which occurred 7 minutes later.

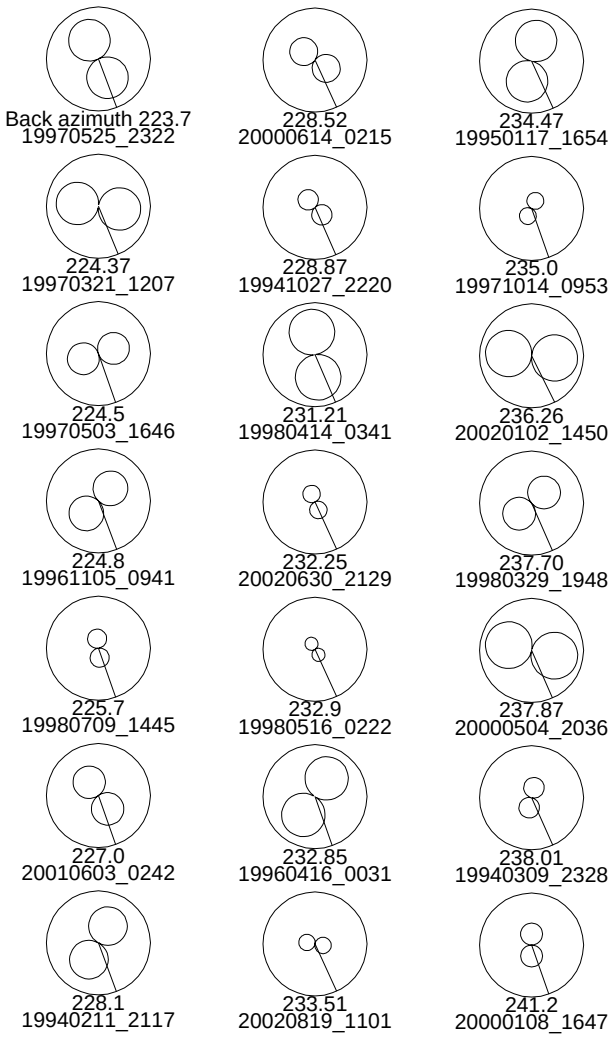

Figure 3.4: SH wave radiation pattern of the Fiji-Tonga events recorded at station BDFB. The radiation patterns are evaluated in the great circle plane, which connects the source and receiver. The straight line in each plot shows the take-off angles of Sdiff phase. The mechanisms are from the Harvard CMT Catalog (http://www.seismology.harvard.edu/CMTsearch.html). They are shown in order of back azimuth from BDFB from the top left to bottom right.

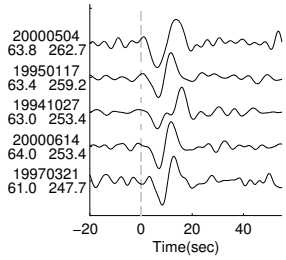

Figure 3.5: S waveforms for those events listed in Table 3.1, recorded at station RPN (shown in Fig. 3.1), for which data are available. The event date, epicentral distance(left) and azimuth(right) are indicated on the left of the traces. The simple S phase waveforms indicate that the secondary pulses in the SHdiff waveforms in Figure 3.3 are due to heterogeneous structure rather than to the source process. Event 19941027 has a secondary pulse around 10 sec after the first motion, but this cannot be related to that observed for SHdiff, as the latter arrives much later, about 25 sec after the first motion.

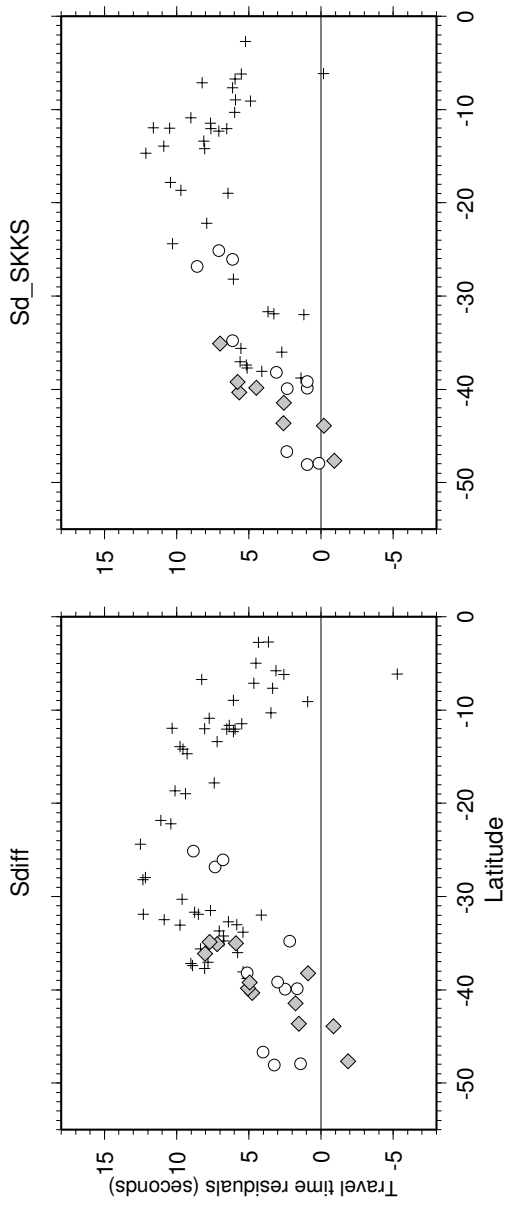

Figure 3.6: Travel time shifts as a function of latitude of the point where the Sdiff raypath reaches the CMB. Left: absolute Sdiff travel time residual with respect to PREM. Right: differential travel time residuals of Sdiff-SKKS. Diamonds correspond to the data at station BDFB. Crosses are data for Fiji-Tonga events. Circles are data for South American events. Both Sdiff and Sdiff-SKKS shows a steep gradient with respect to latitude.

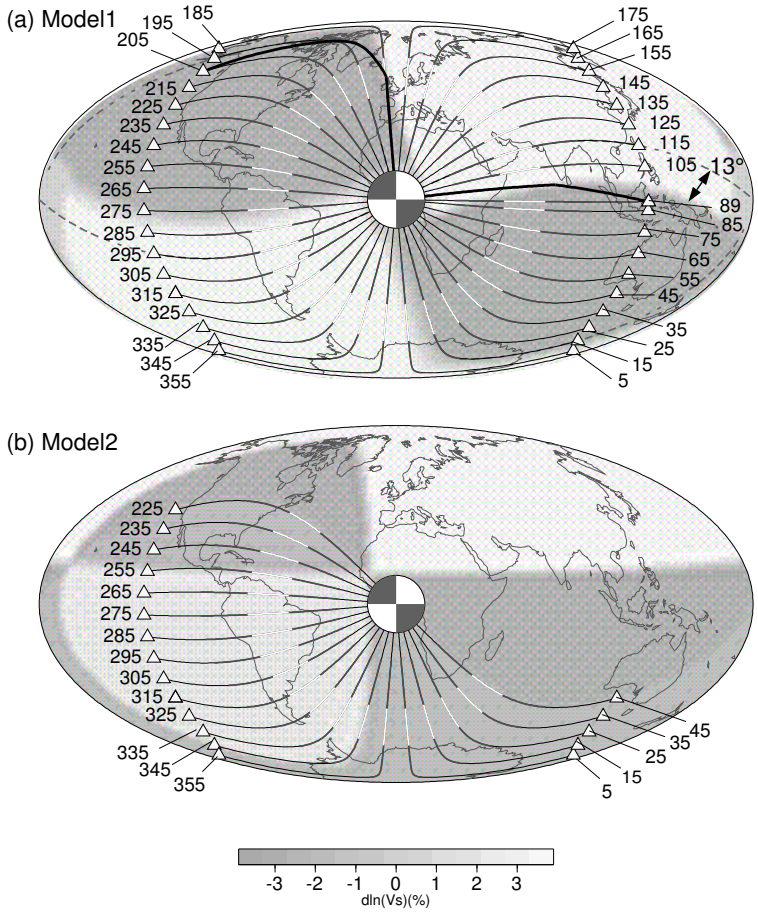

Figure 3.7: The shear velocity models used in the CSEM synthetic waveform calculation. (a) Model1: The fast and slow regions have velocity anomalies of -3% and +3% respectively with respect to PREM. The sharp boundaries are located in the top and right (North trending and East trending, thin white lines), and gradual boundaries are on the left and bottom. The sharp boundaries are shifted 13 degrees away from the great circles, which are parallel to them (shown by a dashed line). The gradual boundaries are oriented between 5 degrees and 13 degrees from the great circles. (b) Model2: The fast and slow regions have velocity anomalies of -2% and +2% respectively. The boundaries are shifted 15 degrees away from the great circles which are parallel to the interface. Thick dark lines show the portion of Sdiff raypath, which samples the bottom 300km of the mantle. Thick white lines show the diffracting portion at the CMB. The numbers next to the stations are azimuths measured from the south. They also serve as the station names in Figure 3.5. Raypaths of 1D model are shown except for the station 89 and 205 in Model1 where multipathing are shown by thick black lines.

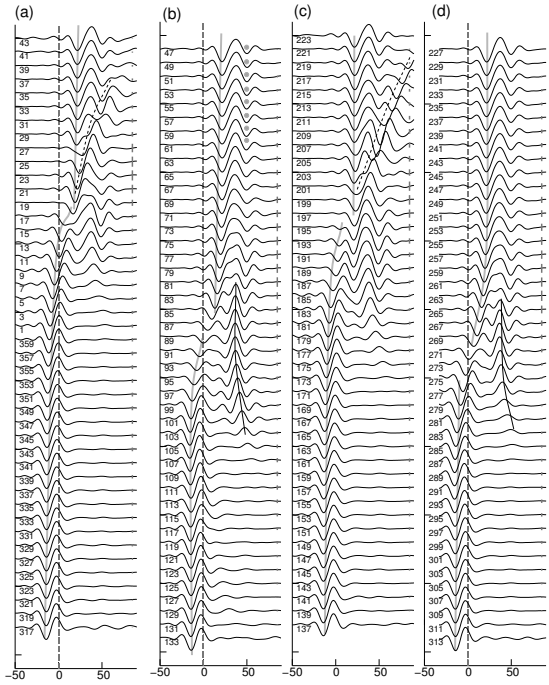

Figure 3.8: Synthetic waveforms calculated using CSEM for the models shown in Figure 3.7. Each trace is normalized by its maximum amplitude. Bars on the right side show the relative maximum amplitude. The waveforms in the four panels (a) to (d) are calculated for Model1 which has a 6% lateral shear velocity jump (-3% to +3%). They show different combinations according to whether the interface is sharp (c)(d) or gradual (a)(b) and whether the source is located on the slow (a)(c) or fast (b)(d) side of the interface. The waveforms in the last two panels (e) and (f) are calculated for Model2, which has a lateral velocity jump of 4%. The source is located in the slow region for (e), and in the fast region for (f). The gray lines follow the trough of the first pulse. When the source is located in the slow anomaly region ((a), (c) and (e)), large postcursors (dashed lines) are observed at the receivers located in the slow regions. They correspond to paths turning within the velocity gradient. They are observed at stations 24-41 for (a), 221-203 for (c) and 1-7 for (e). When the source is located in the fast region ((b), (d) and (f)), a secondary phase due to refraction and diffraction is observed as indicated by the black solid lines. They are observed at stations 81-105 for (b), 261-281 for (d) and 231-259 for (f). The waveforms which sample only the slow regions (stations at 47-63, 227-241 for Model 1, 13-41 for Model 2) show additional pulse which are indicated by grey dots. We think the pulses are due to the vertical velocity change in the synthetic model, which is the sudden reduction of velocity at 300km above the CMB.

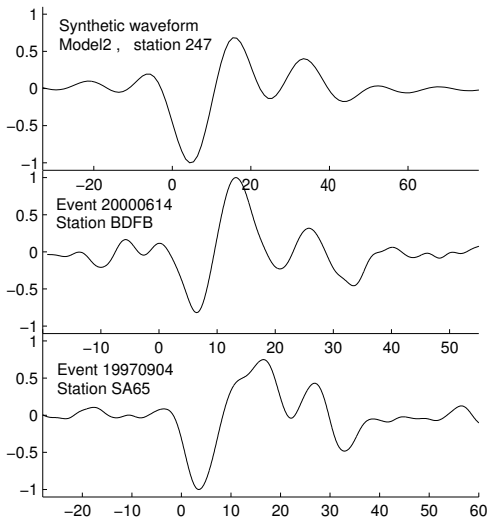

Figure 3.9: Comparison between observed and synthetic waveforms. Top: CSEM synthetics as in Figure 3.5. Middle: an observed waveform that samples PSA, bandpass filtered with corner frequencies at 0.01 and 0.125 Hz. Bottom: an observed waveform that samples ASA. In Figure 3.2(a) this trace is shown at a back azimuth of 212 degrees, but bandpass filtered with corner frequencies at 0.01 and 0.10 Hz. The time scale of the synthetic is streched compared to that of the observed waveforms. This is because among the synthetic waveforms, we have chosen a station which clearly shows the two crests separately. Stations that are closer to the boundary would present the two pulses closer to each other, however with the frequency limitation those pulses would blend into a single broadened pulse.

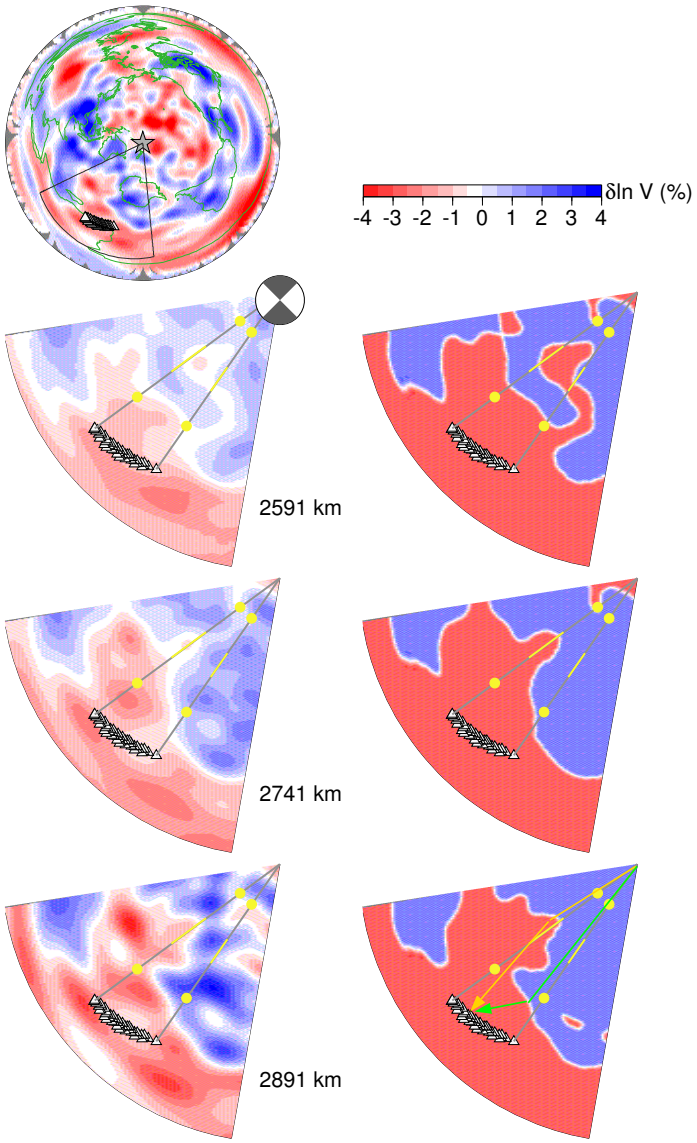

Figure 3.10: Left panel: the original SAW24B16 model at three depths in the bottom 300km of the mantle. The source in Fiji Tonga region is located at the apex. The stations in Africa (Fig. 3.1) are shown by triangles. Right panel: a model which is modified from SAW24B16. The boundary of the fast and slow anomaly is the contour line of 0(%) anomaly of SAW24B16. The anomaly jump is from -2.75 to 1.75 (%) . Theses values are determined by fitting travel time data. The model is expanded in spherical harmonics of up to degree 300, and the velocity jump of 4.5(%) occurs within a distance of 100km at the CMB. Both models have 1D PREM structure from surface down to 370km above the CMB. The 3D velocity anomalies linearly increase from 370 to 300 km above the CMB.

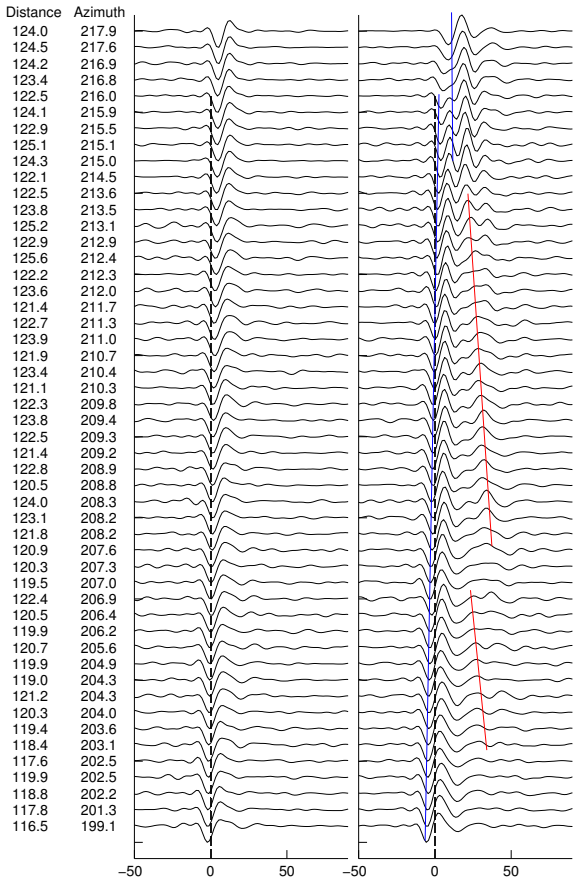

Figure 3.11: Synthetic waveforms calculated by CSEM down to 8 seconds. (a) The waveforms from the original tomographic model (Fig. 3.10 left panel); (b) the waveforms from the modified model (Fig. 3.10 right panel). Gray lines follow the first trough, black lines follow the secondary arrivals.

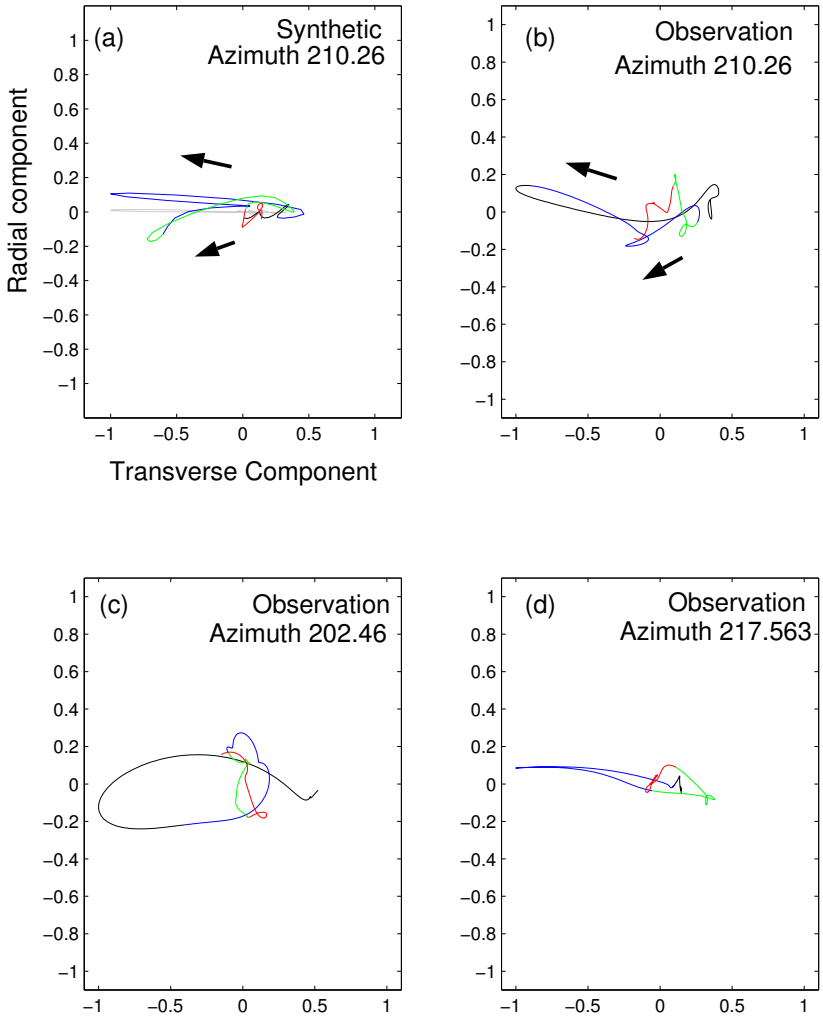

Figure 3.12: Comparison between synthetic (a) and observed (b) particle motions at one of the stations of African array. The station is located at an azimuth of 210.26 degrees and a distance of 121.09 degrees. The color indicates the time with respect to predicted Sdiff arrival from PREM. Black: -35 to -5 s, Blue:-5 to 20 s, Green 20 to 45 s, Red 45 to 70 s. Gray line shows the particle motion calculated from PREM. Arrows indicate the motion of first and second pulse. (c) and (d) are also observed particle motions at the stations located at an azimuth of 202.46 and 217.563 respectively.

Chapter 4

Toward estimations of the Vs anomaly gradient around the Pacific superplume

Summary

In the previous chapter, we showed that the tomographic model (SAW24B16, [*Mégnin and Romanowicz*, 2000]) underestimates the amplitude and gradient of the S velocity (referred to as Vs hereafter) anomalies in the D” layer beneath the Indian Ocean. In this chapter, we examine how well the anomalies are resolved in other regions of the D” layer. We put special focus on the anomaly distributions in the Pacific region, where the locations and details of sharp anomaly gradients around the Pacific superplume are less well understood

than in the African superplume (Fig. 1.2).

First, we evaluate the method which was used to construct the S velocity tomographic model. NACT (nonlinear asymptotic theory, [*Li and Romanowicz*, 1995]) is the method which was used both in the forward and inverse problems in the process of making the tomographic model. We compare the travel time predictions from the two methods, CSEM(Coupled mode Spectral Element Method, [*Capdeville et al.*, 2003]) and NACT. The comparison shows limitations in the ability of NACT to handle effects of large amplitude Vs anomalies.

Second, by comparing synthetic and observed travel times of the Sdiff phase, we evaluate the amplitudes and gradients of the anomalies given by the tomographic model. Despite the limitations in the method which was used to make the model, the comparison shows that the model predicts observed travel times very well, even for those traces with large travel time anomalies.

Finally, we try to estimate the amplitudes and gradients of the Vs anomaly in regions where the tomographic model is unsuccessful in predicting the travel time anomalies. We also examine how sensitive the travel times are to the amplitude and gradient of the Vs anomalies.

4.1 Comparisons of travel time predictions from different methods

First, we assess the method which was used in making the S velocity global tomographic model (SAW24B16) by comparing travel time predictions from NACT and CSEM. As a reference, and also to understand Vs anomaly distribution of the model, we also calculate travel time predictions from 1D ray theory.

1D ray theory is an expedient way to estimate travel time anomalies. The method relies on a high frequency approximation, and assumes that the wave is only sensitive to the heterogeneity along the ray. It also assumes that the anomalies are small in amplitude so that the ray is not bent due to 3D heterogeneities. The predicted travel time anomalies from this method are the summation of the anomalies along the 1D ray.

Ray tracing is conducted in a spherically symmetric (1D) reference model (PREM, [*Dziewonski and Anderson*, 1981]). We first divide the mantle into layers of thin (5km) shells, and then calculate the length of the ray within each layer. Finally, the travel time anomaly in each segment, due to the velocity deviation from the 1D model, are integrated over the ray.

The travel time anomaly in ith segment, dt_i, is given by the following equation:

$$dt_i = -T_i \frac{dv_i}{v_i} \tag{4.1}$$

where

$$T_i = \frac{(dr_i{}^2 + (r_i, d\theta_i)^2)^{\frac{1}{2}}}{v_i} \tag{4.2}$$

T_i is the travel time in the ith layer, dr_i is the thickness of the ith layer, r_i is the radius of ith layer, v_i is the S wave velocity in the ith layer in the 1D model, dv_i is the velocity anomaly in ith layer and $d\theta_i$ is the distance of the ray along the great circle within the ith layer.

$d\theta_i$ can be obtained by first defining the ray parameter p as

$$p = \frac{r \sin j}{v} \tag{4.3}$$

where j is the incident angle of the ray at a radius r. The ray parameter is constant along the ray. Equation 4.3 can then be rewritten to

$$r d\theta = dr \tan j = dr \frac{pv/r}{\sqrt{1-(pv/r)^2}} \tag{4.4}$$

$$d\theta = \frac{pdr}{r\sqrt{(r/v)^2 - p^2}} \tag{4.5}$$

By integrating equation 4.5 from r_i to r_{i+1} we get

$$d\theta_i = w\left(\cos^{-1}\left(\frac{pv_i}{r_i}\right) - \cos^{-1}\left(\frac{pv_{i+1}}{r_{i+1}}\right)\right) \tag{4.6}$$

where w is

$$w = \frac{1}{1 - \frac{\log\frac{v_i}{v_{i+1}}}{\log\frac{r_i}{r_{i+1}}}} \tag{4.7}$$

with the assumption that the 1D velocity profile with respect to the radius can be expressed by the function

$$v(r) = ar^b \tag{4.8}$$

NACT is a normal mode based method and provides waveforms that take into account the heterogeneities on the great circle plane between the source and receiver. Because it includes not only along-the-mode-branch coupling of the modes, but also cross-branch coupling, the theory is able to bring out the ray character of body waves using normal-mode superposition, and accounts for 2D sensitivity in the vertical plane [*Li and Romanowicz,* 1995; *Li and Romanowicz,* 1996; *Mégnin and Romanowicz,* 2000; *Gung et al.*, 2004; *Panning and Romanowicz,* 2006]. The method handles a finite frequency effect. In other words, heterogeneities not only on the ray but also in a region around the ray, where the waves are sensitive due to the finite wavelength, are taken into account.

The Coupled mode Spectral Element Method (CSEM) [*Capdeville et al.,* 2003] is a nu-

merical method to solve the wave equation in 3D heterogeneous media, and it provides complete waveforms. It is exact and not based on any of the approximations, which are mentioned above. This method is described in Chapter 2. The waveforms are calculated down to 17 seconds.

The model has a 3D structure in the bottom 370km of the mantle, given by the S velocity tomographic model SAW24B16. SAW24B16[*Mégnin and Romanowicz*, 2000] is derived from the inversion of hand picked body, surface and higher-mode waveforms, including SHdiff, by using NACT both in the forward and inverse problem. In order to measure the travel time anomalies from NACT and CSEM synthetic waveforms, synthetic waveforms from the 1D model (PREM) are first created for each trace. The travel time anomalies are obtained by taking the cross correlations between PREM and the 3D synthetics. 800 Sdiff waveforms from 15 events are used for the comparison. The locations of events and stations are presented in the next subsection, where we show the measurements from the observed waveforms.

Figure 4.1(a) shows the comparison of travel time anomalies predicted by CSEM and NACT. The travel time anomalies predicted by NACT are clipped around -6 seconds on the negative side and around 4 seconds on the positive side of the travel time anomalies. The figure shows the limitations of NACT in handling strong heterogeneities. In NACT, the effect due to lateral heterogeneities is partitioned in two parts. The first part takes into account the horizontally averaged structure along the great circle between the source and

station. This term can handle the non-linear effects caused by heterogeneities. In the second term, the rest of effects due to cross-branch modal coupling are calculated. This term is linearized and then treated asymptotically under the assumption that these effects are small. The 4.1(a) shows that this assumption is not valid for traces which sample strong heterogeneities. It should be noted that the tomographic model provides smaller amplitude of anomalies compared to the real earth, as it was shown in the previous section. The effect due to the linearized term can be larger when the method is applied to observed data.

Figure 4.1(b) shows the comparison of travel time anomalies predicted by CSEM and 1D ray theory. The travel times of 1D ray theory represent the structure along the 1D ray path. The CSEM gives smaller travel time anomalies for positive travel time anomalies.

In Figure 4.1(b) we used the Vs anomalies at the depth of 2850km as the anomalies at the Core Mantle Boundary (referred to as CMB hereafter) for the 1D ray tracing. Figure 4.2 shows more plots of travel time anomalies from 1D ray theory with respect to CSEM. Vs anomalies at different depths are used for 1D ray tracing in each figure. In the Figure4.2(a), the anomaly model at 2800km is used as the CMB anomaly for the ray tracing. In the Figure 4.2(c) , the actual CMB anomaly is used at CMB. There are two features in the figures, which should be noted. The first is the good correlation of travel time predictions between CSEM and the ray tracing which is shown in Figure 4.2(a). This feature indicates that Sdiff phases are sensitive to structures at the depth around 2800km, which is 90km above CMB, rather then the structure at the CMB. The second feature to note is that, for

the positive travel time anomalies, the differences in travel time predictions from the two methods become larger as the ray sample anomalies that are located deeper in the mantle. A comparison between (a) and (c) of the Figure 4.2 indicates that SAW24B16 has a stronger anomaly gradient with respect to depth in slow regions than in fast regions.

The two features shown in Figure 4.2 indicate that the deviation of the plots from the y=x line in Figure 4.1(b) is likely to be due to the finite frequency effect. The effect is included in CSEM but not in ray theory. Because of the finite width of wavelengths, waves sample not only the heterogeneities on the ray but also those in regions around the ray. The effect of heterogeneities is averaged over a finite depth. Since the model has a strong positive vertical gradient of anomaly amplitudes in the slow velocity regions in D", but not in the fast regions, the predictions between the two methods are different only for the positive travel time anomalies.

Figure 4.1(c) shows the comparison of travel time anomaly predictions between 1D ray theory and NACT. This plot also shows the two features described above. Compared to Figure 4.1(b), NACT gives smaller amplitudes of negative travel time anomalies, which shows the limitations of applying a linearized theory to the model. The plot shows the deviation from the y=x line, which is due to the finite frequency effect that is included in NACT but not in ray theory.

4.2 Evaluating the S velocity tomographic model

4.2.1 Comparison of observed and synthetic travel time anomalies

We compare synthetic and observed travel times and evaluate how well the amplitudes of the anomalies are resolved in the tomographic model SAW24B16. The synthetic travel times are calculated by using CSEM for the bottom 370km of the mantle and by using 1D ray theory to correct for the 3D heterogeneities within the rest of the mantle. The ellipticity correction (ftp://rses.anu.edu.au/pub/ak135/ellip) is included. Station elevation corrections are not included.

Figures 4.6 4.7 and 4.8 show the comparison of the travel time anomalies. The location of the paths are shown in Figure 4.3, 4.4 and 4.5. We chose events with depths greater than 300km to avoid contamination from the depth phases and from strong upper mantle heterogeneity.

The result of the comparison shows that the model predicts the observed travel times very well for most of the data. In many traces there are only a few seconds or less difference between the synthetic and observed travel times. There are some cases in which the synthetics give a much smaller amplitude of travel time anomalies compared to data. These data are marked by blue arrows and can be categorized in the following three cases:

(1) Traces with large travel time anomalies. Most of the data which are marked by blue

arrows have an observed travel time anomaly greater than approximately 7 seconds.

(2) Traces which sample the regions where the dataset for SAW24B16 does not have good coverage in the D" layer. This is the case for the data which sample the southern hemisphere and Atlantic Ocean region. This suggests that the first step to resolve the amplitude of Vs anomalies is to use a dataset with good sampling coverage. In Figure 4.6 4.7 and 4.8, the backgrounds of the graphs are pink for the data which sample the southern hemisphere.

(3) Traces which seem to be affected by local anomalies. Example data includes event (c) 102/57 (distance/azimuth), event (h) 101/298 and event (l) 101/56. The corresponding stations are surrounded by many other stations nearby and the anomalies are not observed in other stations. The discrepancies can also be due to noise or inaccuracy in the travel time measurements.

4.2.2 Travel time analysis of Sdiff, SKKS and SKS phases

We evaluate the distribution and amplitude of the anomalies given by the tomographic model for the D" layer around the Pacific region. We collected 3861 Sdiff travel times which sample the Pacific region. They are measured in the same way as described in the section 4.1. Additionally, we measured travel times of SKS and SKKS for the same traces when those phases were clearly observed. We collected 1796 SKS and 1729 SKKS travel times. Figure 4.9 shows the measured Sdiff travel time anomaly with respect to PREM.

Travel time anomalies are plotted at the midpoint of the diffracting portion of the Sdiff phase. The anomaly distribution has a good correlation with the tomographic model in the D" layer. The figure indicates that the S wave structure in the D" layer primarily contributes to the observed Sdiff anomalies.

Figure 4.10 through 4.16 show the Sdiff travel time anomalies with respect to azimuth or back azimuth for some selected events or stations. The synthetic travel times are also plotted. Because travel times are measured from 248 events and it is expensive to run CSEM for such large numbers of events, the synthetics are obtained from 1D ray theory. The anomaly model at the depth of 2850km is used as the anomaly model at CMB. Travel times of SKS and SKKS are also plotted. Lack of correlations of the travel time anomalies between Sdiff and other phases indicates that the Sdiff travel time anomalies are due to heterogeneities within the lower mantle. This is because the paths of Sdiff and SKKS are close to each other in the upper mantle but they are different in the lowermost mantle. The paths of SKS and Sdiff are more separated compared to Sdiff and SKKS in the upper mantle, however the lack of correlation between SKS and Sdiff travel time anomalies can still indicate if the Sdiff anomalies are caused by near source or station structure or the lower mantle structure.

Figure 4.10 and 4.11 show that trends of Sdiff travel time anomalies are well predicted in the Western and Northern Pacific. The paths sample the border of the Pacific superplume. The finite frequency correction, which is indicated by the dashed line in Figure 4.1, is not

applied in the synthetic travel times. With the finite frequency corrections, the positive anomalies of synthetic travel times become a few seconds smaller from what is shown in the figures. Figure 4.12 and 4.13 show the data set with steep change in Sdiff travel time anomalies with respect to azimuth, observed in the central Pacific. The paths sample inside the Pacific superplume and the jumps of the Sdiff travel time anomaly are associated with small changes of anomalies within the superplume. They indicate a possibility that the superplume is a gathering of multiple separated slow regions rather than a single big blob. Figure 4.14 and 4.13 show some cases where the model over predicts the travel time anomalies. Figure 4.15 and Figure 4.16 show cases where the model underestimates the travel time anomalies.

4.3 Towards the estimation of the Vs anomaly gradient at the base of the mantle

In this section, we modify the gradients of the Vs anomalies in D" layer given by tomographic models and compare the travel time anomalies predicted from the models with the data. From this modeling we estimate the range of gradients of the Vs anomalies which can be explained by the data.

The Vs anomalies between the depths of 2891 and 2521 km are modified by applying a

function to the original Vs anomalies. One example of such a function is shown in Figure 4.17. Each function is determined by a combination of 4 parameters. *x*0 is the shift of the origin, or the point of symmetry, in the x axis. *y*0 is the shift of the origin in the y axis. xd and yd are the distance in the x and y axes from the point (x0, y0) to the point where the slope of the function becomes 0. There is another way to define the same function. In some cases the slope at x0 is given as one of the parameters instead of yd. We fit second order polynomials to these four values. These functions have the following two properties: (1)they change the gradient of the original Vs anomalies for anomalies which fall between x0-xd and x0+xd in the original model, and (2) they flatten the Vs anomaly for those which are larger than x0+xd or smaller than x0-xd in the original model. We show the results of the modeling for two different regions, the Central and Southern Pacific.

4.3.1 Central Pacific

From the Sdiff travel time data set, we chose the data that have their midpoint in the region between latitude -25 and 11 degrees and longitude -180 and -147 degrees. This is the region where the decrease of Sdiff travel times with respect to latitude was shown in the previous chapter (Fig. 3.6). The distribution of the paths is shown in Figure 4.18. We searched for the combination of four parameters, which best fits the travel time data, through the parameter set of:

x0=(-1, -0.75, -0.5, -0.25, 0, 0.25, 0.5),

y0=(-2, -1.5 -1, -0.5, 0)

xd=(0.5, 1, 2, 3)

yd=(1.5, 2, 2.5, 3) We tested 3 different models, SAW24B16, SB4L18 [*Masters et al.*, 2000,] and S20RTS [*Ritsema and van Heijst* , 1998]. The results are shown in Figure 4.18 to 4.21 and also in table 4.1. The variance of travel times before and after the modeling and the four parameter set of the best fitting modified model for each original model are shown in Table 4.1.

The slope of the function at (x0, y0) is indicated as “gradient” in the table. Synthetic travel times are calculated by ray tracing. Except for the model SAW24B16*, the anomaly at the CMB is used as it is, without any finite frequency corrections. The finite frequency correction, which is shown by the dashed line in Figure 4.1, is applied to the predicted travel times for SAW24B16*. We calculated the residual variance from differential travel times, such as Sdiff - SKKS and Sdiff - SKS. The variance is calculated as follows.

$$var = \frac{\sum((O_{Sd-SK} - S_{Sd-SK})^2 + (O_{Sd-SKK} - S_{Sd-SKK})^2 + (O_{SKK-SK} - S_{SKK-SK})^2)}{N_{Sd-SK} + N_{Sd-SKK} + N_{SKK-SK}}$$

O and S stand for observed and synthetic travel time anomalies respectively. The subscripts $_{Sd-SK}$ $_{Sd-SKK}$ and $_{SKK-SK}$ stand for Sdiff-SKS, Sdiff-SKKS and SKKS-SKS differential travel times respectively. N is the number of differential travel time measurements. A smaller variance indicates a better fit of synthetic travel times to the data.

Figures 4.18 through 4.21 show the Vs anomaly distribution at the CMB (depth of 2891km) of the original and modified models and the comparisons of observed and predicted travel times. The difference between Figure 4.18 and 4.19 is that in 4.19, the finite frequency correction is applied to the synthetics travel time from ray theory, whereas no correction is applied in 4.18. Among the three models, the variance is smallest for SAW24B16 both before and after the forward modeling. The bottom panels of 4.19 show that the original SAW24B16 model (blue triangles) already predicts well the trend of the observed travel time anomalies (pink circles). After the modeling by the parameter search, the fit to the data became better for the data between latitude -18 and -10 degrees. The maximum and minimum anomaly amplitudes of the original SAW24B16 model are -5.8 and 5.7% at the CMB. After modeling, the model is saturated with anomalies of -2.5 to 2.5%. The results show that the trend of travel time data can be explained well by increasing the gradient and saturating the model with constant anomaly values.

The plots of the travel time anomalies for model SB4L18 (Figure 4.20) show that mostly only the average value of the anomalies have changed after the modeling. The trend of the travel time anomalies is already explained by the original model. The anomaly range of the

original model is -2.4 to 1.53% at the CMB. The model is saturated at -2 and +2% in the modified model. A significant improvement of travel time anomaly predictions is shown for S20RTS(Figure 4.21). The anomaly range of the original model is -2.4 to 2.1 % at the CMB. The model is saturated at -3 and 2%.

The range of the anomalies obtained for all the models, except SAW24B16*, are between 4 and 5%. This is consistent with the result we presented in the previous chapter, where the difference between the slow and fast regions was 4.5 %. The result also shows that the models provide a good fit to the travel times with larger gradients of anomalies than the original model.

It should be noted that we ended up having many models with similar variance reductions but with different parameter combinations, although most of the models which have a good fit to the data have a larger gradient than the original model. Table 4.2 shows parameters and variances of the 3 models based on SAW24B16 that best fit the data. It shows there is a range of models that can fit the data. From the data set we have, it is difficult to single out the best model by only using 1D ray theory. It should be possible to extract more information on the structure in the D” using full waveform and not just travel times.

We chose one event from among the events which are shown in Figure 4.18 and calculated CSEM synthetics from SAW24B16 and 3 different modified models based on SAW24B16. Figure 4.24 shows the location of the event and the raypaths, together with the observed travel time anomalies for the Sdiff, SKS and SKKS phases.

We used four data points (see figure) between the azimuths of 70° and 105° as the data for the modeling.

The three modified models are the models which are obtained by the parameter search using ray theory, as described above. We calculated the variance reduction in the two datasets, one from all the data shown in Figure 4.18 with 325 paths, and the other the data of four points shown in Figure 4.24. Then we searched for a model which shows good variance reduction in both data sets. The travel times are predicted from 1D ray theory. The four parameters which describe how the models are created from SAW24B16 are indicated in the caption of Figure 4.25 for each model.

The anomaly distributions of each model are shown in Figure 4.25. Model399 fits the data better than SAW24B16 when the finite frequency correction (Fig. 4.1(b) dashed line) is not applied to the synthetic travel times from ray theory. Model8 fits the data better than SAW24B16 when the finite frequency correction is applied to the synthetic travel times obtained from ray theory. Model40 has the same parameters as Model8 except for the parameter $y1$. It has the same gradient and shape of the boundaries between the slow and fast regions as Model8, but the average value of the anomalies is 1% faster than Model8. The top panel of Figure 4.26 shows the comparison of observed Sdiff travel time anomalies with synthetic travel time anomalies for the four models obtained by ray theory **without** the finite frequency correction. Model399 and SAW24B16 give good fits to the data. The middle panel of Figure 4.26 shows the comparison of observed Sdiff travel time anoma-

lies with synthetic travel time anomalies obtained by ray theory **with** the finite frequency correction. Model8 gives the best fit to the data. The bottom panel of Figure 4.26 shows the travel time anomalies obtained by CSEM synthetics. Among the four models, Model8 gives the best fit to the data, although the fit is not perfect. It indicates that with the parameter search method using ray theory with finite frequency corrections, we are able to get a model which fits the data better than the original model. However, more work is required to obtain better fits and more accurate estimates of the amplitudes of the anomaly. For Model8 and Model40, travel time anomalies obtained by CSEM are significantly lower than those from ray theory.

In Figure 4.25, Model40 and Model8 show strong gradients for the slow velocity anomalies at a depth of around 2800km. In other words, the strong slow anomaly at 2800km mostly disappears at a depth of 2700km. On the other hand, the slow anomalies are more continuous in Model399 and SAW24B16 and the differences in the travel time predictions between CSEM and raytheory are smaller. The vertical gradient of the anomalies in the D" layer is the reason for the discrepancies in the travel time anomaly predictions between ray theory and CSEM. The main result of this experiment is that resolving this gradient might hold a key to a better understanding of S velocity structure in the D" region.

4.3.2 Southern Pacific

We show an example where the parameter search is unsuccessful. The tomographic model SAW24B16 underestimates the travel time anomaly for a few parts in the Southern Pacific. We applied the forward modeling using a parameter search to the data which sample the Southern Pacific. The paths of the data set are shown in Figure 4.22. We tested combinations of the following parameter set.

x0=(-0.25, 0, 0.25, 0.5)

y0=(-0.5, -0.25, 0, 0.25)

xd=(1, 1.5, 2, 2.5, 5)

slp0=(0.7, 1, 1.43, 2.14)

The variance of this experiment is defined by:

$$var = \frac{\sum((O_{Sd} - S_{Sd})^2)}{N_{Sd}}$$

O_{Sd} and S_{Sd} stand for observed and synthetic Sdiff travel time anomalies respectively. The variance is 0.530 for the original SAW24B16. After forward modelling, the variance becomes 0.287 for the best fit model with (x0, y0, xd, slp0)= (0.25, -0.5, 5, 1). Figure 4.23

shows the comparison of predicted travel time anomalies from the two models. The observed anomalies are also plotted. The fit of the predicted anomalies to the data becomes better after the forward modeling. However, only the average value of the anomalies is shifted. In other words, several seconds are added to the original anomalies for all the traces, the new model does not produce steep shift of the anomalies with respect to back azimuth which is observed in the data.

The result shows that it is important to have a good starting model to conduct the parameter search. The result is consistent with the low coverage of D" sensitive data in this region in the dataset, which was used to create SAW24B16. The first step to obtain the gradients and amplitudes of anomalies is to create a tomographic model from a dataset with a good sampling coverage.

4.4 Conclusions

We evaluated the NACT waveform modeling method, which was used to construct an S velocity tomographic model. The comparison of Sdiff phase travel time anomalies predicted by CSEM and NACT shows limitations in the ability of NACT to handle the effects of large amplitude Vs anomalies. The travel time anomalies of NACT are clipped around -6 seconds on the negative side and around 4 seconds on the positive side, whereas CSEM gives the travel time anomalies in the range between -10 and 6 seconds. The comparison

of travel time anomalies predicted by 1D ray theory, CSEM and NACT shows the importance of including finite frequency effects in the modelings. With 1D ray theory, which does not include the finite frequency effect, the model SAW24B16 tends to give larger positive travel time anomalies than the two other methods. The differences of the predicted anomalies between CSEM and 1D ray theory became as large as 5 seconds.

We evaluated the D" layer structure of the S velocity global tomographic model by comparing the observed and predicted travel times of Sdiff phase. Despite the limitations in the NACT method which was used to make the model, the model gives good predictions of travel time anomaly amplitudes particularly in the regions where the dataset for SAW24B16 has good sampling coverage. It suggests that the first step to get the correct Vs anomaly amplitudes is to use a dataset with good sampling coverage in the inversion. Travel times are under predicted for some of the traces with large amplitude travel time anomalies.

The travel time analysis of Sdiff and SKS,SKKS travel time dataset, which samples the Pacific region, shows the following features:

(1) Vs anomalies of the D" layer are well predicted in the model SAW24B16 particularly in Western and Northern Pacific:

(2) The Vs anomalies in the southern Pacific are under predicted in the model.

(3) The Vs anomalies are over predicted in the model for some traces which sample the Central Pacific.

(4) There are a few regions within the Pacific superplume where a steep change of Sdiff travel times with respect to azimuth are observed. The locations where the significant shifts are observed correspond to the regions where the model shows changes in Vs anomaly amplitudes.

Based on existing Vs global tomographic models, we created a range of modified models and searched for models which better explain the travel time anomaly data. The results of the parameter search show that we can find models that fit the travel time anomalies better by keeping the shape of anomaly and changing the amplitude and gradient. The difference of the Vs anomalies in slow and fast regions are between 4 to 5%. This is consistent with the value we obtained with forward waveforms modeling using CSEM in the previous section.

The result of the parameter search also shows that from the travel time data set we have, we can obtain a multiple number of models which almost equally explain the data. Using the waveforms, instead of travel time, as the data would help to distinguish between the models. Calculating CSEM synthetic waveforms for each of those models and comparing them with waveform data would allow us to evaluate which model explains the data better.

Table 4.1: Variance of the travel time residuals and the four model parameters

*Finite frequency correction which is provided in Figure 4.1 is applied to the synthetics

models	Original model	Modified model	x0	y0	xd	yd	gradient
SAW24B16	7.57 (sec^2)	6.58	-0.25	0	2	2.5	2.5
SAW24B16*	9.47	6.81	-0.25	0	1	3	6
SB4L18	9.76	7.08	0.25	0	2	2	2
S20RTS	13.83	7.34	0	-0.5	3	2.5	1.667

Table 4.2: Parameters of best fitting models, starting from SAW24B16

residual variance	x0	y0	xd	yd
6.58 (sec^2)	-0.25	0.	2.	2.5
6.59	0.	0.	2.	2
7.10	-0.25	0.	1.	2.

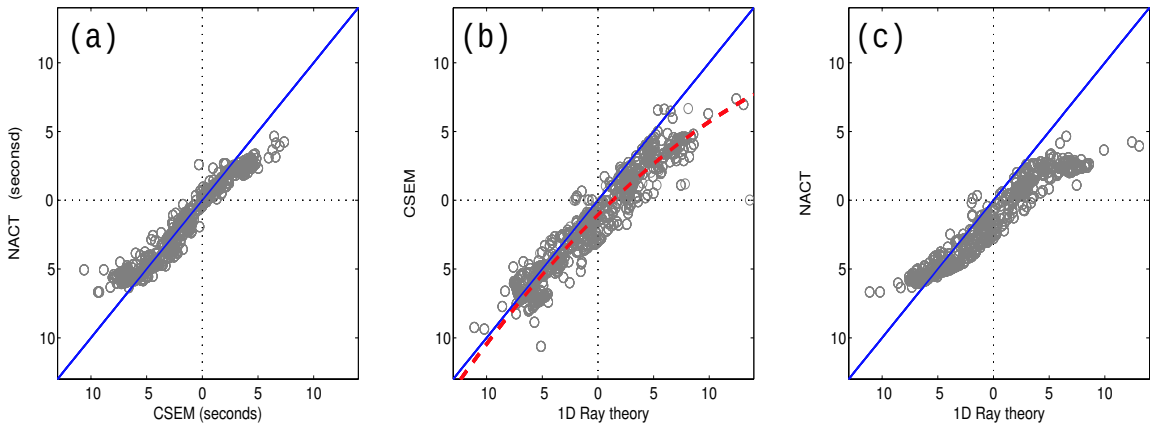

Figure 4.1: Comparison of travel time anomaly predictions of 3 different methods. The travel time anomalies are calculated for 800 Sdiff phases. The model has the 3D Vs structure of SAW24B16 for a 370km thick layer at the bottom of the mantle. (a) Comparison between CSEM and NACT (b) Comparison between 1D ray theory and CSEM. The dashed line is a 3rd order polynomial function which fits the data best in a least-squares sense (c) Comparison between 1D ray theory and NACT.

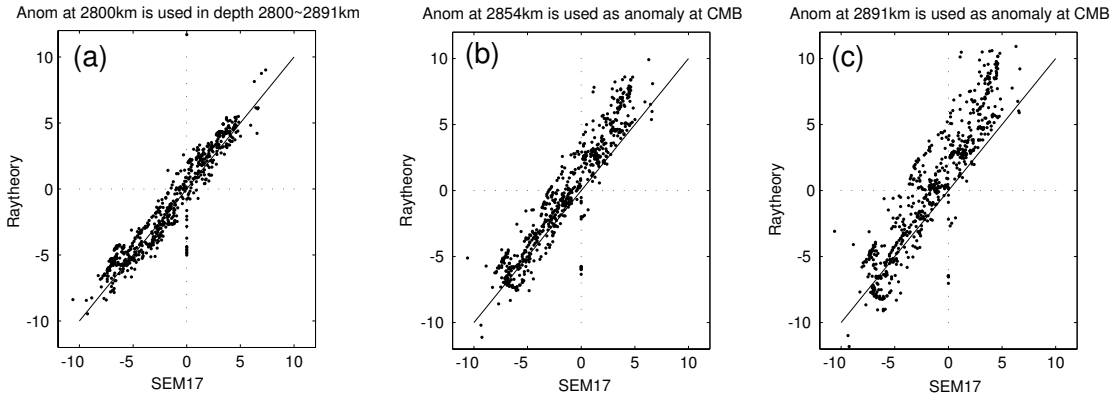

Figure 4.2: Comparison of travel time prediction between CSEM and raytheory. (a) The anomaly model at the depth of 2800km of SAW24B16 is used at the depth between 2800km and 2891km (b) The anomaly model at the depth of 2854km is used at the depth between 2850km and 2891km. (c) The original CMB structure of SAW24B16 model is used. The anomaly model at the depth of 2891km is used as it is at the depth of 2891km.

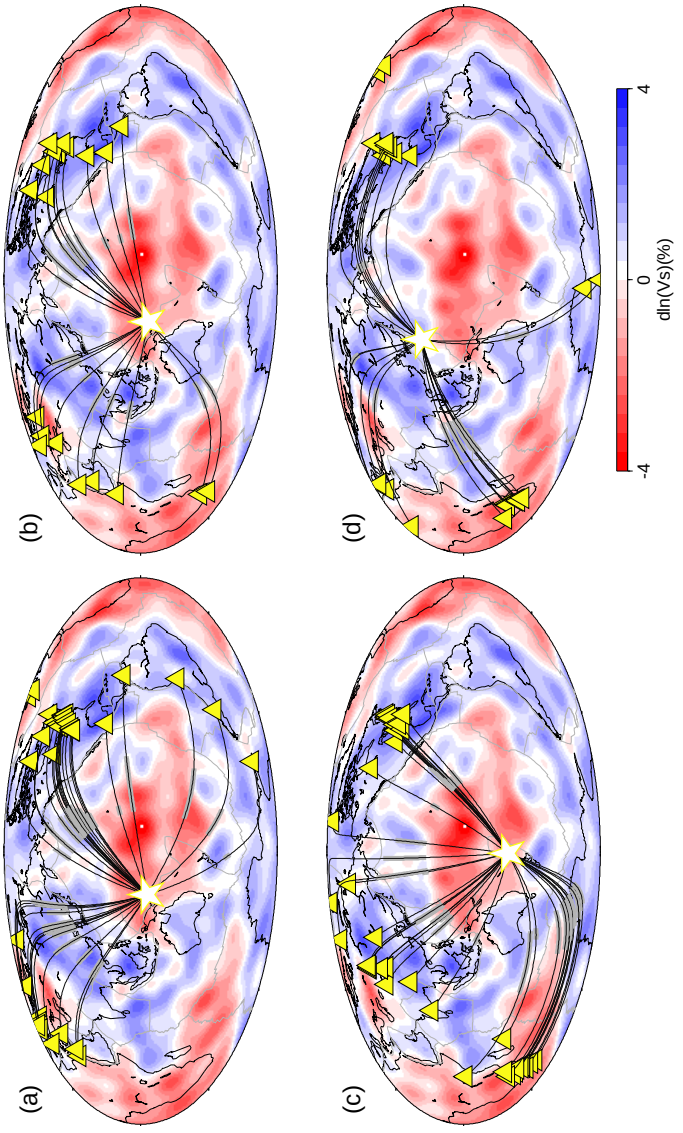

Figure 4.3: Location of the paths for which travel time measurements were made. Stars show the location of the source. Yellow triangles show the location of the stations. The diffracting portions at the CMB of the Sdiff phase are shown in thick gray lines. The background model is SAW24B16 at the depth of 2850km.

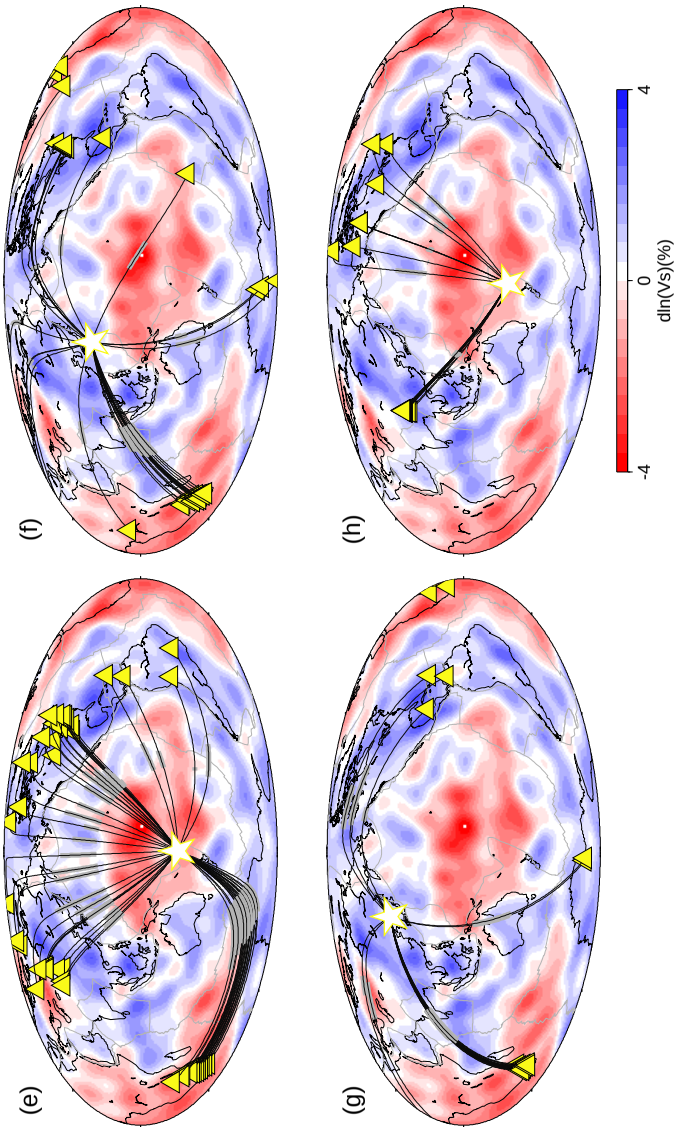

Figure 4.4: Continuation of Figure 4.3

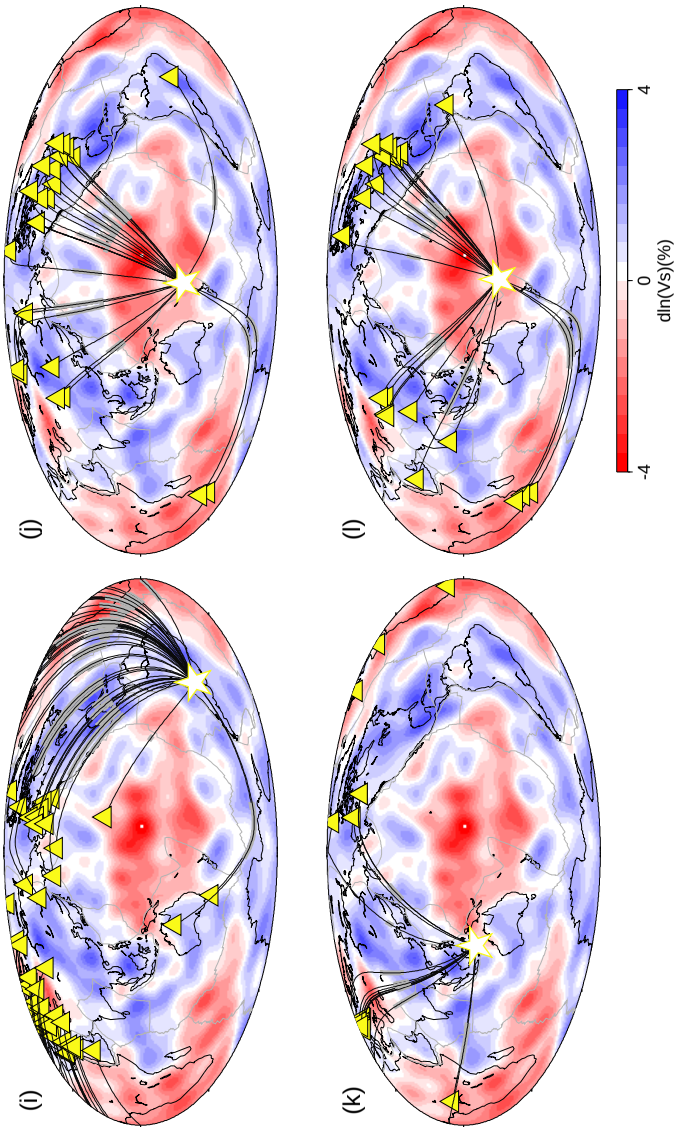

Figure 4.5: Continuation of Figure 4.3

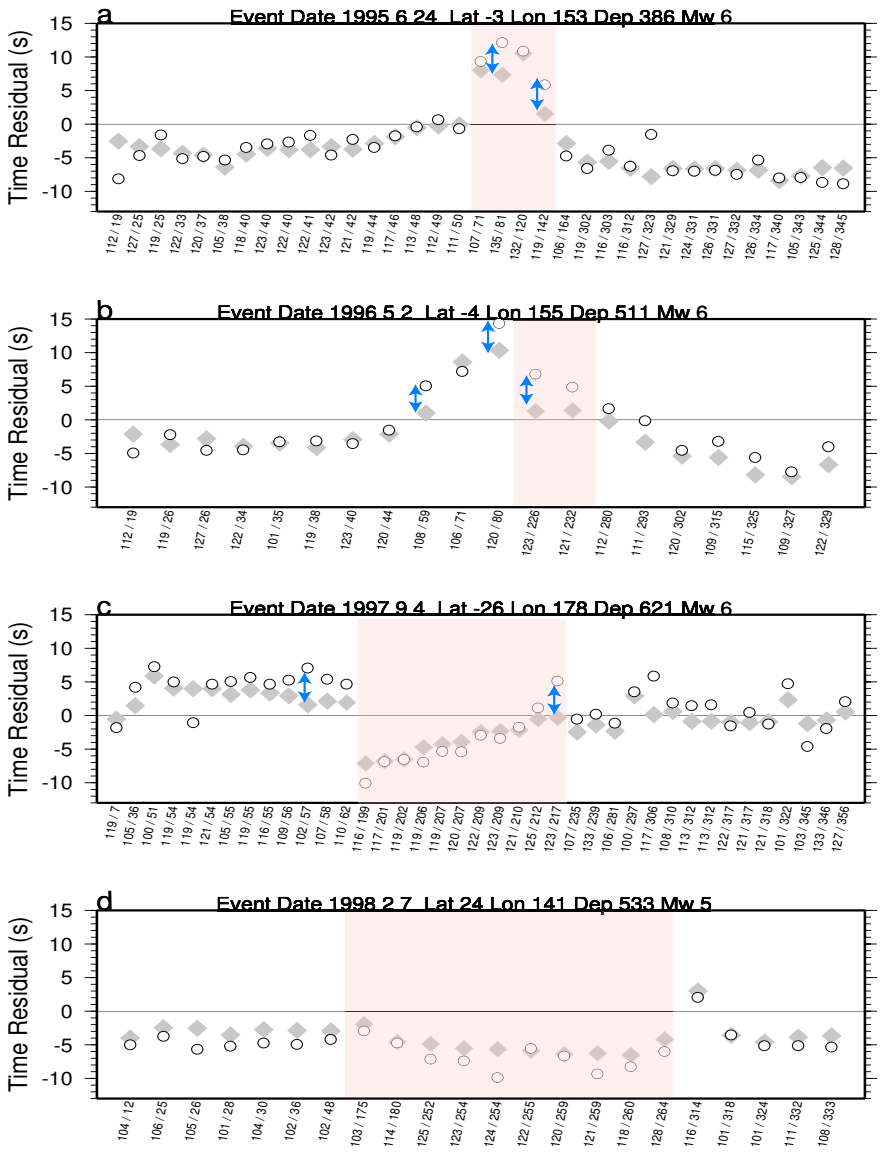

Figure 4.6: Open circles: Observed travel time anomaliesdian. Gray diamonds: Synthetic travel time anomalies calculated from CSEM synthetics. The two numbers on the x axis show distance (bottom) and azimuth (top) in degrees. The lowercase alphabet letter from a to l at the upper left of each panel corresponds to the alphabet letter of the map. Blue arrows point to the data which have large difference between observed and synthetic anomalies. The backgrounds are shaded for the data which mostly sample the Southen Pacific.

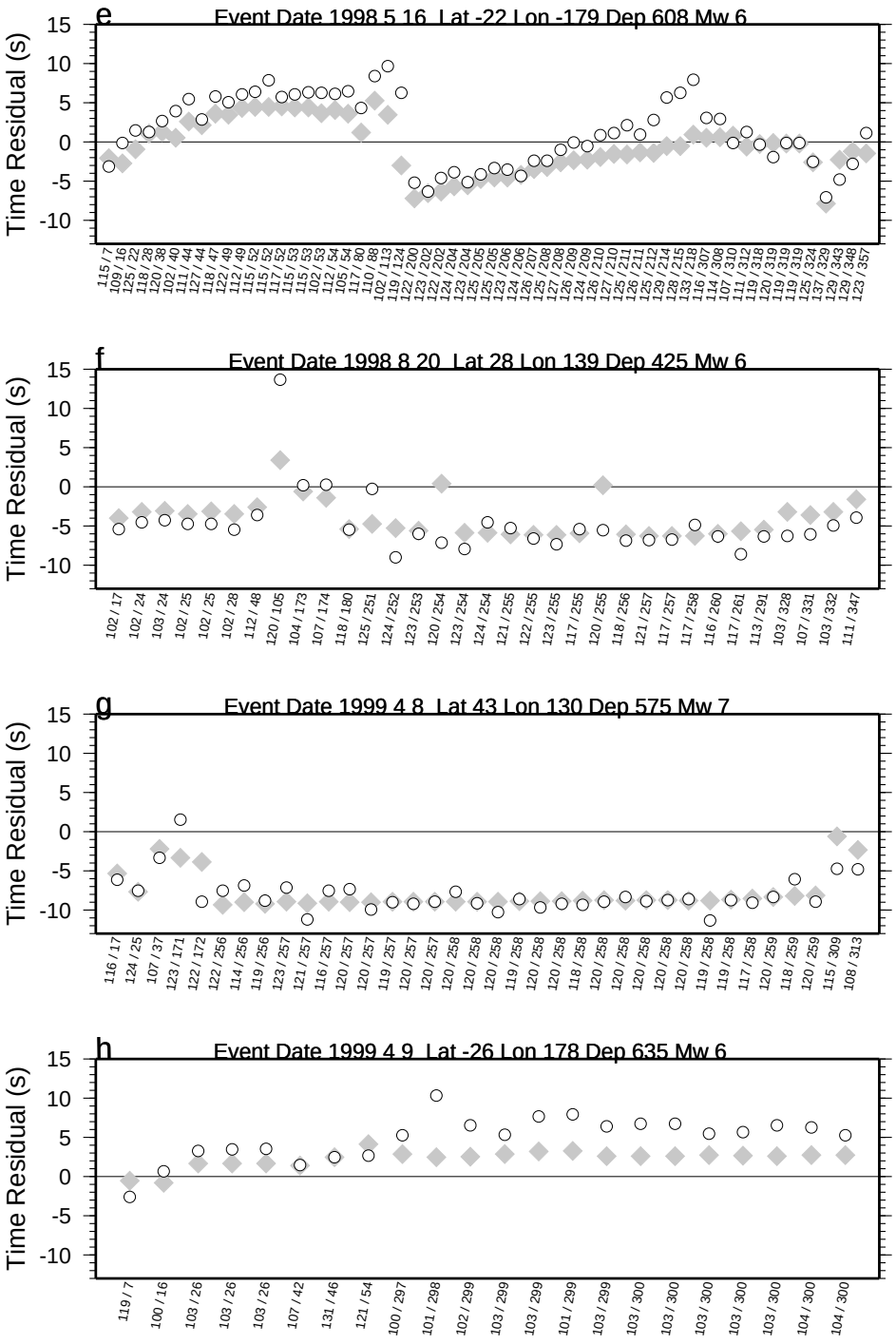

Figure 4.7: Continuation of Figure 4.6

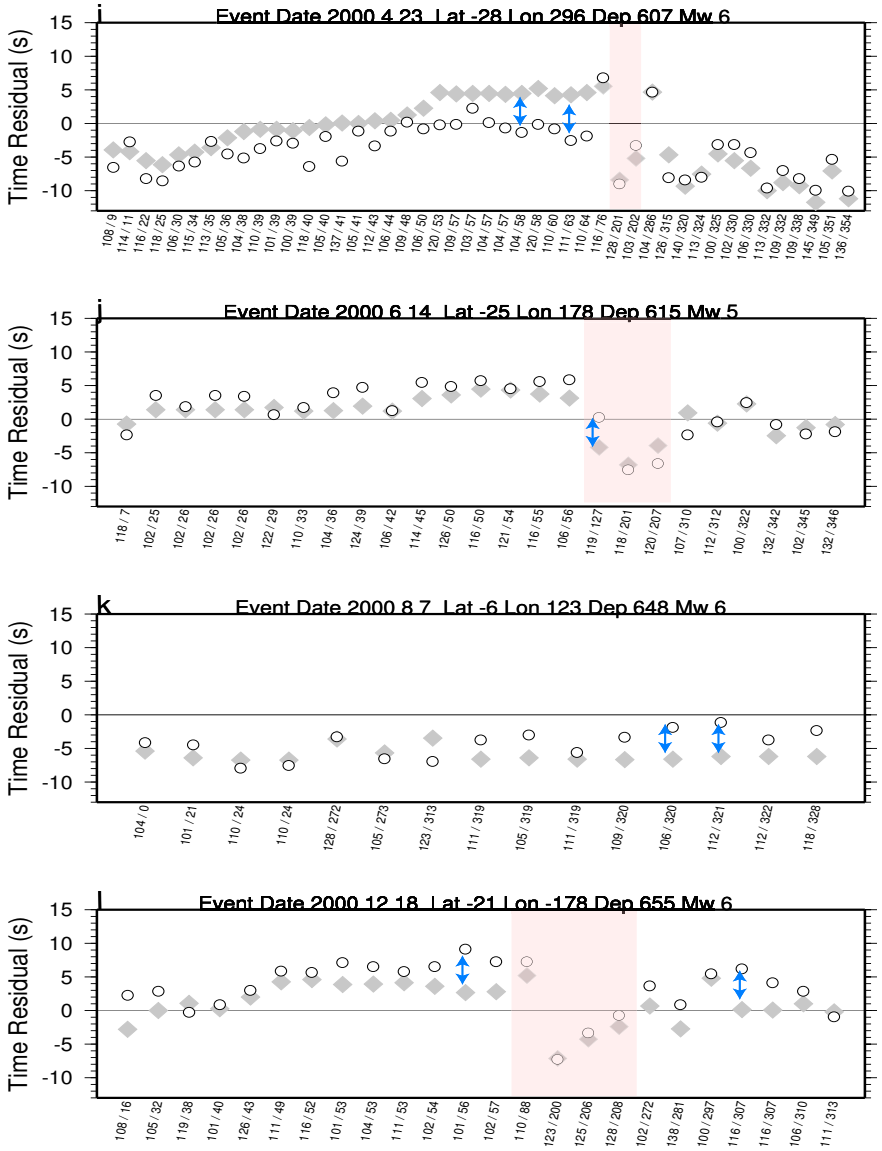

Figure 4.8: Continuation of Figure 4.6

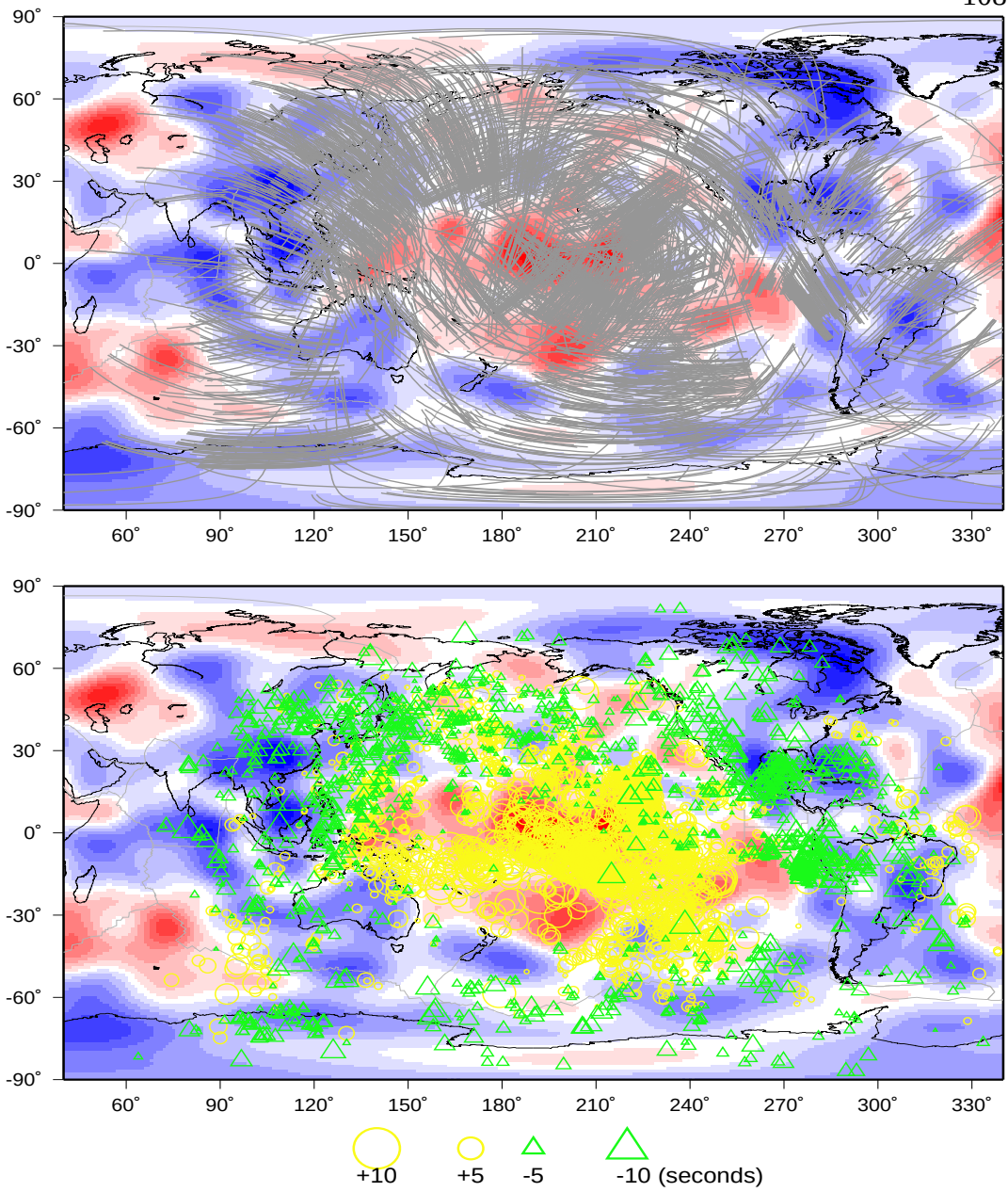

Figure 4.9: Distribution of paths of the measured travel time anomalies. The back ground model is SAW24B16 at the depth of 2850km. Top:Diffracting portion of Sdiff waves. Bottom: Sdiff travel time residuals with respect to PREM is plotted at the midpoint of the paths

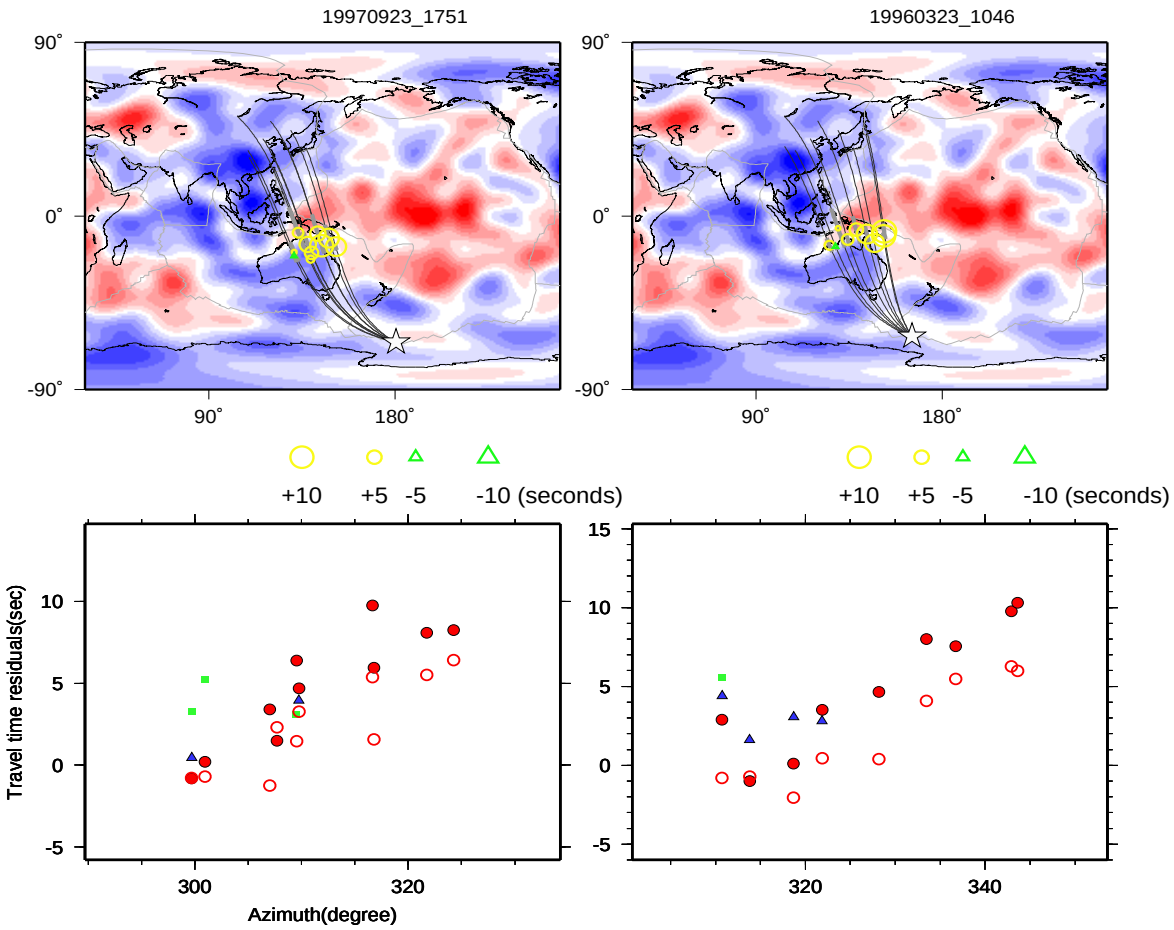

Figure 4.10: Travel time anomaly measurements for the paths which sample the Western Pacific. Top: Sdiff travel time residuals are plotted at the midpoint of the path. Diffracting portion of Sdiff waves are shown in thick gray lines. The back ground model is SAW24B16. The event location is shown by a star. Bottom: Travel time anomalies of Sdiff (solid red circle), SKS (blue triangle) and SKKS (green square) phases with respect to azimuth or back azimuth. Synthetic travel time anomalies obtained by 1D ray theory for SAW24B16 are shown by open red circles. The model gives a good prediction of travel time anomalies for the paths which sample Western Pacific.

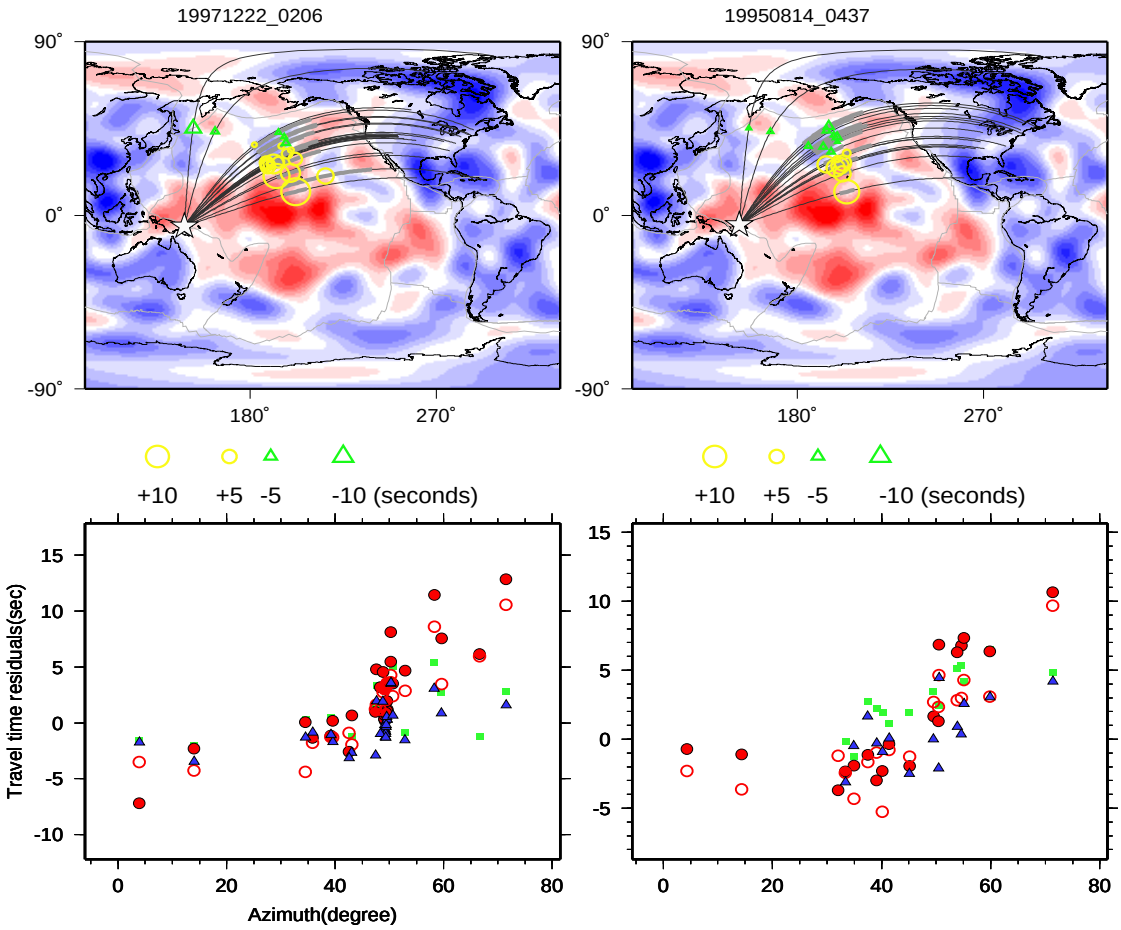

Figure 4.11: Travel time anomaly measurements for the paths which sample the Northern Pacific. The model gives a good prediction of travel time anomalies. Legends are the same as Figure 4.10.

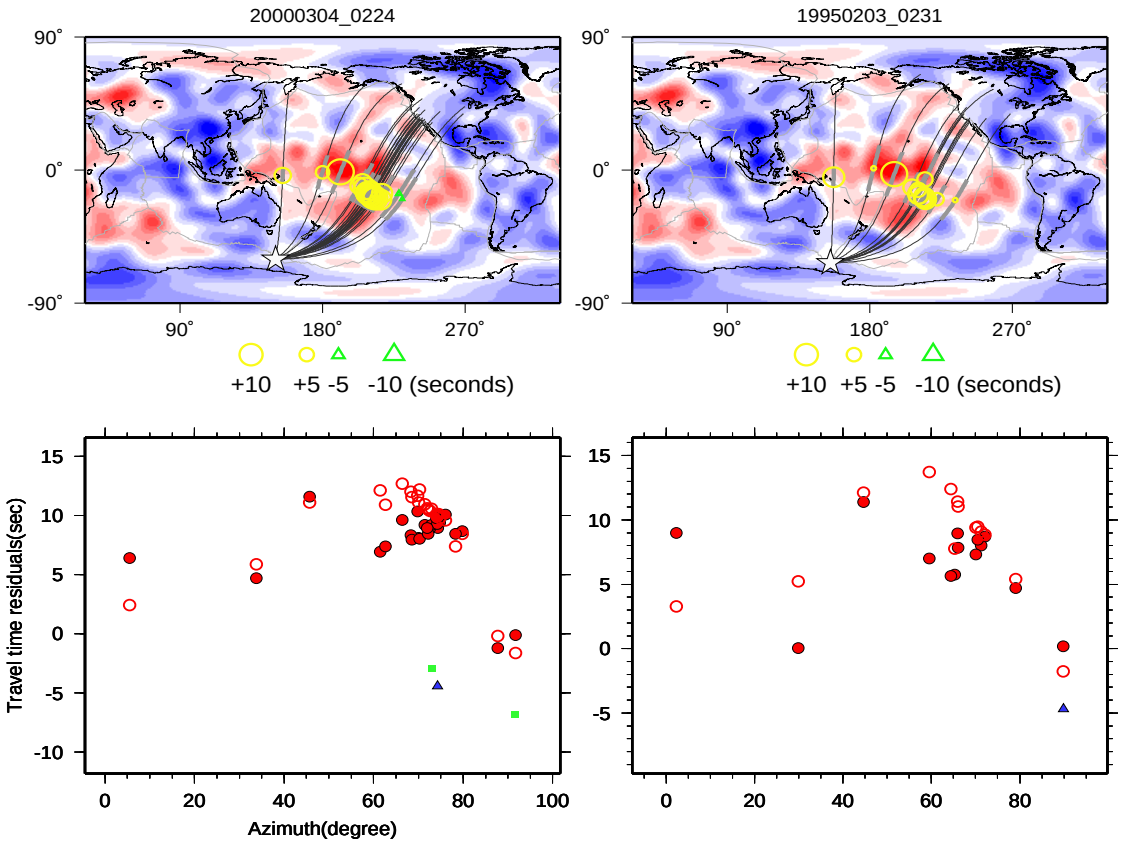

Figure 4.12: Travel time anomaly measurements for the paths which sample inside the Pacific superplume. A few observations show large shift of travel time anomalies within a small distance range. For example, the travel time anomaly jumps are observed at the azimuth of 35 and 80 degrees for the event 20000304_0224(left) and at 35 degrees for the event 19950203_0231. Legends are the same as Figure 4.10.

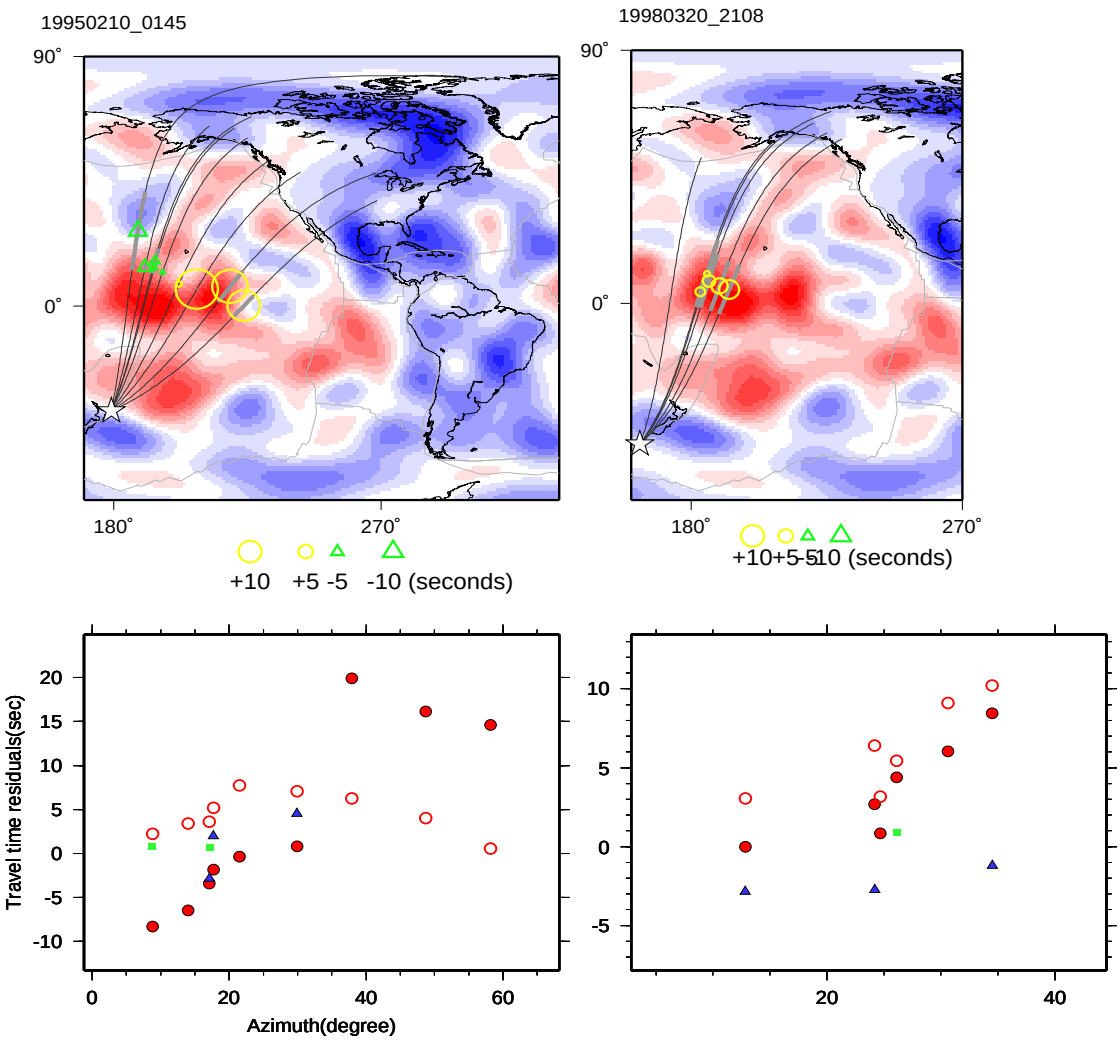

Figure 4.13: Travel time anomaly measurements for the paths which sample inside the Pacific superplume. A few observations show large shift of travel time anomalies within a small distance range. Legends are the same as Figure 4.10.

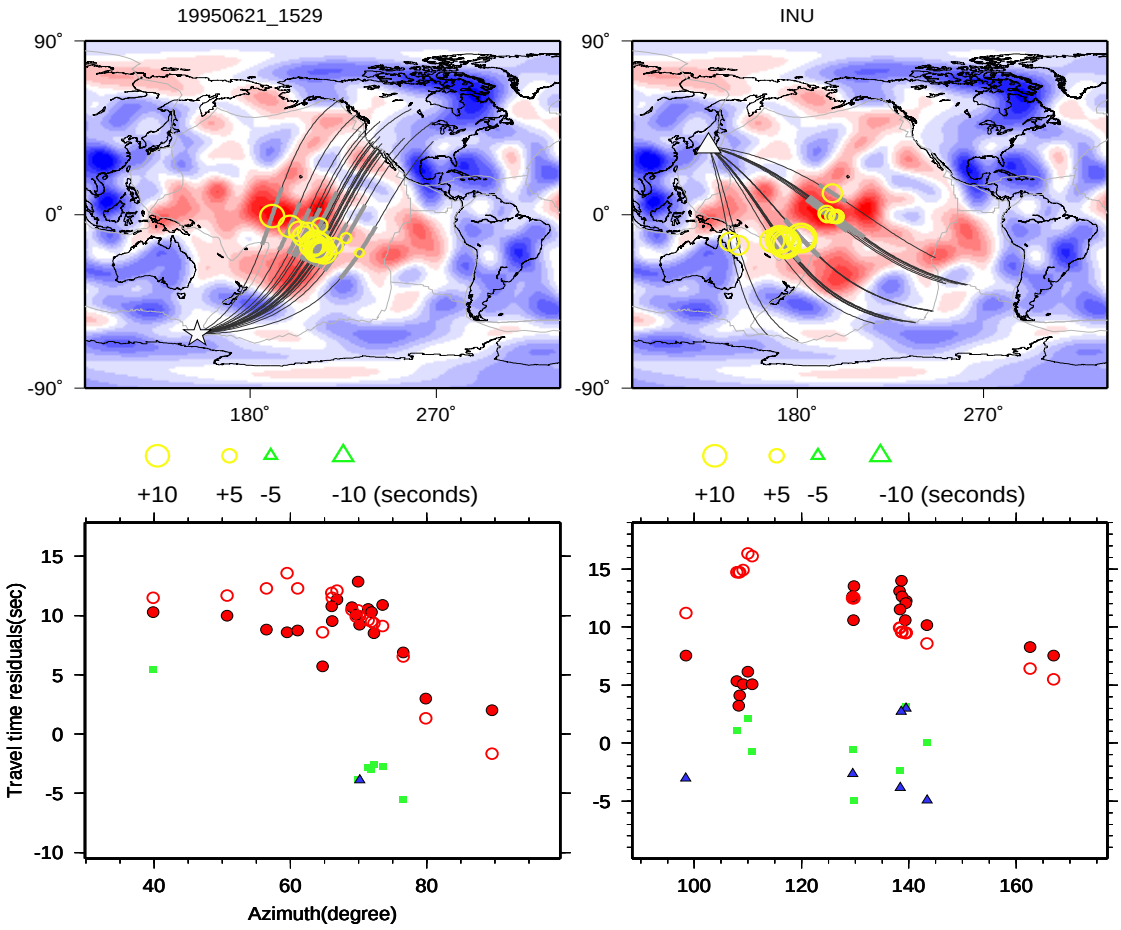

Figure 4.14: Travel time anomaly measurements for the paths which sample the central Pacific. A Large triangle on the map shows the location of a station. Figures show examples of where the model over predicts the anomalies. They are over predicted for the traces at azimuth of 50 deg for the event 19950621_1529 and at 100 deg of back azimuth for the data recorded at the station INU. Legends are the same as Figure 4.10.

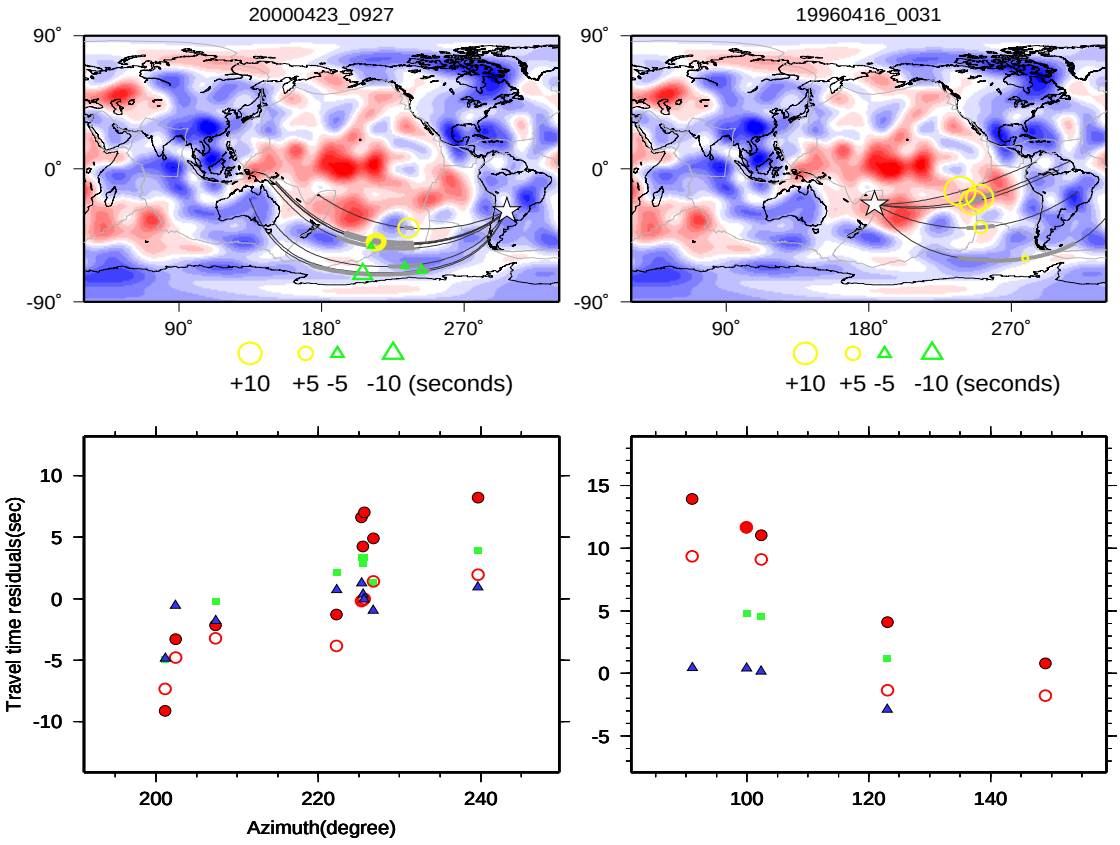

Figure 4.15: More examples of travel time anomaly measurements. A Large triangle on the map shows the location of a station. Figures show examples of where the model underestimates the anomalies. Legends are the same as Figure 4.10.

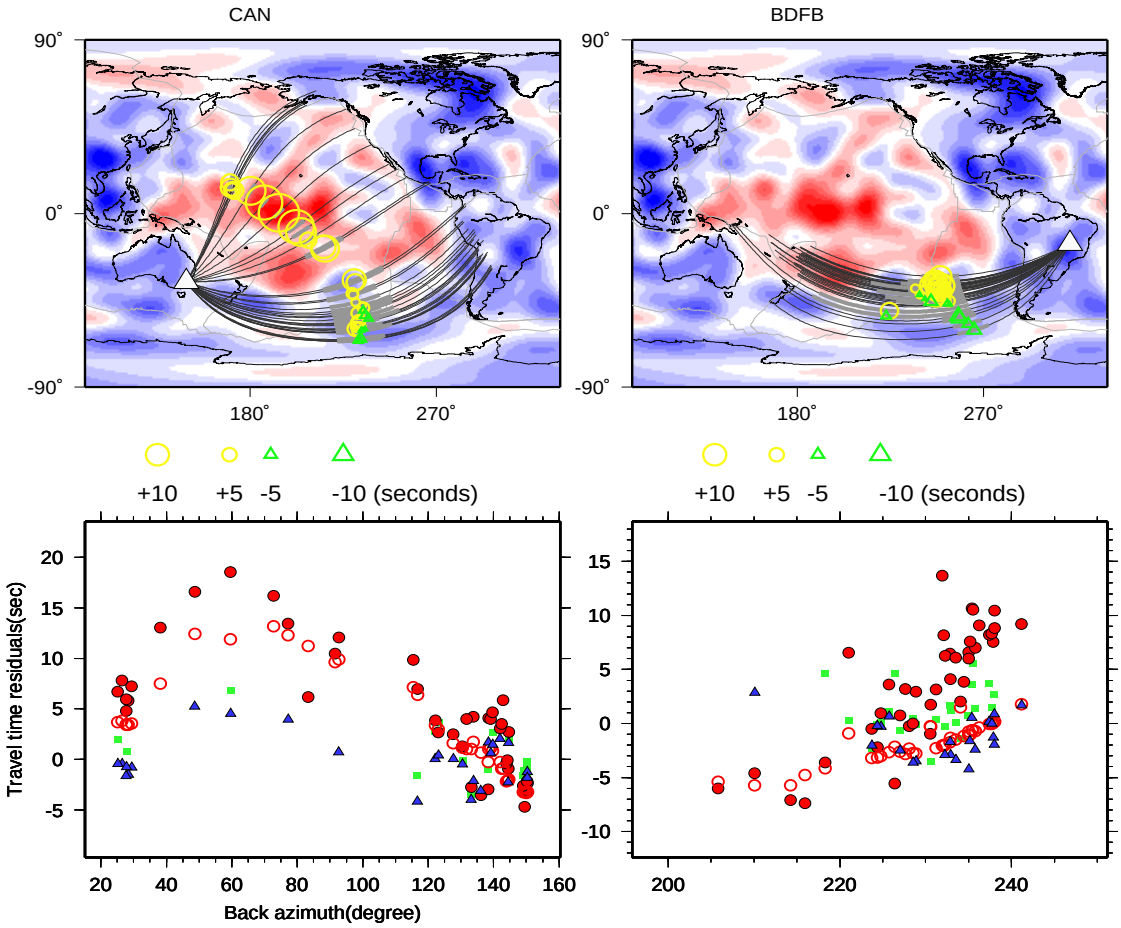

Figure 4.16: More examples of travel time anomaly measurements. The model under estimates the anomalies in the Southern Pacific. Legends are the same as Figure 4.10.

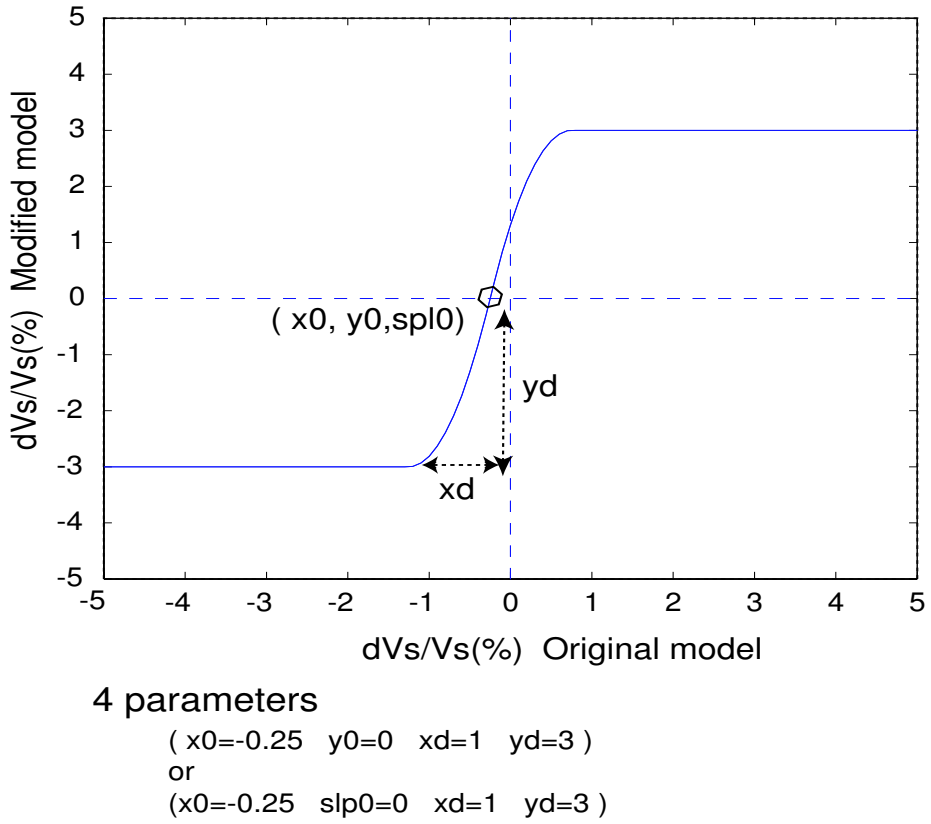

Figure 4.17: Description of a function which is used to modify the anomaly given by the tomographic model. The function is given in 2nd order polynomials. The shape of the function is determined by 4 parameters.

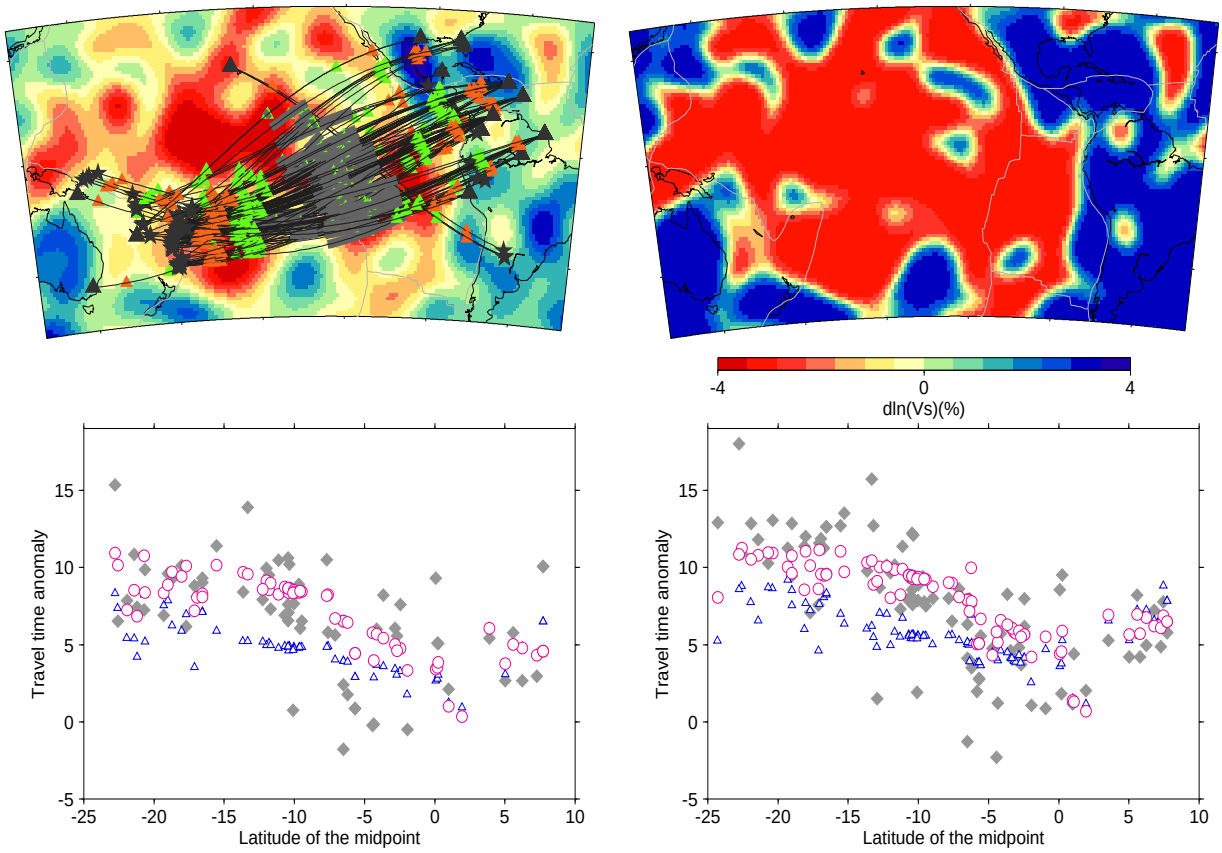

Figure 4.18: Top left: The original SAW24B16 model at the depth of 2891km. The paths of the data which are used in the modeling are plotted. Green triangles show the points where SKKS paths enter and exit the outer core. Red triangles show the points where SKS paths enter and exit the outer core. Top right: The modified model, which best fits the observed travel times, among the tested models. Bottom left: **Sdiff-SKKS** differential travel time anomalies (seconds) with respect to the latitude of mid points (degrees) of the paths. Gray diamonds show the data. Blue triangles show the predicted travel time from the original model. Pink circles are predicted travel times from the modified model. Bottom right: **Sdiff-SKS** differential travel time anomalies with respect to the latitudes of the midpoints of the paths. The synthetic travel times are corrected for the finite frequency effect shown in Figure 4.1.

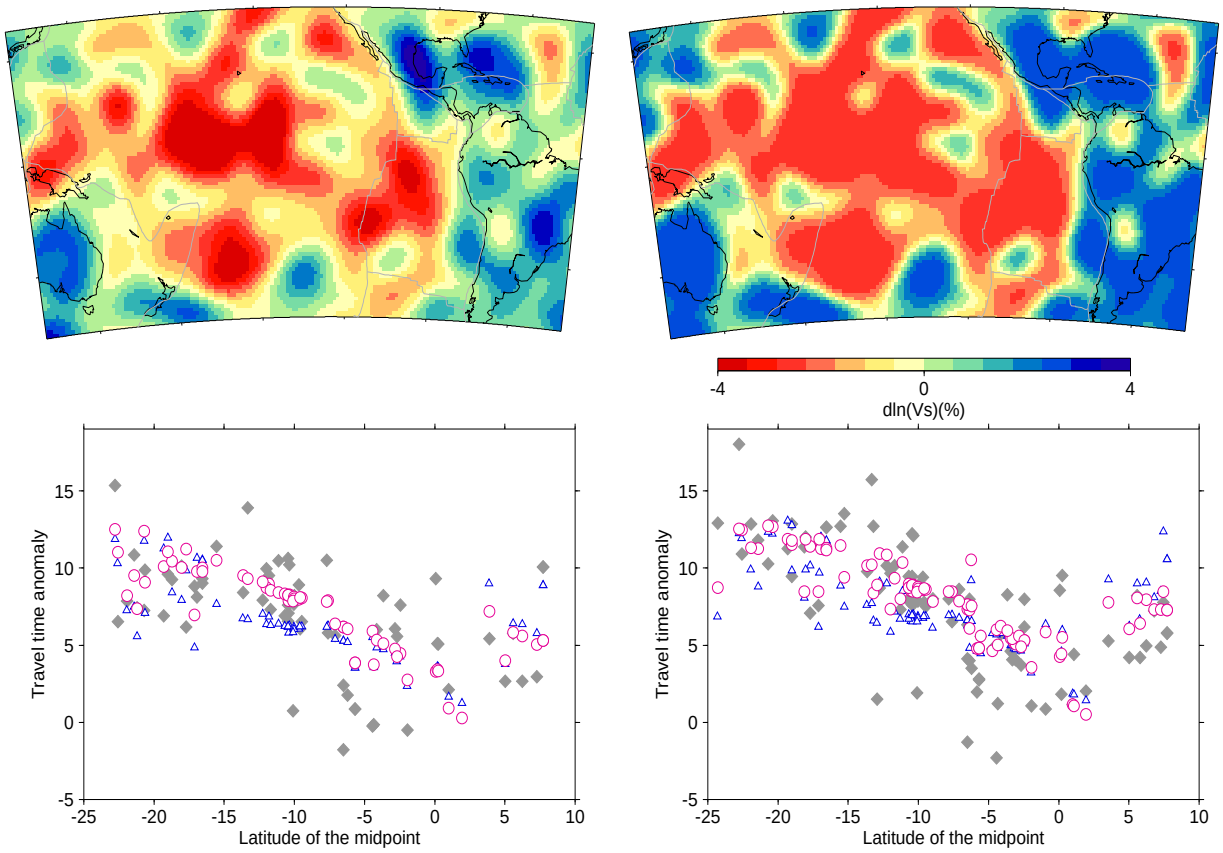

Figure 4.19: Top left: The original SAW24B16 model at the depth of 2891km. Top right: Modified model, which best fits the data. Bottom left: Sdiff-SKKS differential travel time anomalies (seconds) with respect to the latitude of midpoints(degrees) of the paths. Bottom right:Travel time anomalies of Sdiff-SKS differential travel time with respect to the latitudes of midpoints of the paths. Legends are the same as Figure 4.18.

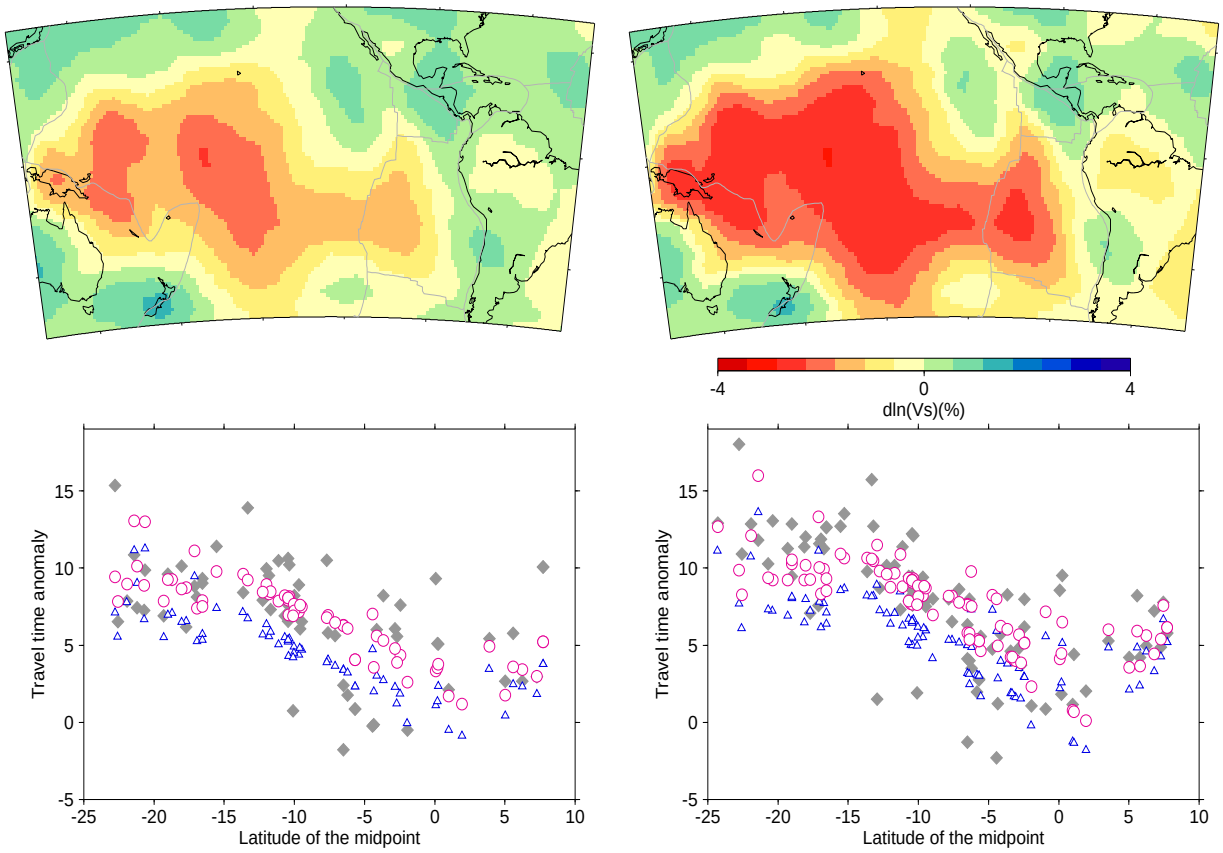

Figure 4.20: Top left: The original SB4L18 model at the depth between 2710 and 2887km. Top right: Modified model, which best fits the data. Bottom left: Sdiff-SKKS differential travel time anomalies (seconds) with respect to the latitude of mid points(degrees) of the paths. Bottom right:Travel time anomalies of Sdiff-SKS differential travel time with respect to the latitudes of midpoints of the paths. Legends are the same as Figure 4.18

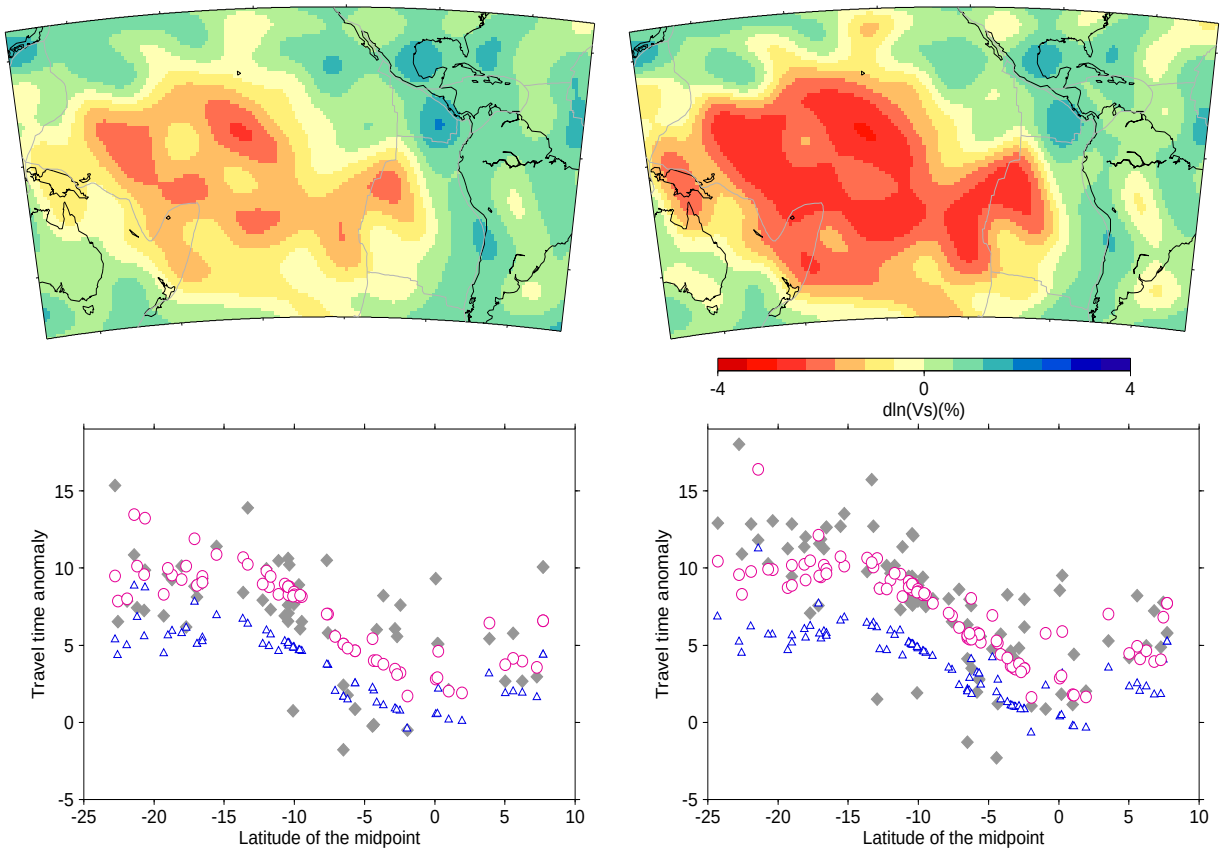

Figure 4.21: Top left: The original of S20RTS model at the depth of 2891km. Top right: Modified model, which best fits the data. Bottom left: Sdiff-SKKS differential travel time anomalies (seconds) with respect to the latitude of mid points(degrees) of the paths. Bottom right:Travel time anomalies of Sdiff-SKS differential travel time with respect to the latitudes of midpoints of the paths. Legends are the same as Figure 4.18.

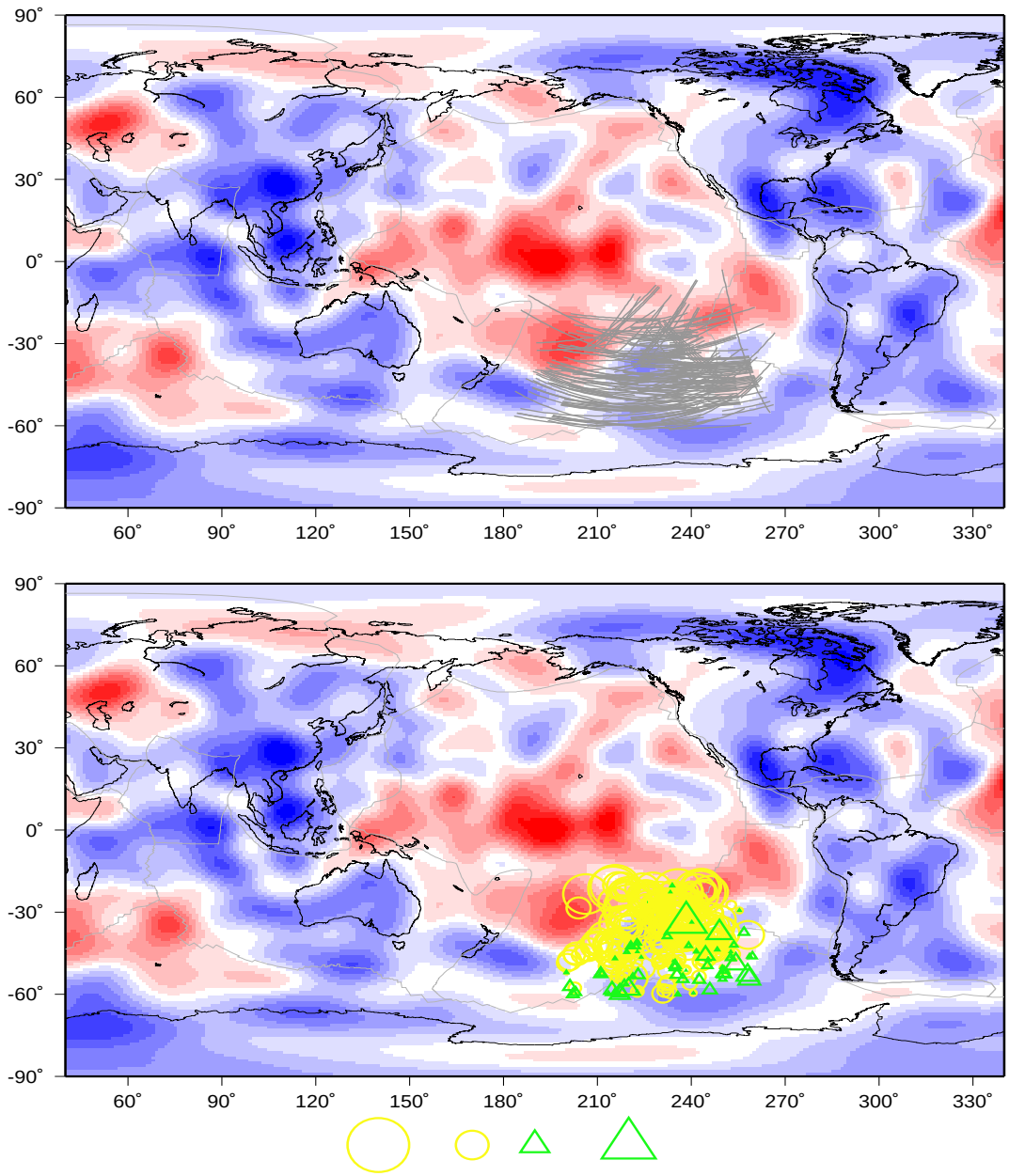

Figure 4.22: The distribution of the paths and the travel time anomalies of the Sdiff phase which were used in the modeling for a Southern Pacific region.

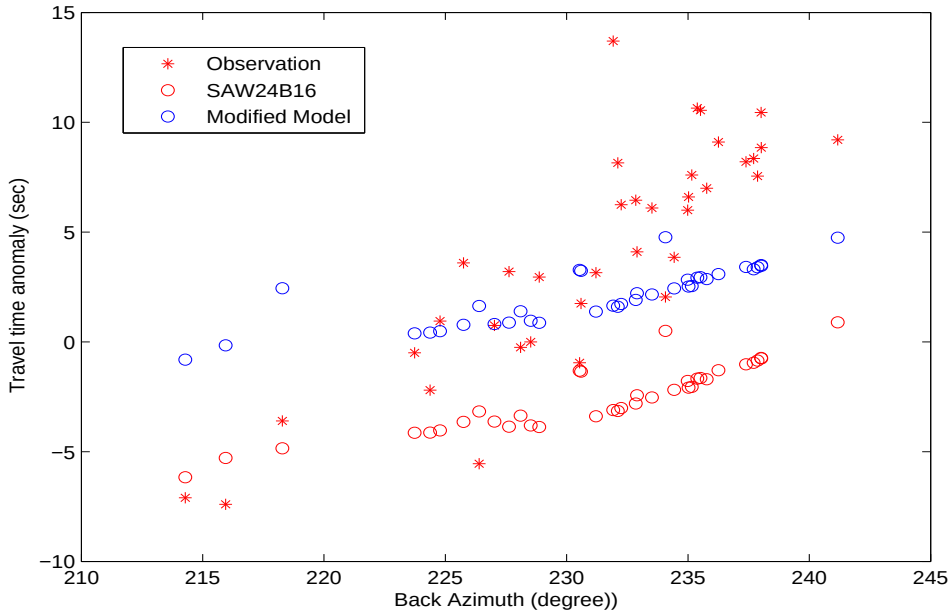

Figure 4.23: Travel time anomalies of Sdiff phases observed in station BDFB in Brazil. The locations of the paths are shown in Figure 4.16. The travel time predictions from ray theory for SAW24B16 (red circle) and a modified model(blue circle) are also plotted. The modified model is obtained by searching for a set of four parameters which best fit the data.

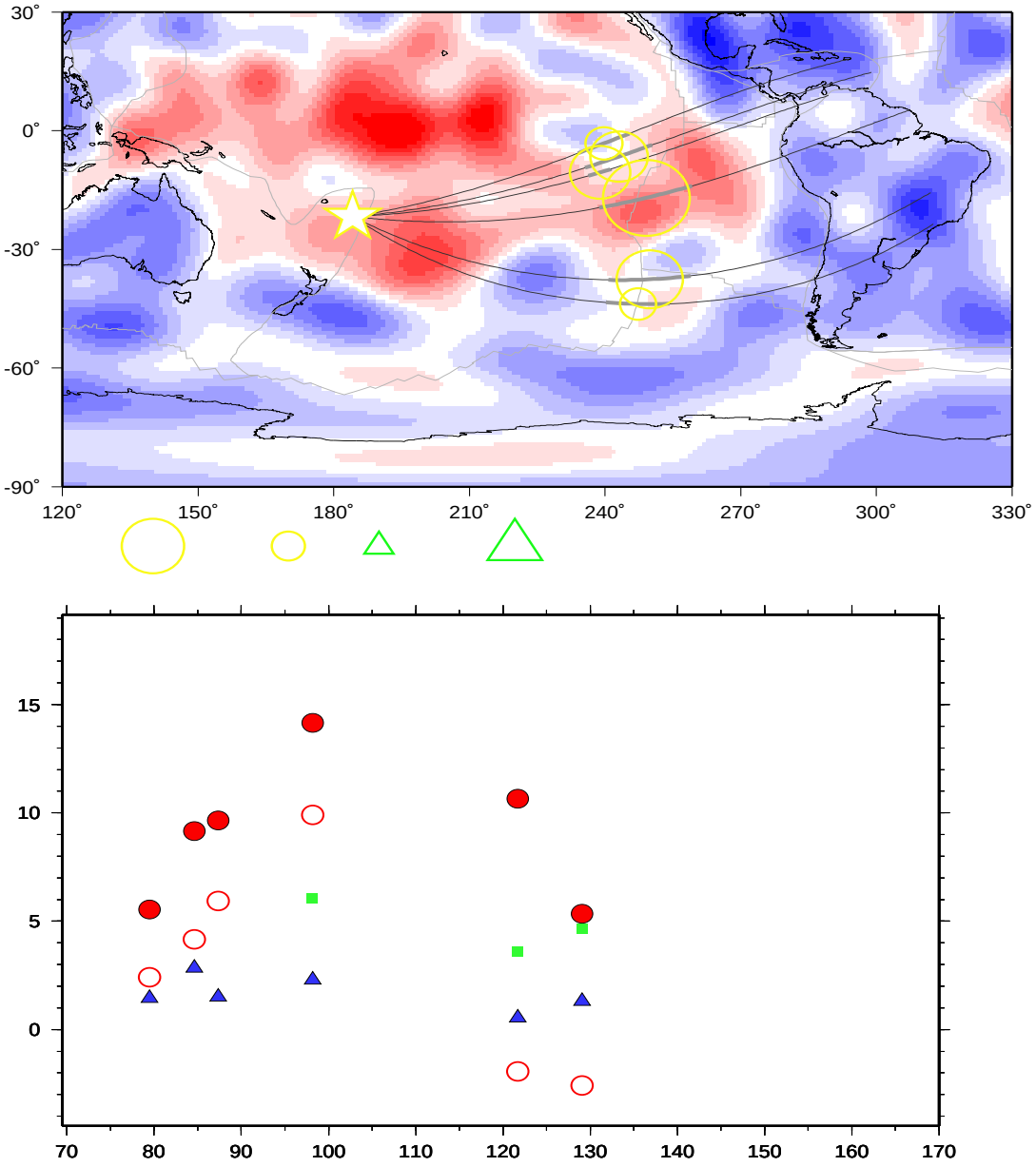

Figure 4.24: Top: The source and recievers of the event which was used in the CSEM calculation. Yellow circles show the travel time anomalies for each path. Bottom: Observed travel time anomalies with respect to azimuth for Sdiff, SKKS and SKS. Legends are the same as Figure 4.18.

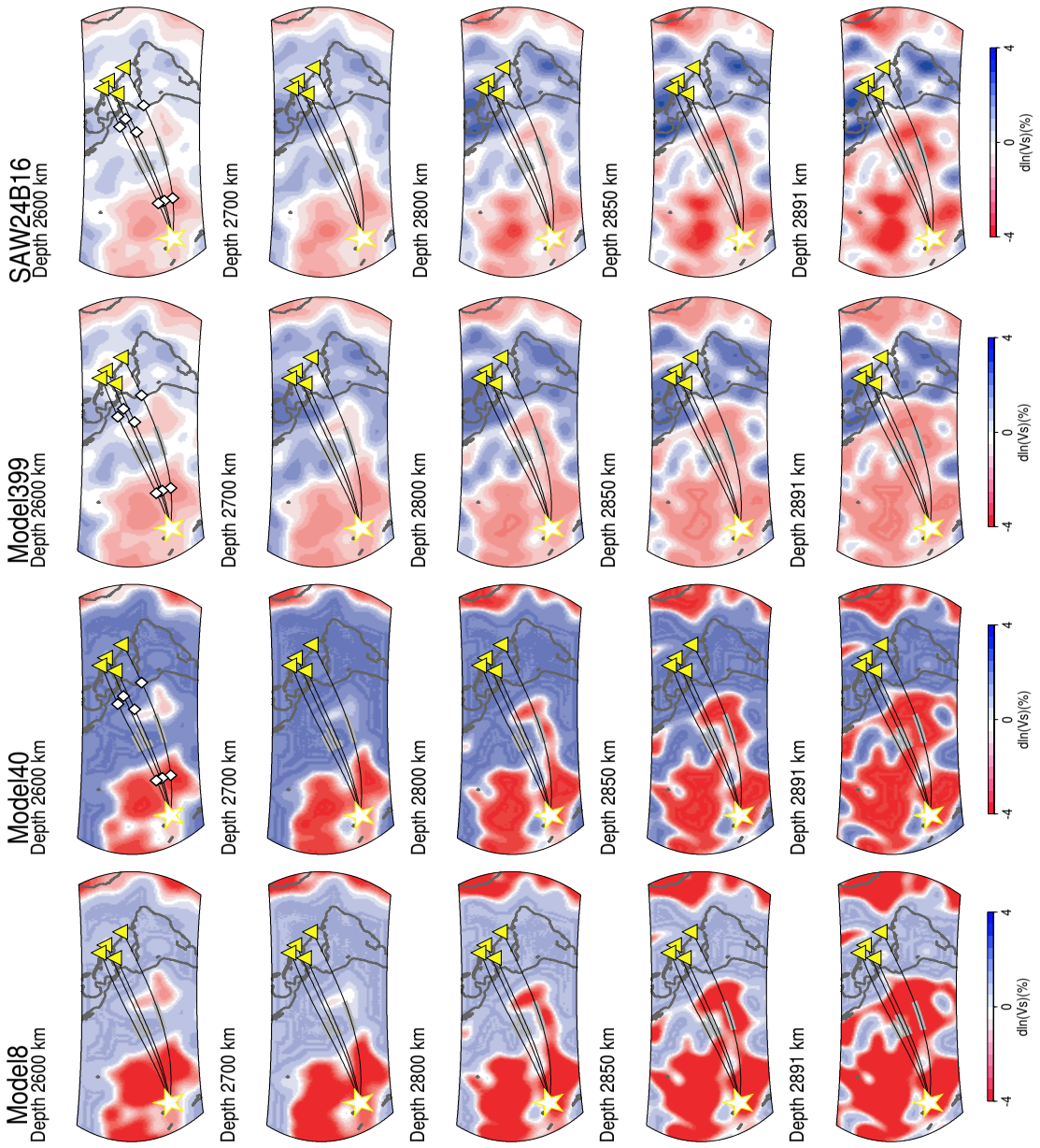

Figure 4.25: Anomaly distributions of the four models which were tested by running CSEM. White diamonds show the points where ray paths of the Sdiff phase enter the D" layer (at a depth of 2600km). The four parameters for each model are as follows: Model8 (x0,y0,xd,yd)=(-1,-2,1,3), Model40 (x0,y0,xd,yd)=(-1,-1,1,3), Model399 (x0,y0,xd,yd)=(0,0,3,2.5).

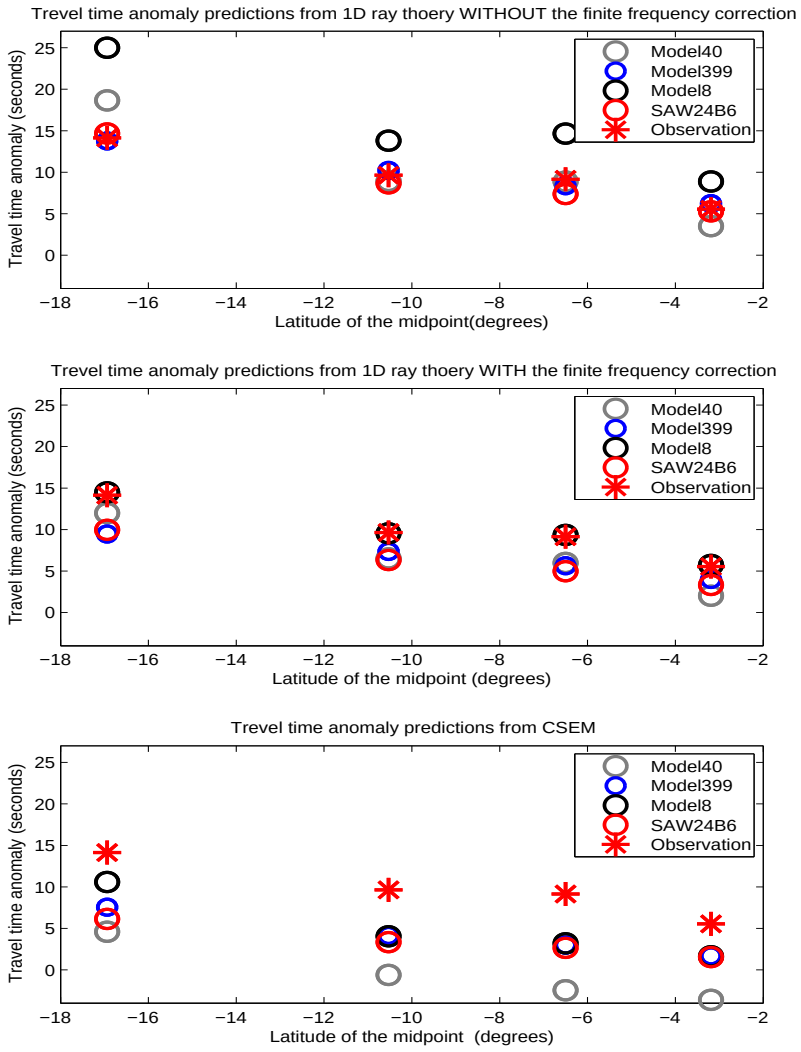

Figure 4.26: Synthetic and observed travel time anomalies with respect to the latitude of the midpoints of the paths. Synthetic travel times are shown by open circles. (a) Synthetic travel time anomalies are obtained by 1D raytheory. The finite frequency correction (Fig. 4.1) dashed line) is not applied. SAW24B16 and MODEL399 fit the data equally well. (b) Synthetic travel time anomalies are obtained by 1D raytheory with the finite frequency correction. MODEL8 best fits the data. (c) CSEM is used to obtain synthetic travel times. MODEL8 shows the best fit to the data. All the models underestimate the anomalies by approximately 5 seconds or more.

Chapter 5

Postseismic deformation stress changes following the 1819 Rann of Kachchh, India earthquake

This chapter has been published in *Geophysical Research Letters* [*To A.; Bürgmann R., Pollitz F. 2004*] with the title ’Postseismic deformation stress changes following the 1819 Rann of Kachchh, India earthquake; was the 2001 Bhuj earthquake a triggered event? ’

Summary

The 2001 Mw 7.7 Bhuj earthquake occurred in an intraplate region showing little evidence of active tectonism, but with rather unusual active seismicity, including an earlier major earthquake, the 1819 Allah Bund earthquake (M7.7). We examine if static coseismic and transient postseismic deformation following the 1819 Great Rann of Kachchh earthquake (M7.7) contributed to the enhanced seismicity in the region and the occurrence of the 2001 Bhuj earthquake, ~ 100 km away and almost two centuries later. Based on the Indian shield setting, great rupture depth of the 2001 event and lack of significant early postseismic deformation seen following the 2001 event, we assume that little viscous relaxation occurs in the lower crust and that the upper mantle has an effective viscosity of about 10^{19} Pas. The predicted Coulomb failure stress on the rupture plane of the 2001 event increased by more than 0.1 bar, which is a small but possibly significant amount. Stress change from 1819 event may have also affected the occurrence of other historic earthquakes in this region. We also evaluate the postseismic deformation and ΔCFS in this region due to the 2001 event. Positive ΔCFS from the 2001 event occur to the NW and SE of the Bhuj earthquake rupture.

5.1 Introduction

The Mw 7.6 26 January 2001 Bhuj earthquake was the most deadly earthquake to strike India in its recorded history; about 20,000 people were killed and 166,000 people were injured (e.g., [*Bendick et al.*, 2001]). Although this region is 300 km from boundaries of the Indian plate, it has experienced several damaging earthquakes (Fig. 5.1). Among those, the 1819 Allah Bund (or Great Rann of Kachchh) earthquake ranks as one of the largest among global intra-plate earthquakes [*Johnston and Kanter*, 1990]. The 1819 earthquake produced an about 90-km-long, 6-km-wide and 3-to-6-m-high uplift known as the Allah Bund ([*Oldham*, 1926; *Bilham*, 1998; *Rajendran and Rajendran*, 2001]). From the surface deformation the magnitude is estimated to be Mw = 7.7±0.2 [*Bilham*, 1998]. Considering the intra-plate setting and apparent low Holocene deformation rates in the region [*Wesnousky et al.*, 2001], the occurrence of two M > 7.5 and ˜ 10 M >5 earthquakes in 200 years warrants evaluation of a causal link between the events leading to such accelerated moment release [*Bendick et al.*, 2001].

Earthquakes and subsequent relaxation processes change the stress in the surrounding Earth's crust and can enhance or delay the occurrence of earthquakes on nearby faults. Here, we examine the possible connection between the occurrence of the 1819 Allah Bund earthquake and the 2001 Bhuj earthquake located about 100 km away. Numerous studies have shown a correlation between calculated positive coseismic stress changes (shear and normal stresses calculated using elastic dislocation models) and the location of after-

shocks as well as triggering of moderate to large earthquakes [*Harris*, 1998]. Coulomb stress changes of > ~0.1 bar have been found to significantly impact seismicity patterns [*Reasenberg and Simpson*, 1992; *Harris*, 1998; *Stein* , 1999]. It has been suggested that postseismic relaxation in the lower crust and upper mantle also plays an important role in stress transfer and earthquake triggering.

For example a sequence of M>8 eathquakes occurred in Mongolia from 1905 to 1967, where background loading is comparatively small. Each event occurred more than 10 years and 100 to 400 km apart. Cosesimic stress changes are small at the remote distances and it is difficult to explain the 10 to 30 years time intervals between events. The earthquake sequence is well explained by taking into account the large and far reaching stress changes from postseismic viscous flow in the crust and upper mantle [*Chéry et al.*,2001; *Pollitz et al.*, 2003].

Here, we explore quantitatively, in the framework of the Coulomb failure criterion, the idea that both coseismic and postseismic stress changes from the 1819 earthquake increased the likelihood of failure at the site of the 2001 event. We also calculate predicted regional surface displacements and stress changes resulting from the 2001 earthquake and subsequent relaxation.

5.2 Model Calculations

We compute coseismic [*Pollitz* , 1996] and postseismic [*Pollitz and Sacks*, 1997] deformation and stress changes using spheroidal and toroidal motion modes of a spherically stratified elastic-viscoelastic medium. The model is parameterized by specifying the fault geometry and slip of the source event and the depth dependent elastic and viscous parameters. Coulomb stress changes are evaluated along the slip direction on the receiver fault, such as on planes parallel to the rupture of the 2001 earthquake, and at a depth of 20 km, near which the 2001 earthquake nucleated.

5.2.1 1819 source rupture model

The fault parameters chosen for the 1819 event are based on [*Bilham*, 1998] and [*Bilham et al.*, 2003]. Bilham(1998) suggested a shallow (from 10 km to near the surface) reverse-slip rupture on a 90-km-long $50-70^{\circ}$ N-dipping fault plane to match the measured elevation changes from the event. Bilham et al. (2003) take the great depth and short lateral fault length of the 2001 rupture into consideration and incorporate new topographic and remote sensing observations of the morphology of the Allah Bund fault scarp to obtain updated fault parameters. The 1819 event is estimated to have a 50-km-long rupture dipping 45° to the north with 3-8 m slip. The slip is set to 5.5 m in this study, consistent with a Mw$\bar{7}$.7 earthquake for a rupture extending to 30-km depth.

5.2.2 Depth dependent viscoelastic parameters

The magnitude and pattern of postseismic deformation and stress changes depend strongly on the rheological layering of the crust and upper mantle, which in turn depends on composition, temperature and other environmental parameters. Seismic data show a Moho depth of 35-40 km [Sarkar et al, 2002], which suggests that the 2001 earthquake and its 10-32-km-deep aftershocks ruptured to near the base of the crust. Thus the Indian shield is apparently significantly colder and less viscous than many plate boundary zones. Figure 5.2 shows the rheological model, which we adopt here. Density, bulk modulus, and shear modulus are consistent with seismic velocity and density layering used in other studies [*Antolik and Dreger*, 2003; *Negishi et al.*, 2002]. We chose the model viscosity of the upper mantle by calculating postseismic displacements for the 2001 Bhuj earthquake using a range of viscosity values, between 1.5×10^{17} and 1.5×10^{21} Pas, and by comparing the estimated deformation transients with early GPS measurements spanning a 6-month time period [*Jade et al.*, 1990; *Miyashita et al*, 2001]. We adopted a model upper mantle viscosity of 1.5×10^{19} Pas.

5.2.3 Stress change calculations

We calculate the coseismic and postseismic changes in coulomb failure stress (ΔCFS) on the receiver fault. The geometry and slip direction (strike, dip and rake) of the receiver fault

need to be specified for this calculation. Positive change in ΔCFS indicates the increase in likelihood of failure on the receiver fault. It is given by $\Delta CFS = \sigma_s + \mu'\sigma_n$, where σ_s s is the change in shear stress in the slip direction on the receiver fault, σ_n is the change in normal stress (tension positive), and μ' is the apparent coefficient of friction incorporating the influence of pore pressure. μ'value of 0.2 to 0.8 are widely used in other studies [*Harris*, 1998]. We present calculated ΔCFS given a range of friction coefficients, as well as changes of σ_s and σ_n (Figure 5.3). The receiver fault geometry of [*Antolik and Dreger*, 2003] for the Bhuj earthquake is adopted (strike = 82°, dip = 51°, rake = 77°)

5.3 Results

5.3.1 1819 earthquake coseismic and postseismic stress changes

Figure 5.3 shows the ΔCFS change from the 1819 event evaluated for faults with the geometry of the 2001 event. The 1819 coseismic shear- and normal-stress changes at the hypocenter of the 2001 earthquake, are 0.06 bar and -0.09 bar, respectively, but stresses rise to 0.30 bar and -0.36 bar following 182 years of postseismic deformation. Within the range of μ ' from 0.2 to 0.8, ΔCFS is positive at the location of the 2001 event. When μ 'is set to 0.4, ΔCFS at the 2001 event location is 0.02 bar for the coseismic and 0.16 bar for the postseismic deformation (Fig. 5.3(a) and Fig. 5.3(b)). The stress change at the

2001 hypocenter from the postseismic relaxation is 4 7 times greater than the immediate coseismic loading, which points to the importance of considering the contribution from viscoelastic relaxation of the lower crust and upper mantle in fault-interaction calculations. The change in ΔCFS from the Mw 6.1 1956 Anjar earthquake (Chung and Gao (1995) at the location of 2001 is evaluated to be positive but very small (about +0.01 bar).

5.3.2 Postseismic deformation of 2001 Bhuj event

To consider the potential impact of the Bhuj earthquake on future seismicity in the region and in anticipation of continued postseismic deformation measurements, we also evaluate the postseismic deformation and ΔCFS in this region due to the 2001 event. We constructed a coseismic fault model of the Bhuj earthquake based on the Harvard CMT solution, aftershock locations [*Negishi et al.*, 2002] and finite fault slip inversion results [Antolik and Dreger, 2003]. Strike, dip, rake and moment magnitude are set to 65°,50°, 50°, and 3.6 $\times$1020 Nm, respectively. The slip distribution of [*Antolik and Dreger*, 2003] is taken into account, with larger amount of slip (8.2 m) confined to a small area in the center (25 $\times$15 km2) and less slip (1.7m) in the surrounding part. The model rupture is 40-km long and 10-to-32-km deep. To first order, major faults in the Rann of Kachchh region strike approximately in an E-W direction, dipping 40° to 50° to the south in the southern part and to the north in the northern part of the region. The faults in this region were formed under N-S tension, before the change to N-S compression occurred around 40 Ma, and therefore

they have steeper dips compared to usual thrust faults [*Wesnousky et al.*, 2001]. We set the receiver fault slip parameters to strike=270°, dip=45°, with a rake of 90°. The result is same for faults dipping 45° south or north. Figure 5.4 shows coseismic and postseismic (calculated for 2011) ΔCFS from the 2001 event, as well as the surface displacement field predicted from this model. Positive ΔCFS from the 2001 event occur to the NW and SE of the Bhuj earthquake rupture. If we consider the fault locations in the Rann of Kachh region, postseimic relaxation from the 2001 event enhances the stress on the Kachchh Mainland fault and faults in the Wagad highlands. The ΔCFS is slightly negative on the Katrol Hill fault. However, the change of ΔCFS depends on the receiver fault geometry and one should use the specific fault parameters for better estimation of enhanced or reduced likelihood of failure on individual faults.

5.4 Discussion

5.4.1 Model sensitivity analysis

We examined the sensitivity of ΔCFS to the geometry of the 1819 fault rupture, the rheology stratification of the model and the geometry of the receiver fault. The results are provided in the electrical supplements. In all of the models considered, we find more then 0.1 bar Coulomb stress increase on the 2001 event rupture. As stress changes as low as 0.1

bar can enhance the occurrence of an earthquake [*Harris*, 1998], we conclude that the post-seimic relaxation following the 1819 earthquake enhanced the loading on the 2001 rupture by a small, but possibly significant amount.

5.4.2 Stress changes at location of other 1819-2001 earthquakes

We examined whether the stress change from the 1819 event affected the occurrence of other historic earthquakes in this region (shown in Figure 5.1). Although the locations of the pre-instrumental events are not well known [*Rajendran and Rajendran*, 2001], all M > 5 events occurred in the region where CFS increased by coseismic and postseimic loading from the 1819 event, if the receiver fault geometry is assumed to be an east-west striking, 45° north or south dipping fault plane. The calculated ΔCFS from coseismic and postseismic deformation for each event are +0.5 bar (1864), +0.6 bar (1903), +0.4 bar (1940), +0.6 bar (1966), +0.7 bar (1985) and +0.2 bar (1956). Bilham (2003) proposed the possibility that the rupture of 1819 event only ruptured along 50 km of 90 km long Allah Bund and that the subsequent 1845 event may have ruptured an adjacent segment to the west in a region where our calculations show coseismic and 25 years of postseimic deformation increased the Colomb failure stress by up to 1 4 bar along the Allah Bund strike.

5.5 Conclusions

The coseismic and postseismic stress changes from the $Mw \approx 7.7$ 1819 Allah Bund earthquake encouraged failure on the 2001 Bhuj rupture fault plane. Computed ΔCFS changes range from 0.09 - 0.25 bar, depending on the choice of source and receiver fault geometry and the model rheology parameterization. Postseismic stress changes at the location of the 2001 earthquake exceed coseismic values by about a factor of 4 to 7. Other historic earthquakes in the region that occurred since 1819 also dominantly occurred in regions of enhanced ΔCFS from the 1819 earthquake. Coseismic and postseismic stress changes from the Mw=7.6 2001 Bhuj earthquake will lead to comparable regional stress perturbations in the Rann of Kachchh region and might thus result in continued enhanced earthquake activity in an extended earthquake sequence in an otherwise low-strain rate, intra-plate setting.

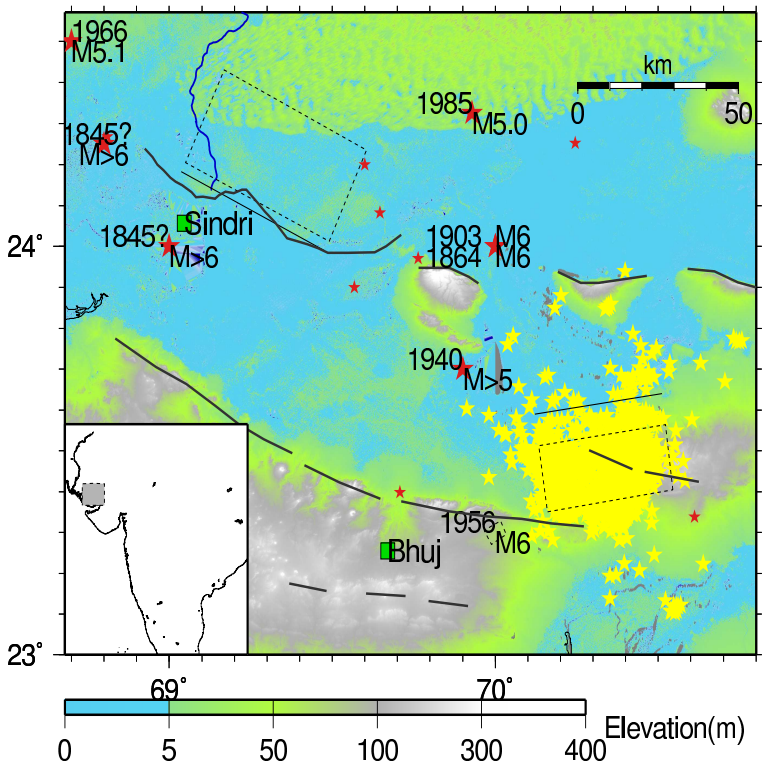

Figure 5.1: The location of major faults and post-1819 earthquakes (after [*Rajendran and Rajendran*, 2001] for 1819-1966 events, and using USGS-NEIC catalog for instrumentally recorded events.) Events of M > 5 are shown by large red star, M < 5 from USGS-NEIC catalog are shown by small red star. Dashed rectangles lines the fault geometry of the 1819, 1956, and 2001 events. The intersections of the faults with the surface are shown in thick gray lines. Yellow stars are aftershocks of the 2001 event.

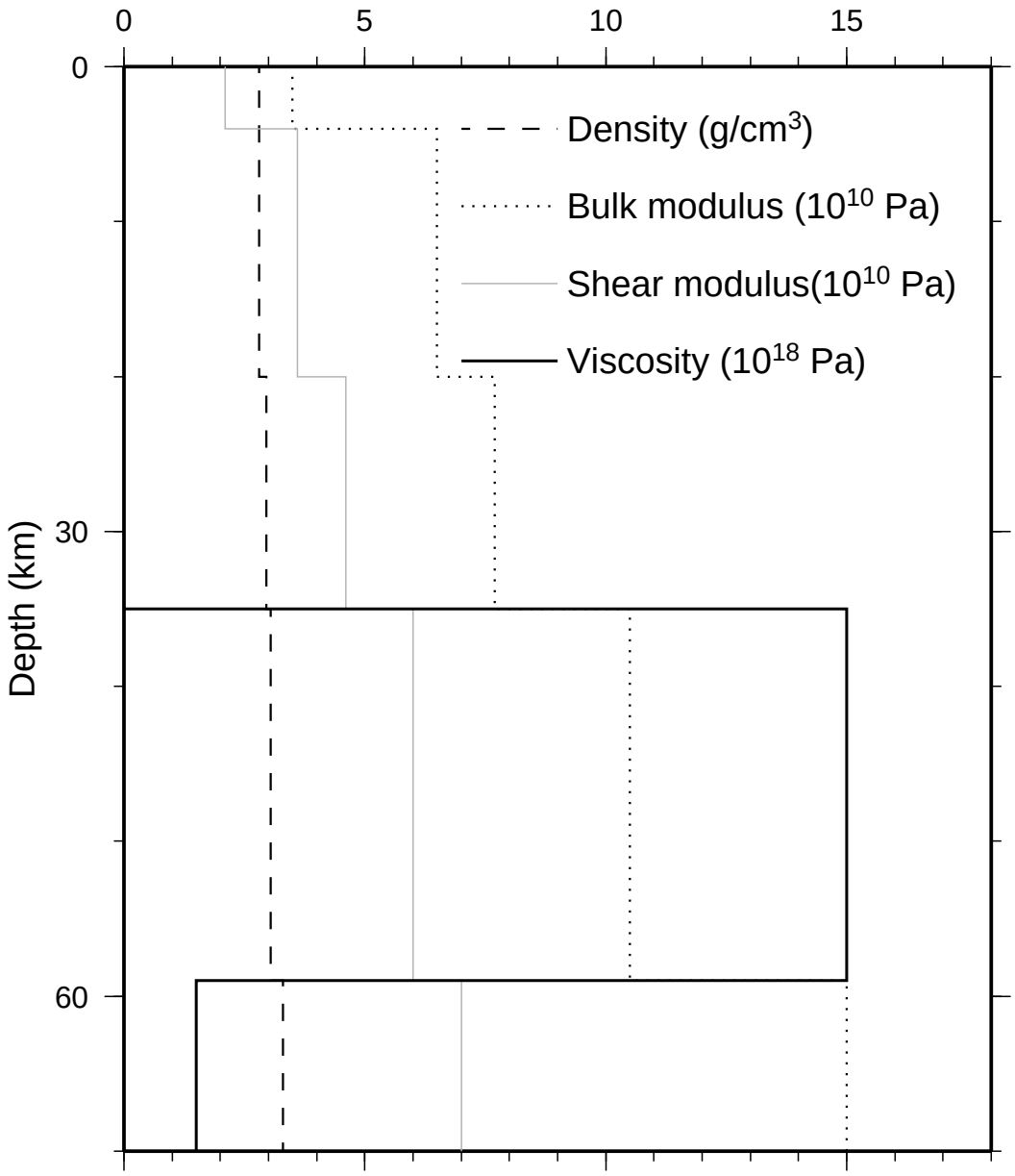

Figure 5.2: Viscoelastic stratification used for the calculation. Upper-mantle viscosities of 1.5×10^17, 1.5×10^19 and 1.5×10^21 Pas were considered.

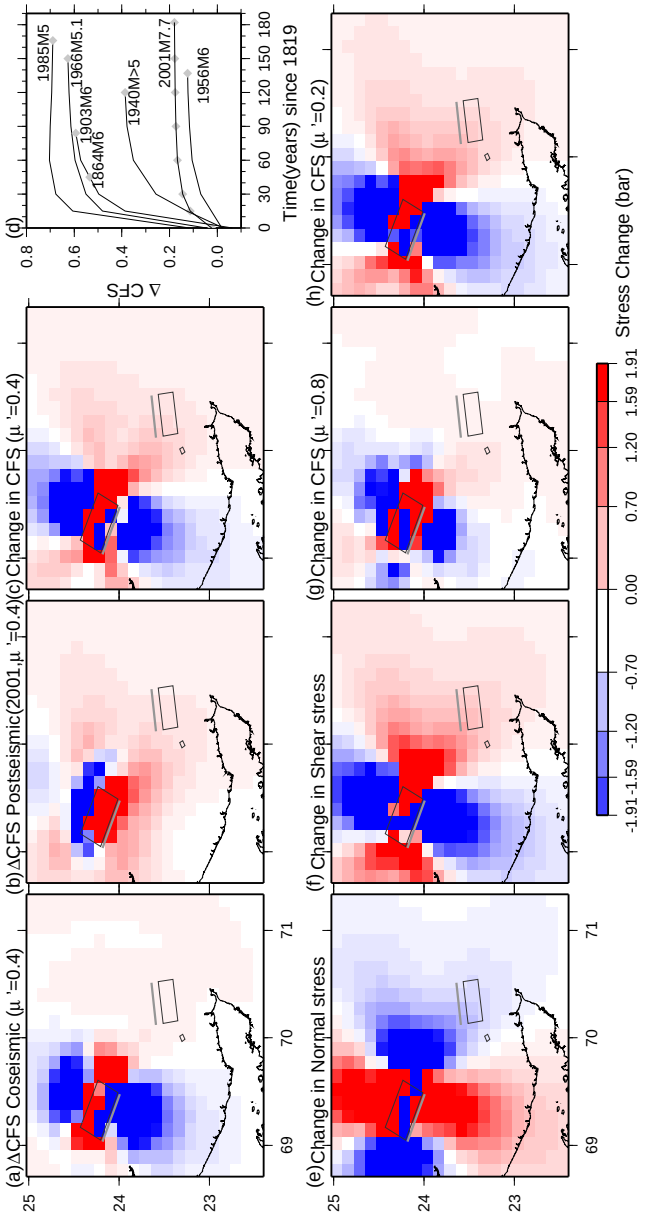

Figure 5.3: $\Delta CFS(\mu' = 0.4)$ from (a) coseismic, (b) postseismic, and (c) coseismic and postseicmic deformation. (g) and (h) show ΔCFS. from coseismic and postseismic deformation with μ' set at 0.2 and 0.8. The fault geometry of the 2001 rupture obtained from [*Antolik and Dreger*, 2003] is used and ΔCFS are evaluated at a depth of 20 km at the time of the 2001 earthquake. (e) and (f) show change of normal and shear stress from coseismic and postseimic deformation. (d) Change of CFS with time since 1819 at the hypocenter of the 2001 event and other M >5 events in the region $(\mu' = 0.4)$. Stress changes are calculated for E-W striking, $45°N$ or S-dipping reverse faults except for the 2001 [*Antolik and Dreger*, 2003] and 1956 event [*Chung and Gao*, 1995].

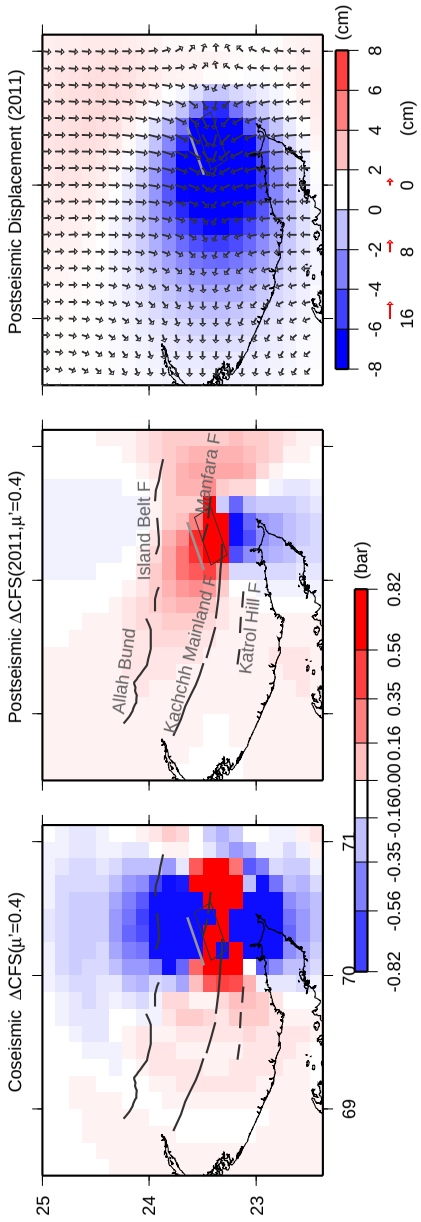

Figure 5.4: CFS (μ' = 0.4) and postseismic surface displacements from 2001 event evaluated for 10 years after the event. Stress changes are calculated for E-W striking, 45° N or S-dipping reverse faults.

Chapter 6

Conclusions

We have carried out a series of studies to better understand the structures, particularly the amplitudes and gradients of Vs anomaly, in the D” layer.

We developed a waveform modeling tool which is suitable to apply to relatively high frequency S diffracted waveforms which propagate through strongly heterogeneous D” regions. The accuracy of the method is checked against normal mode summation in simple models and shows a satisfactory precision. The comparison of observed Sdiff seismograms for paths sampling the D'' across the Pacific, with synthetics computed in an existing tomographic model in which heterogeneity has been restricted to the bottom 370km of the mantle, shows surprisingly good agreement not only in phase, but also in amplitude (in contrast to PREM synthetics) at least down to a 12 s corner frequency. This indicates that

3D effects not accounted for by the theoretical approximations used in the construction of model SAW24B16 are not systematically dominant.

We applied the method to observed Sdiff waveforms to constrain the structure in the D" layer beneath the Indian Ocean. The SHdiff waveforms, which graze the southeastern edge of the African superplume, have previously been reported to show a rapid arrival time shift and a broadening of the waveforms with respect to the azimuth. In addition the waveforms show a secondary pulse that follows the direct Sdiff phase. The comparison of waveform data with CSEM synthetics indicates that the postcursors can be explained by simple 3D structure effect in the D" region with a sharp, quasi-vertical boundary aligned almost parallel to the ray path. When including 3D effects in the modeling, we find that the velocity contrast across the sharp boundary is of the order of 4-5%, averaged over the last 300 km of the mantle, which is smaller than has been proposed in some studies, but larger than in existing tomographic models, implying that the "superplume" features at the base of the mantle cannot be purely thermal.

We showed that a set of SHdiff waveforms, which grazed the southern border of the Pacific superplume, have similar features to waveforms which grazed the southeastern edge of the African superplume. The similarity of the two observed SHdiff waveform sets at relatively high frequencies indicates that the low velocity regions in the lower mantle under the Pacific Ocean and Africa, corresponding to the strong degree-2 pattern in shear velocity tomographic models, have a similar nature also at finer scales.

We also examined how well the anomalies are resolved in the tomographic model in other regions of the D" layer. The comparison of synthetic travel time anomalies between CSEM and NACT shows the limitations in the ability of NACT to handle the effects of large amplitude Vs anomalies. The comparisons of travel time anomalies predicted by 1D ray theory, CSEM and NACT shows the importance of including finite frequency effects in the modeling.

The comparison of observed travel time anomalies with CSEM synthetics show that despite the limitations in the NACT method, the model (SAW24B16) gives a good prediction of travel time anomaly amplitudes particularly in the regions where the dataset for the model have a good sampling coverage. The travel time amplitudes are underestimated in some regions in the southern hemisphere. This suggests that the first step to get correct Vs anomaly amplitudes is to use a dataset with good sampling coverage in the inversion. We showed that we can find multiple models that fit the travel time anomalies better then the original model by keeping the shape of anomalies and changing the amplitudes and gradients. Calculating CSEM synthetic waveforms for each of these models and comparing them with waveform data allows us to evaluate which model better explains the data.

We performed simulations of coseismic and postseismic deformation due to the Mw=7.7 1819 Allah Bund earthquake, using a previously obtained source rupture model. Our results show that Coulomb failure stress on the rupture plane of the Mw7.6 2001 Bhuj event had increased by more than 0.1 bar due to the 1819 event. This is a small, but possibly signifi-

cant, amount. Other historic earthquakes in the Rann of Kachchh region that occurred since 1819 also predominantly occurred in regions of enhanced ΔCFS from the 1819 earthquake. This implies that coseismic and postseismic stress changes due to the 2001 Bhuj earthquake will lead to comparable regional stress perturbations in the Rann of Kachchh region and might thus result in continued enhanced earthquake activity in an extended earthquake sequence in an otherwise low-strain rate, intra-plate setting.

Bibliography

Antolik, M. and D. Dreger, Rupture process of the 26 January 2001 Mw 7.6 Bhuj, India, earthquake from teleseismic broadband data, *Bull. Seismol. Soc. Am.*, **93**, 1235-1248, 2003.

Bernardi, C., Y. Maday and A.T. Patera, A new nonconforming approach to domain decomposition: the mortar element method, In: Nonlinear Partial Differential Equations and Their Applications, (eds.) Brezis, H. and J. Lions, *Pitman, New York* , pp. 13-51, 1994.

Bendick, R., R. Bilham, E. Fielding, V. K. Gaur, S. Hough, G. Kier, M. N. Kulkarni, S. Martin, K. Mueller and M. Mukul, The January 26, 2001 "Republic Day" Earthquake, India, *Seism. Res. Lett.* , **72**, 328-335, 2001.

Bilham, R., E. Fielding, S. Hough, C. P. Rajendran and K. Rajendran, A reevaluation of the allah bund 1819 Earthquake using the 2001 Bhuj Earthquake as a template, *SSA abstract* , 2003.

Bilham, R., Slip parameters for the Rann of Kachchh, India, 16 June 1819, earthquake, quantified from contemporary accounts, *Geological Society, London, Special Publication* , **146**, 295-319, 1998.

Bréger, L. and B. Romanowicz, Thermal and chemical 3-D heterogeneity in D", *Science* , **282**, 718-720, 1998.

Bréger, L., B. Romanowicz and L. Vinnik, Tests of tomographic models in D" using differential travel times, *Geophys. Res. Lett.*, **25**, 5-8, 1998.

Bréger, L., B. Romanowicz and C. Ng, The pacific plume as seen by S, ScS, and SKS, *Geophys, Res. Lett.* ,**28**, 1859-1862, 2001.

Bullen, K.E., An Introduction to the Theory of Seismology, *Cambridge University Press*, 1963.

Capdeville, Y., E. Chaljub, J.P. Vilotte, and J. P. Montagner, Coupling the spectral element method with a modal solution for elastic wave propagation in global earth models, *Geophys. J. Int.*,**152**, 34-66, 2002.

Capdeville, Y., Methode couplee elements spectraux solution modale pour la propagation d'ondes dans la Terre a l'echelle globale, *PhD thesis, Universite Paris 7*, 2000.

Capdeville, Y., C. Larmat, J.P. Vilotte and J.P. Montagner, Direct numerical simulation of the scattering induced by a localized plume like using a coupled spectral element and modal solution, *Geophys. Res. Lett. ,* **29**, no 9, 10.1029/2001GL013 747, 2002.

Capdeville, Y., A. To and B. Romanowicz, Coupling spectral elements and modes in a spherical earth: an extension to the "sandwich" case, *Geophys. J. Int.*,**154**, 44-57, 2003.

Chaljub, E., Modelisation numerique de la propagation d'ondes sismiques a l'echelle du globe, *These de doctorat Universite Paris 7*, 2000.

Chaljub, E., Y. Capdeville and J. Solving, Elastodynamics in a solid heterogeneous 3 sphere: a spectral element approximation on geometrically non-conforming grids, *J. Comp. Phys.*, **183**, 457-491, 2003.

Chapman, C., A new method for computing synthetic seismograms, *Geophys. J. R. astr. Soc.*, **54**, 481-518, 1978.

Chéry, J., S. Carretier, and J. F. Ritz, Postseismic stress transfer explains time clustering of large earthquakes in Mongolia, *Earth Planet. Sci. Lett.*, **94**, 277-286, 2001

Chung, W.P. and H. Gao, Source parameters of the Anjar earthquake of July 21, 1956, India, and its seismotectonic implication for the Kutchrift basin, *Tectonophysics* ,**242**, 281-292, 1995.

Clevede, E. and P. Logonnne, Frechet derivatives of coupled seismograms with to an anelastic rotating Earth, *Geophys. J. Int.*, **124**, 456-482, 1996.

Cormier, V.F., Some problems with S, SKS and ScS observations and implications for the structure of the base of the mantle and outer core, *J. Geophys.*,**57**, 14-22, 1985.

Cummins, P.R., N. Takeuchi and R.J. Geller, Computation of complete synthetic seismograms for laterally heterogeneous models using the direct solution method, *Geophys. J. Int.*, **130**, 1-16, 1997.

Dahlen, F., S.-H. Hung and G. Nolet, Frechet kernels for finite-frequency traveltimes-I. Theory, *Geophys. J. Int.*, **141**, 157-174, 2000.

Dziewonski, A.M. and D.L. Anderson, Preliminary reference earth model, *Phys. Earth planet. Inter.*, **25**, 297-356, 1981.

Faccioli, E., F. Maggio, R. Paolucci and A. Quarteroni, 2D and 3D elastic wave propagation by a pseudospectral domain decomposition method, *J. Seismology*, **1**, 237-251, 1997.

Freed, A.M. and J. Lin, Delayed triggering of the earthquake at Hector Mine, California in 1999 by viscoelastic stress transfer, *Nature* ,**411**, 180-183, 2001.

Garnero, E., X., Lower mantle heterogeneity, *Ann. Rev. Earth planet. Sci.*, **28**, 509-37, 2000.

Garnero, E.J. and D.V. Helmberger, Travel times of S and SKS: Implications for three-dimensional lower mantle structure beneath the central Pacific, *J. Geophys. Res.*,**98**, 8225-8241,1993.

Garnero, E., J, Helmberger and V. Donald, A very slow basal layer underlying large-scale low-velocity anomalies in the lower mantle beneath the Pacific; evidence from core phases, *Physics of the Earth and Planetary Interiors* ,**91** 161-176, 1995.

Garnero, E. J. and D. V. Helmberger, Seismic detection of a thin laterally varying boundary layer at the base of the mantle beneath the Central-Pacific, *Geophysical Research Letters* ,**23**, 977-980, 1996.

Geller, R. and T. Ohminato, Computation of synthetic seismograms and their partial derivatives for heterogeneous media with arbitary natural boundary conditions using the direct solution method, *Geophys. J. Int.*, **116**, 421-446, 1994.

Geller, R. and N. Takeuchi, A new method for computing highly accurate DSM synthetic seismograms, *Geophys. J. Int.*, **123**, 449-470, 1995.

Gilbert, F., Exitation of normal modes of the Earth by earthquake sources, *Geophys. J. R. Astr.. Soc.*, **22**, 223-226, 1971.

Givoli, D. and J. Keller, Non-reflecting boundary conditions for elastic waves, *Wave Motion* , **12**, 261-279, 1990.

Grand, S., R. van der Hilst and S. Widiyantoro, Global seismic tomography: a snapshot of convection in the Earth, *Geol. Soc. Am. Today*, **7**, 1-7, 1997.

Grand, S.P., Mantle shear-wave tomography and the fate of the subducted slabs, *Phil. Trans. R. Soc. Lond.*, **360**, 475-491, 2002.

Grote, M.J. and J. Keller, On nonreflecting boundary conditions, *J. Comput. Phys.*, **122**, 231-243, 1995.

Gu, Y. J., A.M. Dziewonski, W.J. Su and G. Ekstrom, Models of the mantle shear velocity and discontinuities in the pattern of lateral heterogeneities, *J. Geophys. Res.*, **106** 11169-11199, 2001.

Gung, Y. and B. Romanowicz (2004) Q tomography of the upper mantle using three component long period waveforms,*Geophys. J. Int.*,**157**, 813-830

Haddon, R.A.W. and G.G.R. Buchbinder, Wave propagation effects and the Earth's structure in the lower mantle, *Geophys. Res. Lett.* , **13**, 1489-1492, 1986.

Hager, B., R.W. Clayton, M. A. Richards, R. P. Comer and A. M. Dziewonski, Lower mantle heterogeneity, dynamic topography and the geoid, *Nature* **313**, 541-545, 1985.

Harris, R. A., R.W. Simpson and P.A. Reasenberg, Influence of static stress changes on earthquake location in southern California, *Nature* ,**375**, 221-224, 1995.

Harris, R. A., Introduction to special section: Stress triggers, stress shadows, and implications for seismic hazard, *J. Geophys. Res.*,**103**, 24347-24358, 1998.

Hearn, E.H., R. Buergmann, and R. Reilinger, Dynamics of Izmit earthquake postseismic deformation and loading of the Duzce earthquake hypocenter, *Bull. Seism. Soc. Am.*, **92**, 172-193, 2002.

Helmberger, D.V., Theory and application of synthetic seismograms, In: Earthquakes: Observation, Theory and Interpretation, (ed.) Kanamori, H., *Soc. Italianadi Fisica, Bologna* , pp. 173-222, 1983.

Hough S. E., S. Martin, R. Bilham, and G.M. Atkinson, The 26 January 2001 M 7.6 Bhuj, India, Earthquake; observed and predicted ground motions, *Bull. Seismol. Soc. Am.*,**92**, 2061-2079, 2002.

Hutko, A. R., T. Lay, E. J. Garnero and J. Revenaugh, Seismic detection of folded, subducted lithosphere at the core- mantle boundary, *Nature*, **441**, 333-336, 2006.

Hung, S.-H., F. Dahlen and G. Nolet, Wavefront healing: a banana-doughnut perspective, *Geophys. J. Int.*, **146**, 289-312. 2001.

Ishii, M. and J. Tromp, Normal-mode and free-air gravity constraints on lateral variations in velocity and density of the Earth's mantle, *Science* ,**285**, 1231-1236, 1999.

Jade, S., M. Mukul, A. P. Imtiyaz, M. B. Ananda, P. D. Kemar and V. K. Gaur, Estimates of cosiesmic displacement and postseismic deformation using Global Positioning System geodesy for the Bhuj earthquake of 26 January 2001, *Current Science*,**82** , 748-752, 2002.

Johnston, A.C. and L.R. Kanter, Earthquakes in stable continental crust, *Scientific American*,**262**, 68-75, 1990.

Kennett, B.L.N. and O.Gudmundsson, Ellipticity corrections for seismic phases, *Geophys. J. Int.*, **127** , 40-48, 1996.

Komatitsch, D. and J. Tromp, Introduction to the spectral element method for three-dimensional seismic wave propagation, *Geophys. J. Int.*, **139**, 806-822, 1999.

Komatitsch, D. and J. Tromp, Spectral-element simulations of global seismic wave propagation, part II: 3-D models, oceans, rotation, and gravity, *Geophys. J. Int.*, **150**, 303-318, 2002.

Komatitsch, D. and J.P. Vilotte, The spectral element method: an effective tool to simulate the seismic response of 2D and 3D geological structures, *Bull. Seism. Soc. Am.*, **88**, 368-392, 1998.

Lay, T., Q. Williams and E. Garnero, The core-mantle boundary layer and the deep Earth dynamics, *Nature*, **392**, 461-468, 1998.

Li, X.D., and B. Romanowicz, Comparing of global waveform inversions with and without considering cross-branch modal coupling, *Geophys.J.Int.*,**121**, 695-709,1995.

Li, X.D. and B. Romanowicz, Global mantle shear velocity model developed using onlinear asymptotic coupling theory, *J. Geophys. Res.*, **101**, 11245-22271, 1996.

Li, X.D. and T. Tanimoto, Waveform of long-period body waves in a slightly aspherical Eath model, *Geophys. J. Int.*, **112**, 92-102, 1993.

Liu, X. and A. Dziewonski, Global analysis of shear wave velocity anomalies in the lowermost mantle, In: The Core-Mantle Boundary Region, (eds.) Gurnis, M. et al., *Geodyn. Ser. Washington DC, AGU* , **Vol. 28, pp 21-36**, 1998.

Liu, X.F., J. Tromp and A.M. Dziewonski, Is there a first-order discontinuity in the lowermost mantle?, *Earth Planet. Sci. Lett.* , **160** , 343-351, 1998.

Lognonne, P. and B. Romanowicz, Modelling of coupled normal modes of the Earth: the spectral method, *Geophys. J. Int.*, **102**, 365-395, 1990.

Loper, D. and T. Lay, The core-mantle boundary region, *J. Geophys. Res.*, **100**, 6397-6420, 1995.

Maday, Y. and A. Patera, Spectral element methods for the incompressible Navier-Stokes equations, In: State of the Art Survey in Computational Mechanics, (eds.) Noor, A. and J. Oden, *ASME, New York*, pp. 71-143, 1989.

Masters, G., S. Jonhson, G. Laske and H. Bolton, A shear-velocity model of the mantle, *Phil. Trans. R. Soc. Lond. A*, **354**, 1385-1411, 1996.

Masters, G., G. Laske, H. Bolton and A.M. Dziewonski, The relative behavior of shear velocity, bulk sound speed, and compressional velocity in the mantle: Implications for chemical and thermal structure, In: Earth's Deep Interior: Mineral Physics and Tomography from the Atomic to the Global Scale, (eds.) S. Karato, A. Forte, R. Liebermann, G. Masters, L. Stixrude, , *Geophysical Monograph 17, AGU, Washington DC*, pp. 63-87, 2000.

Mégnin, C. and B. Romanowicz, The three-dimensional shear velocity structure of the mantle from the inversion of body, surface and higher-mode waveforms, *Geophys. J. Int.*,**143**, 709-728, 2000.

Miyashita, K., K. Vijaykumar, T. Kato, Y. Aoki and C. D. Reddy, Postseismic Crustal Deformation Deduced from GPS Observations, in "A Comprehensive Survey of the 26 Jan-

uary 2001 Earthquake (Mw 7.7) in the State of Gujarat, India", ed. http://www.st.hirosaki-u.ac.jp/ tamao/Gujaratweb.html

Murakami, M., K. Hirose, N. Sata, Y. Ohishi, and K. Kawamura, Phase transition of MgSiO3 perovskite in the deep lower mantle, *Science*, **304**, 855-85, 2004.

Negishi H., J. Mori, T. Sato, R. Singh, S. Kumar and N. Hirata, Size and orientation of the fault plane for the 2001 Gujarat, India earthquake (Mw7.7) from aftershock observations: A high stress drop event, *Geophys. Res. Lett.*, **29**, 10.1-10.4, 2002.

Effects of a perovskite-post perovskite phase change near core-mantle boundary in compressible mantle convection *Geophys. Res. Lett.*, **31**, no.16, 4 pp., 28, 2004.

Ni, S. and D.V. Helmberger, Horizontal transition from fast (slab) to slow (plume) structures at the core-mantle boundary, *Earth planet. Sci. Lett.*, **187**, 301-310, 2001.

Ni, S., D. V. Helmberger and J. Tromp, 3D Structure of the African super plume from waveform modeling, *Geophys. J. Int.*,**161** 283-294, 2005.

Ni, S., E. Tan, M. Gurnis and D.V. Helmberger, Sharp sides to the African super plume, *Science*,**296**, 1850-1852, 2002.

Oldham, R.D., The Cutch Earthquake of 16th June 1819 with a revision of the great earthquake of 12th June 1897, *Geological Survey of India Memoris* ,**46**, 71-146, 1926.

Oganov, A. R., and S. Ono, Theoretical and experimental evidence for a post-perovskite phase of MgSiO3 in Earth's D? layer, *Nature*, **430**, 445-448, 2004.

Panning, M. and B. Romanowicz, Inference on flow at the base of Earth's mantle based on seismic anisotropy, *Science*,**303**, 3 51-353, 2004.

Panning, M. and B. Romanowicz, A three dimensional radially anisotropic model of shear velocity in the whole mantle, *Geophys. J. Int.*, doi: 10.1111/j.1365-246.2006.03100

Patera, A.T., A spectral element method for fluid dynamics: laminar flow in a channel expansion, *J. Comput. Phys.*, **54**, 468-488, 1984.

Phinney, R.A. and R. Burridge, Representation of elastic-gravitational excitation of a spherical earth model by generalized spherical harmonics, *Geophys. J. R. Astr.o. Soc.*, **34**, 451-278, 1973.

Pollitz, F.F. and I.S. Sacks, The 1995 Kobe, Japan, Earthquake: A long-delayed aftershock of the offshore 1944 Tonankai and 1946 Nankaido earthquake, *Bull.Seismo.Soc.Amer.*,**87**, 1-10, 1997.

Pollitz, F.F., Coseismic deformation from earthquake faulting on a layered spherical Earth, *Geophs.J. Int.*, **125**, 1-14, 1996.

Pollitz, F.F., Gravitational-viscoelastic postseismic relaxation a layered spherical Earth, *J.Geophys. Res.*, **102**, 17921-17941, 1997.

Pollitz F.F., R. Burgmann and B. Romanowicz, Viscosity of oceanic asthenosphere inferred from remote triggering of earthquakes, *Science* ,**280**, 1245-1249, 1998.

Pollitz, F.F., and I.S. Sacks, Stress triggering of the 1999 Hector Mine earthquake by transient deformation following the 1992 Landers earthquake, *Bull.Seismo. Soc. Amer.*, **92**, 1487-1496, 2002.

Pollitz,F.F., M. Vergnolle and E. Calais, Fault interaction and stress triggering of twentieth century earthquakes in Mongolia, *J. Geophys Res.*, **108 (B10), 2503**, doi:10.1029/2002JB002375, 2003.

Rajendran, C.P. and K. Rajendran, Characteristics of deformation and past seismicity associated with the 1819 Kutch earthquakes, Northwestern India, *Bull.Seismo.Soc.Amer.*,**91**, 407-426, 2001.

Response of regional seismicity to the static stress change produced by the Loma Prieta earthquake, *Science*, **255**, 1687-1690, 1992

Ritsema ,J., H.J. van Heijst and J.H. Woodhouse, Complex shear wave velocity structure imaged beneath Africa and Iceland, *Science*,**286**, 1925-1928, 1999.

Ritsema, J., S. Ni, D.V. Helmberger and H.P. Crotwell, Evidence for strong shear velocity reductions and velocity gradients in the lower mantle beneath Africa, *Geophys. Res. Lett.*, **25**, 4245-4248, 1998.

Ritsema, J., and van Heijst, H.-J., 2000. Seismic imaging of structural heterogeneity in Earth's mantle: Evidence for large-scale mantle flow. *Science Progress*, **83**, 243-259, 1998

Robertson, S.G. and J.H. Woodhouse, Ratio of relative S to P velocity heterogeneity in the lower mantle, *J. Geophys. Res.*, **101**, 20041-20052, 1996.

Ronchi, C., R. Ianoco and P.S. Paolucci, The 'cubed sphere': a new method for the solution of partial differential equations in spherical geometry, *J. Comput. Phys.*, **124**, 93-114, 1996.

Sadourny, R., Conservative finite-difference approximations of the primitive equation on quasi-uniform spherical grids, *Mon.Weather Rev*, **100**, 136-144, 1972.

Sanchez-Sesma, F.J. and R. Vai, Absorbing boundaries in the frequency domain, In: The Effects of Surface Geology on Seismic Motion, (eds.) Okada, K. et al., *Rotterdam*, pp. 961-966, 1998.

Schubert, G., G. Masters, P. Olson and P. Tackley, Superplumes or plume clusters?, *Phys. Earth and Planet. Inter.*, **146**, 147-162, 2004.

Stead, R.J. and D.V. Helmberger, Numerical-analytical interfacing in two dimensions with applications to modeling NST seismograms, *Pure Appl. Geophys.*, **174**, 153-174, 1988.

Stein, R.S., G.C.P. Ling, and J. Lin, Stress triggering of the 1994 M=6.7 Northridge, California, earthquake by its predecessors, *Science* ,**265**, 1432-1435, 1994.

Stein, R. S., The role of stress transfer in earthquake occurrence, *Nature*,**402**, 605-609, 1999.

Su, W.J. and A.M. Dziewonski, Simultaneous inversion for 3-D variations in shear and bulk velocity in the mantle, *Phys. Earth Planet. Inter.*, **100**, 135-156, 1997.

Su, W.-J., R.L. Woodward and A.M. Dziewonski, Degree-12 model of shear velocity heterogeneity in the mantle, *J. Geophys. Res.*, **99**, 6945-6980, 1994.

Takeuchi, N. and R. Geller, Optimally accurate second order time-domain finite difference scheme for computing synthetic seismograms in 2-D and 3-D media, *Phys. Earth planet. Inter.*, **119**, 99-131, 2000.

Takeuchi, H. and M. Saito, Seismic surface waves, *Methods Comp. Phys.*, **11**, 217-295, 1972.

Tanaka, S., Very low shear wave velocity at the base of the mantle under the South Pacific superswell, *Earth Planet. Sci. Lett.*, **203**, 879-893, 2002.

Tanaka, S. and H. Hamaguchi, Heterogeneity in the lower mantle beneath Africa, as revealed from S and ScS phases, *Tectonophysics* ,**209**, 213-222, 1992.

Thomas, C., E. J.Garnero and T. Lay, High-resolution imaging of lowermost mantle structure under the Cocos Plate, *J. Geophys. Res.*, **109**, doi: 10.1029/2004JB003013, 2004.

To, A., Y. Capdeville and B. Romanowicz, Waveform modeling of 3D structure of D" region using a coupled SEM/ normal mode approach, *EOS Trans A.G.U.*, Fall'03 Meeting Abstract, S31D-0787, 2003.

Valette, B., About the influence of pre-stress upon the adiabatic perturbations of the Earth, *Geophys. J. R. Astr. Soc.*, **85**, 179-208, 1986.

Vidale, J. and M. Hedlin, Evidence for partial melt at the core-mantle boundary north of tonga from the strong scattering of seismic waves, *Nature*, **391**, 682-685, 1998.

Vinnik, L., L. Bréger and B. Romanowicz, Anisotropic structures at the base of the Earth's mantle, *Nature* , **393**, 564-567, 1998.

Vinnik, L., B. Romanowicz, Y.Le Stunff and L. Makeyeva, Seismic anisotropy in the D' layer, *Geophysical Research Letters* ,**22**, 1657-1660, 1995.

Wen, L., Seismic evidence for a rapidly varying compositional anomaly at the base of the Earth's mantle beneath the Indian Ocean, *Earth Planet. Sci. Lett.*, **194**, 83-95. 2001.

Wen, L., An SH hybrid method and shear velocity structures in the lowermost mantle beneath the central Pacific and South Atlantic oceans, *J. Geophys. Res.*,**107**, 10.1029/2001JB000499 29 March, 2002.

Wen, L. and D.V. Helmberger, A two-dimensional, p-sv hybrid method and its application to modeling localized structures near the core-mantle boundary, *J. Geophys. Res.*, **103**, 17 901-17 918, 1998a.

Wen, L. and D.V. Helmberger, Ultra-low velocity zones near the core-mantle boundary from broadband pkp precursors, *Science* , **279**, 1701-1703, 1998b.

Wesnousky S. G., L. Seeber, T. K. Rockwell, V. Thakur, R. Briggs, S. Kumar and D. Ragona, Eight days in Bhuj: Field report bearing on surface rupture and genesis of the January 26, 2001 Republic Day earthquake of India, *Seismological Research Letters*,**72**, 514-524, 2001.

Woodhouse, J.H. and F.A. Dahlen, The effect of a general aspherical perturbation on the free oscillations of the Earth, *Geophys. J. R. astr. Soc.*, **53**, 335-354, 1978.

Woodhouse, J.H. and T.P. Girnius, Surface waves and free oscillations in a regionalized Earth model, *Geophys. J. R. astr. Soc.*, **78**, 641–660, 1982.

Wysession, M.E., L. Bartko and J. Wilson, Mapping the lowermost mantle using core-reflected shear waves, *J. Geophys. Res.*, **99**, 13667-13684, 1994.

Wysession, M.E., K.M. Fischer, G.I. Al-eqabi, P.J. Shore and I. Gurari, Using MOMA broad-band array ScS-S data to image smaller scale structures at the base of the mantle, *Geophys. Res. Lett.*, **28**, 867-870, 2001.

.1 Construction of particular solution $\mathscr{B}$ and receiver operator $\mathscr{P}$

The equation to be solved in the frequency domain in Ω_{M2} is

$$-\omega^2\rho(\mathbf{r})\mathbf{u}^{M2}(\mathbf{r},\omega)-\mathscr{H}(\mathbf{r})\mathbf{u}^{M2}(\mathbf{r},\omega)=\mathbf{f}(\mathbf{r},\omega)\,, \tag{.1}$$

with a free surface boundary condition on $\partial\Omega$ and a Dirichlet boundary condition on Γ_2,

$$\mathbf{u}_{\Gamma_2}(\mathbf{r},\omega)=\mathbf{u}^S_{\Gamma_2}(\mathbf{r},\omega)\,, \tag{.2}$$

where $\mathbf{u}^{S}_{\Gamma_2}$ is the restriction of displacement on Γ_2 in the SEM domain Ω_S. $\mathbf{u}_{\Gamma_2}(\mathbf{r},\omega)$ is the restriction of displacement on Γ_2 in the upper modal solution domain Ω_{M2}. In this appendix, $\mathbf{u}$ with no upperscript denotes the displacement in the domain Ω_{M2}.

Taking into account the spherical symmetry of Ω_{M2}, we seek for a solution of the form

$$\mathbf{u}(\mathbf{r},\omega) = \mathbf{d}_{\ell,m}(r,\omega)\cdot\mathscr{Y}_{\ell,m}(\theta,\phi)\,. \tag{.3}$$

where $\mathscr{Y}_{\ell,m}$ is the generalized spherical harmonics tensor (see paper 1 for details). Three solutions of (.1) without second member satisfying the free surface condition are found and they are denoted ${}_q\mathbf{d}_\ell(r,\omega)$ with $q=\{1,2,3\}$. If we are able to find a particular solution to (.1) with second member, $\mathbf{d}^p_{\ell,m}(r,\omega)$, then the general sultion in the frequency–spherical harmonic domain is

$$\mathbf{u}_{\ell,m}(r,\omega) = \sum_q {}_qa_{\ell,m}(\omega)\,{}_q\mathbf{d}_\ell(r,\omega) + \mathbf{d}^p_{\ell,m}(r,\omega)\,, \tag{.4}$$

where ${}_qa_{\ell,m}(\omega)$ is an excitation coefficient that will be determined by the boundary condition (.2). To build $\mathbf{d}^p_\ell$ we can use mode summation as it is classicaly done in seismology (e.g. [*Gilbert*, 1971; *Woodhouse and Girnius*,1982.]). To build the normal mode basis to be used for this purpose, any boundary condition on Γ_2 can be choosen, and for practical reason, we take an homogeneous Dirichlet boundary condition. In the following, we note $\mathscr{D}_\ell$ and $\mathscr{T}_\ell$ the tensors defined in the generalized spherical harmonics basis $(\mathbf{e}_\alpha)$ by,

$$[\mathscr{D}_\ell]^{q,\alpha}(\omega) = {}_qd^\alpha_\ell(r_\Gamma,\omega)\,,\quad [\mathscr{T}_\ell]^{q,\alpha}(\omega) = {}_qt^\alpha_\ell(r_\Gamma,\omega)\,,$$

and $\tilde{a}_{\ell,m}$ the vector of components $[\tilde{a}_{\ell,m}]_q = {}_qa_{\ell,m}$. Thanks to the choice $\mathbf{d}^p_{\ell,m}(r_{\Gamma_2},\omega)=0$,

using (.2), (.4) we have

$$\tilde{a}_{\ell,m}(\omega) = \mathbf{u}^S_{\ell,m}(r_\Gamma,\omega)\cdot\mathscr{D}_\ell(\omega)^{-1} \qquad \forall\ (\ell,m,\omega),\ \omega\notin\Pi^d_\ell\,, \tag{.5}$$

where Π^d_ℓ is the set of eigenfrequency where $\mathscr{D}_\ell^{-1}$ is not defined. Using (.4), its corresponding expression in traction and the *DtN* expression (2.8), as in paper 1, we can still write for the *DtN* operator

$${}^t\mathscr{A}_\ell(\omega) = \mathscr{D}_\ell^{-1}(\omega)\cdot\mathscr{T}_\ell(\omega) \qquad \forall\omega\notin\Pi^d_\ell\,, \tag{.6}$$

where ^{t} denotes the transposition. We have

$$\mathscr{B}^d_{\ell,m}(\omega) = \mathbf{d}^p_{\ell,m}(r_\Omega,\omega)\,, \tag{.7}$$

$$\mathscr{B}_{\ell,m}(\omega) = \mathbf{t}^p_{\ell,m}(r_{\Gamma_2},\omega)\,, \tag{.8}$$

where $\mathbf{t}^p$ is the corresponding traction to $\mathbf{u}^p$. To find the operator $\mathscr{P}$, we use the same process as for the *DtN* operator to obtain

$${}^t\mathscr{P}_\ell(\omega) = \mathscr{D}_\ell^{-1}(\omega)\cdot\mathscr{D}^S_\ell(\omega) \qquad \forall\omega\notin\Pi^d_\ell\,, \tag{.9}$$

where $[\mathscr{D}^S_\ell]^{q,\alpha}(\omega) = {}_qd^\alpha_\ell(r_\Omega,\omega)$

To build a particular solution $\mathbf{u}^p$, we name $\mathbf{U}_{q,n,\ell}(r)$ and $\mathbf{T}_{q,n,\ell}(r)$, such that

$$\mathbf{u}_k(\mathbf{r}) = \mathbf{U}_{q,n,\ell}(r) \cdot \mathscr{Y}_{\ell,m}(\theta,\phi)\,,$$

$$\mathbf{t}_k(\mathbf{r}) = \mathbf{T}_{q,n,\ell}(r) \cdot \mathscr{Y}_{\ell,m}(\theta,\phi)\,,$$

the eigenfunction in Ω_{M2} in displacement and its corresponding traction (on a spherical surface of radius r) associated to the eigenfrequency ω_k with $k = (q,n,\ell,m)$ where q corresponds to the type of mode (spheroidal or toroidal) and n is the radial order of the eigenfrequency. Using classical modal summation and (.8), we have in the frequency–spherical harmonics domain

$$\mathscr{B}_{\ell,m}(\omega) = g(\omega)\left[\sum_{q,n} \frac{(\mathbf{u}_k,\mathbf{f})}{\omega^2-\omega_k^2}\,\mathbf{T}_{q,n,\ell}(r_{\Gamma_2})\right], \tag{.10}$$

where wavelete g is such $\mathbf{f}(\mathbf{r},t) = g(t)\mathbf{f}(\mathbf{r})$ and the inner product definition is

$$(\mathbf{f},\mathbf{g}) = \int_{\Omega_2} \mathbf{f}\cdot\mathbf{g}\,\mathrm{d}\mathbf{x}\,. \tag{.11}$$

In the time–space domain we obtain

$$\mathscr{B}(\theta,\phi,t) = g(t) * \sum_k \left[H(t)\frac{\sin(\omega_k t)}{\omega_k}(\mathbf{u}_k,\mathbf{f})\,\mathbf{T}_{q,n,\ell}(r_{\Gamma_2})\right] \cdot \mathscr{Y}_{\ell,m}(\theta,\phi)\,. \tag{.12}$$

where $*$ is the time convolution. We also obtain for $\mathscr{B}^p$, in the frequency domain:

$$\mathscr{B}^p_{\ell,m}(\omega) = g(\omega)\left[\sum_{q,n}\frac{(\mathbf{u}_k,\mathbf{f})}{\omega^2-\omega_k^2}\,\mathbf{U}_{q,n,\ell}(r_\Omega)\right], \tag{.13}$$

and in the time–space domain

$$\mathscr{B}^p(\theta,\phi,t) = g(t) * \sum_k \left[H(t)\frac{\sin(\omega_k t)}{\omega_k}(\mathbf{u}_k,\mathbf{f})\,\mathbf{U}_{q,n,\ell}(r_\Omega)\right]\cdot \mathscr{Y}_{\ell,m}(\theta,\phi)\,. \tag{.14}$$